TERAHERTZ IMAGING FOR NONDESTRUCTIVE EVALUATION AND MATERIAL CHARACTERIZATION

A Dissertation
Presented to
The Academic Faculty

By

Junliang Dong

In Partial Fulfillment
of the Requirements for the Degree
Doctor of Philosophy in the
School of Electrical and Computer Engineering

Georgia Institute of Technology

August 2017

TERAHERTZ IMAGING FOR NONDESTRUCTIVE EVALUATION AND MATERIAL CHARACTERIZATION

Approved by:

Dr. David S. Citrin, Advisor
School of Electrical and Computer Engineering
Georgia Institute of Technology

Dr. Waymond R. Scott
School of Electrical and Computer Engineering
Georgia Institute of Technology

Dr. Paul L. Voss
School of Electrical and Computer Engineering
Georgia Institute of Technology

Dr. Justin Romberg
School of Electrical and Computer Engineering
Georgia Institute of Technology

Dr. Nico F. Declercq
Woodruff School of Mechanical Engineering
Georgia Institute of Technology

Dr. Alexandre Locquet
School of Electrical and Computer Engineering
Georgia Institute of Technology

Date Approved: June 22, 2017

Aide-toi, le ciel t'aidera.

To my parents

To myself

ACKNOWLEDGEMENTS

First and foremost I would like to express my deep sense of gratitude and appreciation to my Ph.D. advisor Prof. David. S. Citrin. It has been a honor to be his first Ph.D. student working in the field of terahertz science and technology. His patient guidance, enthusiasm for the research and encouraging support have led me to go through all the tough times in the Ph.D. pursuit and to grow as a researcher in this wonderful world of terahertz. I am also grateful for the excellent example he has provided as a successful physicist, professor, and mentor.

I would like to thank Dr. Alexandre Locquet for his support and for all the discussions and suggestions he provided for my research work. Answering his questions was challenging sometimes, but I have to admit that it was helpful for a better understanding of the key to the problems.

I would like to express my gratitude to Prof. Nico F. Declecrq for his guidance on ultrasonics. Comparative studies between terahertz and ultrasonic imaging play an important role in this dissertation. Doing experiments in the LUNE lab was a precious experience for me, because it enabled me take advantage of my ultrasonics background and further improve my skills.

In regards to the investigation of fiber-reinforced composites, I thank Pascal Pomerade, a Ph.D. student in ENSAM, for performing fatigue testing and introducing various damages and defects into the composite samples. Pascal shared his knowledge of materials and mechanics, which helped me understand the damage mechanisms and verify the imaging results. For the study of artworks, I would like to acknowledge our collaborator Marcello Melis, the CEO of Profilcolore srl in Italy. We worked together on the multispectral imaging of art paintings, and I very much appreciated his enthusiasm and the kindness for providing various artworks as samples.

For this dissertation I would like to express my gratitude to the committee mem-

bers: Prof. Waymond R. Scott, Prof. Justin Romberg, and Prof. Paul L. Voss for their time, interest, and insightful comments.

My time at Georgia Tech was made enjoyable in large part due to many friends that became a part of my Ph.D. life. Many thanks to my dear friends, Dr. Xin Li, Dr. Fan Xu, Yang Wu, Xiaolong Wu, and Chien-Yuan Chang for sharing all my happiness and sadness no matter for the life or for the research, and offering help and support whenever needed.

Lastly, I would like to thank my parents for all their unconditional love and encouragement. I would like to thank them for raising me with a love of science and always supporting me in all my pursuits.

TABLE OF CONTENTS

Acknowledgments v

List of Tables x

List of Figures xi

Chapter 1: Introduction 1

1.1 Motivation and research problems 1

1.2 State-of-the-art 4

1.2.1 Terahertz imaging of fiber-reinforced composites 4

1.2.2 Terahertz characterization of multilayered coatings on metal . 8

1.2.3 Terahertz imaging in cultural heritage conservation science . . 11

1.3 Scope of the thesis 14

Chapter 2: Equipment and Imaging Contrasts 18

2.1 Terahertz time-domain spectroscopy system 18

2.2 Imaging contrast mechanisms 20

Chapter 3: Terahertz Nondestructive Evaluation of Fiber-reinforced Composites 22

3.1 Terahertz imaging of forced delaminations in glass fiber-reinforced composites 23

3.1.1 Terahertz 3D quantitative imaging 23

3.1.2 Comparison with ultrasonic C-scans 27

3.2 Enhanced terahertz imaging of small delaminations in woven glass fiber-reinforced composites 32

3.2.1 Influence of water vapor 34

3.2.2 Wavelet de-noising 35

3.2.3 Enhanced terahertz imaging with wavelet de-noising 37

3.3 Polarization-resolved terahertz imaging of impact damages in hybrid fiber-reinforced composites 44

3.3.1 Terahertz polarization versus carbon fiber orientation 44

3.3.2 Polarization-resolved terahertz imaging 46

Chapter 4: Terahertz Deconvolution For Stratigraphic Characterization of Multilayered Structures 58

4.1 Terahertz Deconvolution Based on Inverse Filtering 60

4.1.1 Terahertz frequency-wavelet domain deconvolution (FWDD) . 61

4.1.2 Characterization of failure modes in polymer-coated steel with FWDD 63

4.2 Terahertz Sparse Deconvolution 72

4.2.1 Terahertz sparse deconvolution with data-resolution 73

4.2.2 Terahertz sparse deconvolution with super-resolution 76

4.2.3 Terahertz sparse deconvolution considering pulse spreading . . 77

4.2.4 Numerical and experimental verification 80

4.3 Terahertz Deconvolution Based on Autoregressive Spectral Extrapolation 92

4.3.1 Autoregressive model for terahertz spectrum 94

4.3.2 Numerical and experimental verification 96

Chapter 5: Terahertz Reflectometry of Art Paintings 104

5.1 Terahertz stratigraphic and subsurface investigation of a 20th century Italian oil painting on paperboard 106

5.1.1 Terahertz raw images of *After Fishing* 107

5.1.2 Reconstruction of stratigraphy based on FWDD 110

5.1.3 Correlation between terahertz and X-ray images 114

5.2 Terahertz characterization of the stratigraphic details of a 17th century Italian oil painting on canvas 118

5.2.1 Terahertz raw images of *Vièrge en priere* 121

5.2.2 Sparsity-based deconvolved signals 125

5.2.3 3D global mapping of detailed stratigraphy 128

Chapter 6: Conclusion and Perspective 136

6.1 Conclusion 136

6.2 Perspective 138

6.3 Publications 140

References 152

LIST OF TABLES

1.1 State-of-the-art THz imaging of actual art paintings 13

LIST OF FIGURES

1.1 The terahertz portion of the electromagnetic spectrum. 1

2.1 Schematic diagram of THz time-domain spectroscopy (TDS) system in both reflection and transmission configurations. 19

2.2 Image of the advanced variable angle reflection/transmission scan module. 20

3.1 (a) THz C-scan image of sample 1 with the contrast mechanism associated with the peak-to-valley difference of the reflected THz pulse within the time window 13-20 ps. (b) THz C-scan image after applying 50% rule for sizing the delaminations. 24

3.2 THz reflection B-scan images through the cross-sections labeled in Fig.3.1(a) with the contrast mechanism associated with the amplitude of the reflected THz pulse. 25

3.3 Three-dimensional THz imaging for sample 1. 26

3.4 Time traces of detected reflected THz signals (a) in the absence of delamination and (b) with delamination. 26

3.5 THz reflection images of representative samples. THz C-scans (a1) to (a6), B-scans (b1) to (b6), and time-domain waveforms (c1) to (c6) corresponding to samples 23, 10, 60, 46, 51, and 57, respectively. . . . 28

3.6 Ultrasonic imaging C-scan results for samples 51 and 57. (a) 51 in transmission, (b) 57 in transmission, (c) 51 in reflection, and (d) 57 in reflection modes. 29

3.7 Ultrasonic time-domain waveforms without and with delamination for sample 51 in (a) transmission mode and (b) reflection mode. 29

3.8 Ultrasonic B-scan images for (a) sample 51 with x position at 18 mm, (b) sample 57 with x position at 18 mm. 30

3.9 Estimated reflected THz pulses in region with delamination indicating the observed features associated with reflections off various interfaces. 32

3.10 Schematic level-3 decomposition of a signal with stationary wavelet transform (SWT). 36

3.11 The photograph of the woven E-glass fiber reinforced nylon matrix laminate. Inset: Amplification of the photograph to show the size of the fiber bundles. 37

3.12 THz reference signal with and without wavelet de-noising in (a) time domain and (b) frequency domain. The inset in (a) shows the fluctuations in the signal due to ambient water vapor. 38

3.13 Multiple parameter regress analysis of measured THz waveform without delamination to identify the water-vapor effect. 39

3.14 Typical reflected THz waveforms with and without wavelet de-noising in the region (a) without and (b) with delamination. 40

3.15 THz C-scan images based on THz waveforms (a) without and (b) with wavelet de-noising. 41

3.16 Binary THz C-scan images based on THz waveforms (a) without and (b) with wavelet de-noising. 42

3.17 THz B-scan images based on THz waveforms (a) without and (b) with wavelet de-noising. 43

3.18 Binary THz B-scan images based on THz waveforms (a) without and (b) with wavelet de-noising. 43

3.19 Schematic diagram of hybrid fiber-reinforced composite sample indicating dimensions and internal structure. 46

3.20 Schematic diagram (edge view) of sample subjected to low-velocity impact damage with highlighted damage types. 47

3.21 Ultrasonic C-scan results (a) in transmission and (b) in reflection modes. The ultrasonic waves are incident from the top surface of the sample. The contrast is based on the absolute value of the amplitude of the second-round signal in transmission and the second echo in reflection. 48

3.22 Estimated reflected THz waveforms (a) in undamaged region and (b) in region with delamination. 49

3.23 Typical time-of-flight waveforms from an undamaged region with THz polarization parallel and perpendicular to the carbon fibers. 51

3.24 THz C-scans of the top surface with polarization perpendicular (a) and parallel (b) to the carbon-fiber orientation. 52

3.25 THz C-scans of the Interface I with polarization perpendicular (a) and parallel (b) to the carbon-fiber orientation. 52

3.26 THz B-scans incident on the top surface (along section y=0) and with polarization perpendicular (a) and parallel (b) to the carbon-fiber orientation. 52

3.27 THz C-scans of the bottom surface with polarization perpendicular (a) and parallel (b) to the carbon fiber orientation. 55

3.28 THz C-scans of the Interface II with polarization perpendicular (a) and parallel (b) to the carbon fiber orientation. 55

3.29 Temporal waveforms for perpendicular THz polarization at selected positions on sample (see Fig. 11). 56

3.30 B-scans incident from the bottom surface (along section y=0) and with polarization perpendicular (a) and parallel (b) to the carbon-fiber orientation. 57

4.1 Hanning window function with typical values, t_0=10 ps and f_c=4 THz, in the time domain and its Fourier transform (power spectrum) in the inset. 62

4.2 (a) Visible photograph of the surface of the coating sample with four typical positions highlighted to represent different failure modes. This photograph is also labeled with the pixel number which is the same as the THz C-scans in the following section. (b) Optical micrograph from the edge of the coated sample to roughly estimate the thicknesses of the coating and the steel plate. 64

4.3 The THz raw signals [(a1) and (b1)] and deconvolved signals [(a2) and (b2)] at positions (50, 60) and (70, 190), with the corresponding representations of round-trip echoes in [(a3) and (b3)]. 65

4.4 (a) THz C-scan based on the raw signals with the contrast mechanism as the maximum amplitude of the received signal, which is similar to the optical photograph in Fig. 4.2(a); (b) THz C-scan based on the deconvolved signals associated with the delamination, which indicates the regions with delamination and the physical thicknesses of the delamination across the coating plane. 66

4.5 THz raw signals [(a1) and (b1)] with the corresponding deconvolved signals [(a2) and (b2)] at positions (79, 115) and (21, 121) where a blister is visually present. 68

4.6 (a) THz C-scan based on the optical delay between the first positive peak and second positive peak in the deconvolved signals, which represents the optical distance between the coating surface and the top surface of the metal substrate; (b) THz C-scan based on the amplitude of the second positive peak in the deconvolved signals, which indicates the adhesive condition. 69

4.7 Optical micrographs associated with different failure modes after peeling off the coating. (a) Oxidized substrate in the blistering area; (b) Oxidized substrate in the delamination area; (c) Comparison between the steel substrate at the undamaged area and the blistering area by peeling off the coating at one blister area and the adjacent undamaged area; (d) Grown metal oxide due to corrosion along the scratch. . . . 70

4.8 THz image of the thickness distribution, as well as the surface topology, of the coating. Different failure modes, including corrosion, delamination, and blistering, have been characterized quantitatively in three dimensions. 71

4.9 Comparisons between the assumed (a)$f_0[n]$ and (b)$f_0'[n]$, and the deconvolution results obtained by sparse deconvolution and FWDD respectively. Insets are the zoom-in images of corresponding boxed peaks. 82

4.10 Comparisons between the assumed (a)$f_0[n]$ and (b)$f_0'[n]$, and the deconvolution results obtained by DR sparse deconvolution, SR sparse deconvolution with $K = 4$ and FWDD respectively. Insets are the zoom-in images of corresponding boxed peaks. 84

4.11 Two samples with multi-layered structures. (a) Sample A: a three-layered structure, which is composed of one copy paper, air gap and one polymer coating; (b) Sample B: a seven-layered structure, which is composed of four different papercards with air gaps between them. 84

4.12 The THz reference signal used in the deconvolution of experimental THz received signals, which contains 512 data points with sampling period $T_s = 0.093$ ps. The inset is the frequency spectrum of this reference signal. 85

4.13 The raw and deconvolved signals for Sample A. (a) The received THz signal from Sample A; (b) The deconvolved signal with FWDD; (c) The deconvolved signal with DR sparse deconvolution. 87

4.14 Comparison between the DR deconvolved sigal and the SR deconvolved signals with the up-sampling factor $K = 2, 4$ and 8. Two insets are the zoom-in version of the first and fourth peaks. 88

4.15 Comparsion between the received signal and the re-convolution signal. (a) Comparison between the re-convolution without considering the pulse spreading effect and the actual received signal, and the inset is the zoom-in of the last echo; (b) Comparison between the re-convolution considering the pulse spreading effect and the actual received signal, and the inset is the zoom-in of the last echo; (c) The deviation between $h(t) \otimes f_{DR}(t)$ and $y_0(t)$ in (a); (d) The deviation between $h_a(t) \otimes f_{DR}(t)$ and $y_0(t)$ in (b). 89

4.16 Comparison between the deconvolved signals with and without considering the temporal pulse spreading effect. (a) The deconvolved signal with FWDD; (b) The deconvolved signal with sparse deconvolution without considering the pulse spreading; (c) The deconvolved signal with sparse deconvolution including pulse spreading; (d) The zoom-in of the last three interefaces in (b); (e) The zoom-in of the last three interefaces in (c). 90

4.17 The assumed impulse response function h_0 and the simulated received THz signal r_0. The inset shows the actual THz reference signal f_0. . . 97

4.18 (a) Comparison between the assumed frequency spectrum H_0, the deconvolved frequency spectrum by direct inverse filtering H_{inv} and the estimated frequency spectrum by AR spectral extrapolation H_{AR}. (b) The zoom-in of (a), which shows the detailed data allocation for the AR model. 98

4.19 Comparison of the simulated deconvolution results obtained by AR deconvolution with $p = 44$, FWDD and the assumed impulse response function. The inset shows the AIC values with different model orders. 100

4.20 (a) The deconvolution results based on FWDD and AR deconvolution. The inset shows the received THz signal reflected from the poly-coated steel sample; (b) The estimated frequency spectrum (up to 5 THz) based on autogressive spectral extrapolation. 102

5.1 Images of *After Fishing* by Ausonio Tanda. (a) Visible photograph of *After Fishing*, and (b) X-ray transmission image of *After Fishing*. . . 107

5.2 THz C-scan image of *After Fishing* in time domain based on the raw data. 108

5.3 THz C-scan images of *After Fishing* in frequency domain at (a) 0.4, (b) 0.6, (c) 0.8, and (d) 1.2 THz. 109

5.4 THz imaging results of the 'Spots' location in the paperboard. . . . 109

5.5 THz frequency-wavelet deconvolution result for a typical THz waveform.111

5.6 Four different types of the deconvolved signals with (a) (d) corresponding to Type I Type IV. 111

5.7 THz C-scans based on the Type I signal and the main peak indicating the surface feature of the painting. 112

5.8 THz C-scans based on the Type II and III signals indicating the existence of the underlying layer. 113

5.9 Comparison between THz B-scans based on the raw data and binary THz B-scans based on the deconvolved data. 114

5.10 THz image of the thickness distribution of the applied paint layers calculated with an estimated refractive index of the pigments. 115

5.11 Raking light image of *After Fishing*. 116

5.12 The fused image of the X-ray image in red and THz thickness distribution image in green to distinguish the areas of similar intensity in yellow. 117

5.13 Images of *Vierge en priere*. (a) Visible photograph of the *Viège en priere*; Image of *Viège en priere* obtained by UV Fluorescence; (c) Image of *Viège en priere* obtained by IR Reflectography. 120

5.14 THz C-scans based on the raw THz data based on the following contrast mechanisms in the reflected signal: (a) peak-to-valley amplitude; (b) integrated spectrum between 0.5 and 1.0 THz; (c) peak-to-valley amplitude between 13 to 18 ps. The horizontal line at $Y = 150$, marked cross section, is in reference to the B-scan in Fig. 5.15. Contrast is normalized to one. 122

5.15 The THz B-scan based on the raw signal with the cross-section $Y = 150$. Two typical THz reflected signals are plotted corresponding to the THz B-scan, with the waveform at pixel (89, 150) in green and the waveform at pixel (124, 150) in blue. 124

5.16 Typical THz reflected signals and the sparsity-based deconvolved signals. Figures 5.16(a1), (a2), and (a3) show examples of raw reflected signals (black) and signals reconstructed from the sparse-deconvolution and reference signals. Figures 5.16(b1), (b2), and (b3) show the corresponding sparsity-based deconvolution signals (red); Fig. 5.16(b1) also shows the deconvolved signal achieved by FWDD for comparison. . . 126

5.17 Comparison for optical delay corresponding to the layers above the canvas between (a) the THz B-scan based on the raw data (Fig. 5.15 on an expanded vertical scale) and (b) the binary THz B-scan based on the deconvolved data with the cross-section $Y = 150$ in which a valid peak is assigned value '1' and the other positions '0' regardless of the sign or height of the peak. 127

5.18 Varnish features revealed by THz sparsity-based deconvolved signals. (a) THz C-scan based on the amplitude of the first peak of the deconvolved signal. The contrast is normalized to one; (b) THz C-scan based on the optical delay between the first and second peaks of the deconvolved signal. 129

5.19 Features of the pictorial layer revealed by THz sparsity-based deconvolved signals. (a) THz C-scan based on the amplitude of second peak of the deconvolved signals; (b) THz C-scan based on the amplitude of the peak corresponding to the interface between the pictorial and underpainting layers; (c) binary THz C-scan indicating the positions with the existence of delaminations; (d) THz C-scan based on the optical delay between the peaks corresponding to the thickness of the pictorial layer. 131

5.20 Features of the underpainting, imprimatura, and ground layers revealed by THz C-scans based on sparsity-based deconvolved signals. THz C-scans based on the amplitude of (a1) the fourth, (b1) fifth, and (c1) sixth peak. Contrast is normalized to one. THz C-scans based on the optical delay between (a2) the third and fourth peaks, (b2) fourth and fifth peaks, and (c2) fifth and sixth peaks. 133

5.21 The optical microscopic image of a small region at the edge of *Vièrge en priere*. The applications of ground, imprimatura, and the underpainting can be clearly identified. 133

5.22 White-light raking images of *Vièrge en priere* with the light source (a) placed on the left side and (b) the top side of the painting. 134

SUMMARY

Thanks to the emergence of powerful light sources and highly sensitive detectors operating in the terahertz (THz) spectral region, the traditional THz 'gap' (0.1-10 THz) is shrinking fast nowadays. Recent advances in photonics and electronics enables the development of compact but sophisticated THz time domain spectroscopy (TDS) systems. Today, pulsed THz imaging based on THz-TDS systems is investigated in many areas spanning from nondestructive evaluation (NDE), industrial quality control, medical imaging and security sectors to studies of fundamental physics and cultural heritage. Despite the on-going broad applications of THz imaging, a THz 'killer application'– a novel, innovative use in which THz imaging exhibits higher performance than any other existing techniques, is still waiting to be clearly identified. Therefore, the research problems of this thesis aim at the exploration of the potential of THz imaging in the fields of industry and cultural heritage conservation science, and developing theories and techniques to enhance the capabilities of THz imaging to solve practical problems in NDE and material characterization.

The thesis is outlined as follows.

Chapter 1 introduces the background of this thesis. The basic knowledge of THz radiation is briefly introduced. The motivation and research problems of this project are described. The state-of-the-art of the development and applications of THz imaging in the fields of industry and cultural heritage conservation science are also summarized in this chapter.

Chapter 2 presents the main equipment, the THz time-domain spectroscopy (TDS) system, utilized in this project. The main imaging contrasts, based on which the THz results are presented, are briefly described.

Chapter 3 is devoted to NDE of fiber-reinforced composites with THz imaging. Fiber-reinforced composites are widely used in the industry to take the place of con-

ventional materials, such as metal. In this chapter, three case studies are presented. The first case study shows the capability of THz imaging in providing 3D quantitative information for characterization of delaminations in glass-fiber reinforced composites. The spatial resolution, including the lateral resolution and the axial resolution of THz reflective imaging are discussed in detail in this study. The second case study takes the water-vapor influence into account, especially for THz characterization of small delaminations in woven glass-fiber reinforced composites. Wavelet de-noising is applied to cancel the noise due to the atmospheric water-vapor. In view of the difficulty and expense in purging with dry nitrogen to physically remove the water-vapor features in many cases, the demonstrated results will be of great interest for a range of laboratory- and field-based THz NDE applications. In the third case study, polarization-resolved THz imaging is firstly applied to a hybrid fiber-reinforced composite laminate. The evolution of intra- and inter-laminar damage throughout the thickness of the laminate subject to low-velocity impact is evaluated. Inter-laminar damage at the interface and the intra-laminar damage close to the same interface can be differentiated by taking advantage of the sensitivity of the carbon-fiber orientation to the THz polarization. Comparative studies with ultrasonic imaging are also involved in the chapter.

Chapter 4 focuses on developing advanced THz deconvolution techniques to enhance the capability of THz imaging for the stratigraphic characterization of multi-layered structures with optically thin layers in the THz regime. Generally, layers with thicknesses smaller than 100 μm cannot be easily resolved based on the raw THz signals, due to the depth-resolution achieved by a typical THz TDS system, which further limits the applications of THz imaging. Deconvolution, if applied properly, can yield sub-wavelength or sub-pulse-width depth resolution. In the context of THz imaging, three kinds of deconvolution methods are developed in this chapter. Conventional deconvolution, such as THz frequency-wavelet domain deconvolution (FWDD),

which is based on inverse filtering is introduced. The depth-resolution achieved by FWDD is about 55 μm in air. FWDD is used in a case study for the characterization of various failure modes in polymer-coated. However, depth-resolution achieved by FWDD cannot satisfy all of the expected applications of THz imaging. In order to further enhance the depth-resolution, sparse representation is exploited, and sparse deconvolution based on an iterative shrinkage algorithm is developed. With an up-sampling approach, sparse deconvolution with super-resolution is also developed to overcome the time resolution limited by the sampling period in the measurement. A simple but effective time-domain model for describing the temporal pulse spreading due the frequency-dependent loss is also designed and introduced into the algorithm, which significantly improves the performance of sparse deconvolution in processing time-varying pulses during the propagation of THz waves in materials. The depth-resolution achieved by sparse deconvolution is about 45 μm in air. Finally, a novel method for enhancing the depth-resolution of THz deconvolution based on autoregressive spectral extrapolation is developed. An autoregressive process is modeled based on the THz frequency components with high SNR, and the missing frequency components in the low SNR regions are extrapolated based on the autoregressive model. In this way, the entire THz frequency spectrum of the impulse response function is recovered. This method is able to provide a 'quasi-ideal' impulse response function, and therefore, significantly enhances the depth-resolution for resolving optically thin layers in the THz regime. The depth-resolution achieved by this method is about 27 μm in air. The deconvolution techniques developed and presented in this chapter greatly enhance the capability for resolving optically thin layers in the THz regime, and provide a powerful tool to the entire THz community for a broad applications.

Chapter 5 is addressed to THz reflectometry of art paintings. Based on the advanced deconvolution techniques developed in Chapter 4, THz reflectometry with enhanced depth-resolution presents great potentials for the characterization of stratig-

raphy in historical paintings in this chapter. Compared with other techniques, THz reflectometry can provide 3D global mapping of the stratigraphy quantitatively. Two historical paintings are well-studied via THz reflectometry. The first one is a 19th century Italian oil painting on paperboard, *After Fishing*. Based on the deconvolved signals achieved by FWDD, the stratigraphy and subsurface features are clearly revealed. The second historical painting is a 17th century Italian easel painting, *Vièrge en priere*. Sparsity-based THz reflectometry is applied to characterize the detailed stratigraphy. Based on the sparsity-based deconvolved signals, the detailed layer structure, including the canvas, the ground, imprimatura, underpainting, pictorial, and varnish layers are clearly identified. In addition, a hitherto unidentified restoration of the varnish has been found. It is important to note that, it is the first time to our knowledge THz reflectometry has resolved multiple layers in an easel painting. Based on this work, the full promise of THz reflectometry to provide a global and detailed account of an easel painting's stratigraphy has been unlocked by exploitation of the sparse deconvolution.

Chapter 6 is divided into three sections. Firstly, the conclusion part summarizes the results and contributions of this thesis. Secondly, further possible research directions are proposed in the perspective part. The peer-reviewed publications and conferences attended during the time of Ph.D. study are listed at the end of this chapter.

CHAPTER 1

INTRODUCTION

1.1 Motivation and research problems

The terahertz (THz) portion of the electromagnetic spectrum, shown in Fig.1.1, extends from approximately 100 GHz to 10 THz, and lies between the microwave and infrared; the wavelength in this range is 3 mm to 30 μm. THz waves can penetrate numerous nonmetallic materials that may be opaque in the range of visible and infrared light. Moreover, as nonionizing radiation, THz waves present minimal known health risks. The potential and suitability of the THz technology for practical applications such as nondestructive evaluation (NDE) and material characterization, have been blocked for many years due to the technical difficulty of producing efficient sources and detectors. However, with the development of ultrafast components in both photonics and electronics, the situation has evolved drastically in the last two decades. This evolution, has enabled the introduction of the THz technology to the NDE and material characterization fields, quickly highlighting the advantages of the THz technology for the evaluation and characterization of advanced materials and complex structures.

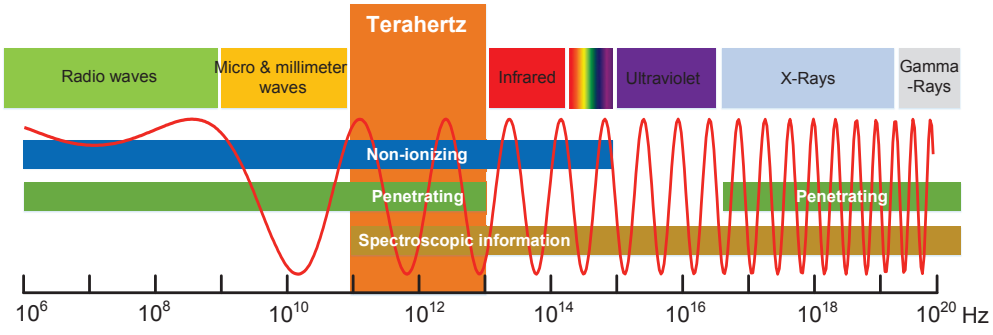

Figure 1.1: The terahertz portion of the electromagnetic spectrum.

In modern industry, fiber-reinforced composites, which combine the merits of high strength and low weight, offer an alternative to conventional structural materials and are widely used for various applications including aerospace, automotive, renewable energy and marine. As a result, the wide applicability of fiber-reinforced composites has created the correspondingly need for advanced NDE techniques for inspection and failure detection during manufacturing and maintenance. Numerous NDE techniques capable of characterizing damages and defects in fiber-reinforced composites have been developed, such as ultrasound, shearography, IR thermography, and X-ray radiography, to name a few. However, until now, only the ultrasonic C-scan has found widespread implementation in industry, because of simplicity of analysis and its effectiveness in geometrically locating damages and defects. Ultrasonic C-scans can provide a good trade-off between material penetration and measurement resolution, and ultrasonic C-scans in pulse-echo mode can also provide qualitative information in depth for thick fiber-reinforced composite samples. However, some of the difficulties associated with ultrasonic C-scans for the NDE of fiber-reinforced composites have been highlighted: (1) negligible quantitative information in depth can be obtained in thin samples with small thickness-to-wavelength ratio due to the relatively large time duration of ultrasonic pulse signal; (2) because of the attenuation of ultrasonic waves in fiber-reinforced composites (especially in glass fiber-reinforced composites), the operating frequency cannot be sufficiently high (usually less than 10 MHz), thus limiting the resolution; and (3) liquid coupling may be required. Although contactless ultrasonic techniques using laser and air-coupled transducers have been proposed, problem (1) and (2) remain. Therefore, alternative nondestructive, noncontact, and nonionizing techniques with high resolution are still needed for inspection of fiber-reinforced composites.

In the steel industry, NDE techniques for monitoring and characterizing coatings on steel are essential to verify protection of the steel surface from corrosion during

service. Coating failure can have many causes and manifestations. Especially, when a region of a coating system becomes detached from its substrate, the term 'adhesion failure' is commonly used. Delamination and blistering are two important types of coating failure in which compromised adhesion is strongly implicated. Since the exact cause and nature of coating failure is still in dispute, various NDE techniques have been explored to study damage mechanisms in coatings, such as electrochemical impedance spectroscopy (EIS), scanning electrochemical microscopy, acoustic emission, and thermography. However, not all of the NDE techniques mentioned above can provide quantitative information in depth, nor may they all be capable of monitoring the condition of adhesion. Scanning acoustic microscopy (SAM) and laser-ultrasonics can provide depth-specific information with enough resolution for characterizing coating systems; however, high attenuation in polymer materials limits the penetration depth of the ultrasonic waves. Therefore, alternative NDE techniques with relatively high resolution are still sought for quantitative evaluation of polymer-coated steel.

Great demand for advanced NDE techniques also appears in the field of cultural heritage conservation science, as preliminary noninvasive investigations are necessary before starting any conservation procedure on valuable artworks, in order to assist conservators in their decision-making process. The use of imaging techniques in the art conservation field ranges from well-established methodologies, such as high-resolution digital photography, visible raking light, UV fluorescence, X-ray radiography, IR reflectography, ect., to cutting-edge applications, such as multi- and hyper-spectral imaging techniques. In principle, all the above techniques could be used in order to reach the desired level of knowledge on the object under analysis. Nevertheless, most of these techniques lack penetration ability and can be only used to study surface or near-surface features. X-ray radiography is capable of penetration and can be used for investigating hidden features or defects. However, X-ray radiography cannot penetrate layers of high density pigments and cannot detect organic materials. X-ray

radiation is ionizing, which is unsafe for humans. Moreover, all these techniques are lack of depth resolution and convey little about the structure of the artworks.

THz imaging, which provides nondestructive, noncontact and nonionizing modality for characterizing materials, can be considered as a new promising NDE technique in both the fields of industry and art conservation. THz imaging can provide quantitative information in depth with a resolution of several tens of microns for characterizing materials and structures. Therefore, THz imaging can be utilized as an alternative or complementary modality to NDE techniques which have already been utilized in the fields of industry and art conservation.

Despite those advantages of THz imaging, a THz 'killer application'– a novel, innovative use in which THz imaging exhibits higher performance than any other existing NDE techniques, still needs to be clearly identified. Therefore, the research problems of this thesis aim at the exploration of the potentials of THz imaging in the fields of industry and art conservation, and developing theories and techniques to raise or enhance the capabilities of THz imaging to solve practical problems in NDE and material characterization.

1.2 State-of-the-art

1.2.1 Terahertz imaging of fiber-reinforced composites

THz imaging was first applied to the NDE of fiber-reinforced composites in 2006 [1] and has been explored extensively since. THz imaging enables to measure and determine the amplitude and the phase of a THz pulse transmitted through a sample. Changes in the amplitude and the phase of the THz field are related to the complex refractive index of the material. A spectroscopic approach can be implemented as the THz spectrum can be achieved based on the Fourier analysis. Hence, both parts of the frequency dependent complex refractive index can be obtained, which are the key parameters of materials. The basic approach of material parameter esti-

mation with THz waves involves constructing a theoretical model that incorporates the etalon effect and solving the inverse problem using a numerical algorithm to find complex refractive index values that fit the measured data to the model [2]. This approach is designed for estimating the material parameters of isotropic and homogeneous materials and can also be modified to the reflection configuration [3]. However, fiber-reinforced materials are anisotropic and inhomogeneous. For fiber-reinforced composites, the fiber fabrics are considered as the inclusion and the polymer matrix are considered as the host material. When the inclusions are small enough compared to the THz wavelength, effective medium approximations [4] can be used to equate the dielectric properties of individual components to the dielectric properties of their composite material. Naito et al. measured the dielectric properties of plain woven fabric glass fiber-reinforced epoxy matrix and eight-harness-stain fabric glass fiber-reinforced polyimide matrix composites in the THz range [5].

Besides the dielectric properties, fiber content and fiber orientation are also key parameters as both of them determine the mechanical performance of composites. Rutz et al. showed that the fiber content can be characterized by measuring the real refractive index of the composites and the fiber orientation can also be estimated by analyzing THz absorption at different polarizations [1]. Jördens et al. studied the birefringent properties of plastics filled with differing amounts of short glass fibers and measured the preferential fiber orientations as well as the fraction of oriented fibers based on the THz birefringence of the composites [6].

Due to the remarkable properties of THz waves, THz imaging has already been explored for detecting various damages and defects during the manufacturing and maintenance of composites. For composites reinforced by non-conductive fibers, such as glass fibers and ultra-high molecular weight polyethylene (UHMWPE) fibers, THz imaging can be utilized to detect both surface and underlying defects. For carbon fiber composites, due to the conductivity of carbon fibers, THz imaging has largely

been applied to detect surface or near-surface damages.

Impact damage is a typical damage that composites can suffer both in service and during maintenance due to many different types of collisions. The resulting impact-induced damage in composite laminates involves a combination of intra-laminar damage and inter-laminar damage, which leads to the separation of adjacent plies (delamination). Delaminations are considered as the most important failure mechanism, because they can severely degrade the strength and the integrity of the structure, and may propagate undetected during service leading to a significant decrease in stability and durability. Ospald et al. systematically studied a wide range of samples based on glass fiber composites with various types of defects with THz waves [7]. Impact damages (mainly fiber distortions and matrix cracking) caused by four different impact energies between 15 and 40 J were clearly observed and delaminations (also artificial inserts) in different depths of a sandwich structure were also successfully detected. Im et al. studied the penetration ability of THz waves in unidirectional carbon fiber composites and found that it depends on the relation between the THz polarization and carbon fiber orientation [8]. Bezborodov et al. characterized the impact damage on the surface of carbon fiber composites by monitoring the reflection coefficients across the surface and showed that the reflection coefficient in regions with and without impact damage can be more easily distinguished with polarization parallel to the carbon fiber orientation [9]. Palka et al. applied THz reflective imaging to evaluate an UHMWPE composite sample punctured by a projectile and 3D distribution of the delaminations inside the sample were clearly revealed [10].

Composite materials also suffer from burn damages due to high and periodic thermal stresses. Burn damage usually arises in the surface of composites where thermal gradients are the highest. Stoik et al. showed that THz imaging can detect burn damage in glass fiber composites generated by heating the part at 440°C for several minutes [11]. Such a heating generated relatively big blisters of few centimeters size

which were easily detected with THz imaging. Karpowicz et al. applied THz imaging to evaluate fire damage to a variety of carbon fiber composite samples. The THz polarization-dependent reflectivity was studied and how the polarization dependence changes versus the burn damage level was also demonstrated [12].

Mechanical stresses like long-term mechanical bending cycles, produce a continuous wearing out of the composite part while in-service. In consequence, the desired composites compactness and fiber matrix interaction on the composites part gets distorted, leading to detrimental effects in its performance. Stoik et al. applied THz transmissive imaging to detect the damages caused by mechanical fatigue generated by 6240 bending cycles in glass fiber composites. THz images clearly exhibited the damage areas with cracking and buckling across the central bend axis [13].

Voids or air bubbles are usual defects that arise during the manufacturing process. Based on the lower THz absorption of air, THz radiation is suitable for void detection in the surface and inner regions of composites. Stoik et al., demonstrated the detection of hidden circular voids of 3 mm diameter with THz imaging [11]. Moreover, composite materials are also widely used in adverse environmental conditions, i.e. offshore wind turbine blades. In such conditions, water usually diffuses into the composite part in service with time, then further degrading its performance. The relatively high permittivity of liquid water compared to other materials in the THz range enables a contrast mechanism for the detection and imaging of moisture. Jördens et al. employed THz spectroscopy to study the absorption of water into polyamide and wood plastic composite. A model for the dielectric behavior depending on the water content was developed and experimentally verified, which proved that THz waves could be considered as an ideal tool for the NDE of the water content [14].

THz imaging has shown great potentials for the NDE of fiber-reinforced composites. However, comparative studies with other NDE techniques are required in order to highlight the performance of THz imaging for this application. Despite the carbon

fibers are conductive, which limits the penetration depth of THz waves, THz imaging can also be utilized to perform subsurface investigation of the carbon fiber-reinforced composites based on the THz sensitivity to the carbon fiber distortion/breakage.

1.2.2 Terahertz characterization of multilayered coatings on metal

The most promising industrial application is the vehicle paint quality control in the automotive industry. Conventional methods to measure the thickness of car paint layers that are commercially available, such as magnetic gauges, eddy current measurements, and ultrasonic testing, all require direct contact between the measurement sensor and the painted car surface. These measurement techniques can only cover a limited number of sampling points on selected cars and hence lack the capability to identify paint defects, monitor drying processes, and map the thickness distribution of the paint layers over a larger surface of the vehicle. New possibilities to overcome these restrictions have been shown by THz imaging, and lots of efforts have been made to improve the capability of THz imaging to characterize multilayered coating structures.

In principle, the individual thicknesses of multilayered coatings can be directly determined using time of flight measurements of ultrafast THz pulses. The absolute thickness of a layer can be determined from the optical delay between two echoes, which are reflected from its front and back surface. For optically thick samples, the reflected adjacent echoes are separated in the time domain so that the individual thickness can be calculated directly from the time delay. However, if the layer is optically thin, the echoes may partially or totally overlap in time. If the exact structure of the multilayered coating is known, efforts can be made to increase the resolution of the minimum layer thickness. In [15], a multiple regression analysis approach using the least-square fitting algorithm was proposed, which decreased the minimum measurable paint film thickness to 20 μm; in [16], Su et al. extended this numer-

ical parameter fitting method by integrating the etalon effect, the absorption and dispersion of the coating materials, which further decreased the minimum measurable thickness down to 18 μm for both single and multilayered automotive paints; in [17], an advanced regression procedure with a self-calibration model is presented to measure individual automotive paint coatings in complex multilayered structures. Due to the high robustness of the proposed self-calibration method and the genetic optimization algorithms, the approach has been applied to resolve individual layer thickness within multilayered paint samples down to 4 μm.

Due to the high sensitivity of THz waves to water contents, THz imaging can also be considered as an effective tool to monitor the drying progress in paint film. In [18], adequate parameters for the drying progress can be extracted from the THz pulse-echo signal, and effectively applied to monitor the wet-to-dry transformation. The THz imaging can be a powerful tool for quality control of the paint film on the in-process monitoring of car body painting.

Surface roughness measurement is frequently used in industrial applications. THz imaging can be used for noncontact measurement of the surface roughness of metal or dielectric materials in the order of 10 μm [19]. This range of surface roughness is too large for optical sensors, but too small for microwave sensors. The surface roughness is obtained from the effective reflectivity of the surface, which is the ratio of the spectral intensity of waves reflected from the specimen and from a reference metal plate, whose reflectivity can be assumed to be 1. In [20], the rms roughness of six different aluminum samples spanning a rms roughness of $5-20$ μm was accurately determined by analyzing THz reflectance spectra. The rms roughness obtained by this method has good agreement with the rms roughness obtained using a surface profilometer. Moreover, it also showed that the THz reflectance spectra were able to discern two rough samples that differed in rms roughness by approximately 1 μm. It demonstrated that THz imaging can be used to identify and quantify material degra-

dation in metallic surfaces and the feasibility of using THz technology in industrial applications.

THz imaging can be used to study the degradation of coated steel. If the corrosion/rusting areas under the opaque coating can be detected at an early stage, both the repair costs and damage to the substrate steel could be reduced. So far, several papers related with the corrosion, rusting and iron-oxides have been published by Japanese researchers. Table I from [21] summarizes several diagnostic techniques used for detection of rust and defects. Different noncontact optical analysis methods were also used to the detection of rust in coated steel plates. This paper concludes that neither XRF and FTIR can detect rust region hidden by the coating. Reflection intensity measurements from a sample coated with epoxy resin show that optical coherence tomography using near-infrared (IR) light and THz waves can pass through the coating. This region can be reproduced by THz imaging without contact. In contrast, neither X-ray fluorescence nor Fourier transform infrared spectroscopy can detect the rust, because of the strong X-ray and IR absorption peaks of the coating. Typical THz imaging result in [21] shows that THz imaging can effectively reveal the rust areas under the coating.

It is known that iron-oxide at room temperature is an insulator or metal depending on the composition and crystal structure. The complex refractive indices at the THz frequencies of hematite (α-Fe_2O_3), magnetite (Fe_3O_4), and wustite (FeO) are investigated in [22]. This paper shows that hematite and wustite are low-loss dielectrics or insulators without free carriers at room temperature. The typical THz amplitude transmittance spectra of the hematite samples is shown, and the amplitude transmittance spectra of wustite also show similar behavior similar to the hematite. Based on the spectra, the complex refractive index of hematite can be extracted. The real refractive index is determined to be 5.5, and this value is almost independent of the frequency. Based on this value, the minimal thickness of hematite layer which

can be measured is estimated about 10 μm. On the other hand, this paper also shows that magnetite is metallic at room temperature. It has been known that magnetite is transformed from metal to insulator at temperatures below 120 K or at pressures of up to 40 GPa. However, achievement of the temperature and pressure for the insulator phase is unrealistic during the process of manufacturing steel. Therefore, in this paper, annealing of the magnetite layer on the steel plate with laser irradiation is proposed. Annealing at temperatures above 580 $°C$ followed by rapid cooling leads to a transformation from magnetite to wustite. In this way, almost the entire magnetite layer can be transformed to wustite, but there will still exist a residual magnetite layer with a thickness of up to 1 μm at the bottom of the transformed wustite layer. Based on the knowledge of the properties of iron-oxide in the THz range, THz reflective imaging can be used for 3D tomographic imaging of the corrosion area under coating [23]. Moreover, since the properties of Fe_2O_3 oxide and Fe_3O_4 oxide are different, THz imaging can also be used to perform separate identification of oxide. In the beginning stage, Fe_3O_4 oxide is formed when soaked water reaches the steel plate. Further deterioration of corrosion protection paint initiates paint cracking and oxide is provided into interface between paint and steel plate. Then Fe_3O_4 oxide changes to Fe_2O_3 oxide by chemical reaction with oxide, and material loss of substrate steel becomes severe. It is important to separately identify these corrosive materials under protection paint for evaluating corrosion condition of steel plate.

1.2.3 Terahertz imaging in cultural heritage conservation science

To date, there is only a limited number of scientific articles published for the application of THz techniques to the analysis of artists' material, art mock-ups, or laboratory panel tests, and only a few touch upon actual artworks [24]. In 2006, the first application of a THz imaging system in the art conservation field was performed in transmission mode to a 19th century canvas painting and the data obtained were

then compared with those acquired using the X-ray fluorescence technique [25]. The first THz transmission images indicate that different paints show a significantly different THz transmission features and also give rise to the hope that the hidden wall pictures can be made visible with a reflection techniques.

Almost at the same time, experiments were performed at the National Institute of Information and Communications Technology (NICT) in Tokyo on painting mock-ups that were focused on acquiring THz spectra of various artists' materials, such as pigments and binders, as well as the application of THz imaging to the analysis of artworks [26]. Spectral features in the THz region are due to molecular and intermolecular interactions, weak bonds and phonon absorptions. THz spectroscopy can be performed in the frequency domain (FDS) or time domain (TDS). It should be noted that NICT and the Riken have been the first institutions to make a spectral database on artists' materials, which included more than 200 spectra of products related with art materials, available online (`http://www.thzdb.org`). With the use of these spectral data, THz spectroscopy can be utilized to determine materials found in artworks, such as pigments with similar composition and the same color.

Besides the THz spectroscopic study of paints, THz stratigraphic and subsurface investigation of art paintings is also emphasized in the art conservation field. Jackson et al. were the first to use reflective THz imaging to observe the 8B graphite underdrawing of a water-based painting on plaster of Paris using spectral power integration between 0.25 THz and 0.75 THz [27]. Adam et al. show that it was possible to image the substructure of paintings on canvas by monitoring the time delay between reflections off different layers and also determine the thickness of the umber underdrawings [28]. In this study, the authors indicated that the smallest absolute thickness measurable with their THz-TDS system, which is about 50 μm by assuming a refractive index of 1.9 for raw umber. Furthermore, they also estimated that it was still possible to measure thicknesses of about 12 μm by means of the changes in the

Table 1.1: State-of-the-art THz imaging of actual art paintings

Ref.	Types	Painting Name	Year
[26]	Panel	*Badia Polyptych* by Giotto di Bondone	2010
[29]	Panel	*San Giovenale Triptych* by Masaccio	2015
[30]	Panel	*the Virgin with the Child and a Saint* in Sicily Italy	2015
[31]	Panel	*A Garden in front of a Country Seat* by David Teniers	2015
[32]	Panel	*The Lamentation over the Dead Christ* by Fra Angelico	2016
[33]	Easel	*Sacrifice to Vesta* by Francisco de Goya	2013
[34]	Easel	*The Dying Messalina and Her Mother* by Nicolai Abildgaard	2015
[35]	Easel	*Homme au chapeau* by Pablo Picasso	2015
[36]	Easel	*Santo Entierro de Nuestro Senor* altarpiece, Mexico	2017
[37]	Wall	Wall painting of Dazhao Monastery, China	2010
[38]	Wall	Wall painting of Catalhoyuk, Turkey	2013
[39]	Wall	Wall painting of Nebbelunde Church, Denmark	2015

time separation of 0.15 ps. However, in order to achieve these values, more elaborate signal processing methods are required.

Considering the application of THz imaging on actual art paintings, one of the most important application of THz imaging in the art conservation science is the case study performed at the end of 2008 on the panel painting *Polittico di Badia* by Giotto di Bondone, on display at the Uffizi Gallery in Florence, Italy [26]. This study could be considered as the first application of THz reflective imaging on an actual tempera panel painting which belongs to one of the most important museums in the world. Gilded panel paintings are a particular kind of art developed in the early medieval age. With THz reflective imaging, gold leaves beneath the paint layers were clearly observed and the layered structure of this panel painting was also revealed based on the reflections in the time domain. During the early Renaissance, painters started to prefer canvases to panels as supports for their paintings because they were much affordable and could be folded for more convenient transportation. Compared with wood panels, canvases are more transparent to THz waves, which enable THz imaging to identify hidden features, such as the artist's signature [33], under-drawings and modifications due the reuse of an earlier painting or canvas [34][31][35]. Portable and compact up-to-date THz-TDS systems also provide the opportunities for in-situ

analysis of wall paintings. THz imaging has been utilized to detect wall paintings whitewashed with lead white, which is opaque to infrared imaging and X-ray radiography. THz imaging can map pigments on wall paintings as well as evaluate the extent of cracks into the plaster [37][39]. The state-of-the-art studies of THz imaging for the NDE of actual art paintings are summarized in Table 1.1.

Besides the area of art paintings, THz imaging has also been applied for characterizing of features in stone sculpture and in architecture [40], wooden objects [41] and tree rings for dendrochonological purposes [42], clay artifacts [43], written papyrus [44], ancient mummies [45] and archaeological bones [46]. These very promising first results reported need to be extended to a more extensive set of case studies, in order to better refine the experimental methodologies.

1.3 Scope of the thesis

The objective of this thesis is to explore the potentials and enhance the capabilities of THz imaging for the NDE and material characterization in the field of industry and culture heritage conservation science.

Chapter 1 introduces the background of this thesis. The basic knowledge of THz radiation is briefly introduced. The motivation and research problems of this project are described. The state-of-the-art of the development and applications of THz imaging in the fields of industry and cultural heritage conservation science are also summarized in this chapter.

Chapter 2 presents the main equipment, THz time-domain spectroscopy (TDS) system, utilized in this project. The main imaging contrasts, based on which the THz results are presented, are briefly described.

Chapter 3 is devoted to the NDE of fiber-reinforced composites with THz imaging. Fiber-reinforced composites are widely used in the industry to take the place of conventional materials, such as metal. In this chapter, three case studies are presents.

The first case study shows the capability of THz imaging in providing 3D quantitative information for characterization of delaminations in glass-fiber reinforced composites. The spatial resolution, including the lateral resolution and the axial resolution of THz reflective imaging are discussed in detail in this study. The second case study takes the water-vapor influence into account, especially for THz characterization of small delaminations in woven glass-fiber reinforced composites. Wavelet de-noising is applied to cancel the noises due to the atmospheric water-vapor. In view of the difficulty and expense in purging with dry nitrogen to physically remove the water-vapor features in many cases, the demonstrated results will be of great interest for a range of laboratory- and field-based THz NDE applications. In the third case study, polarization-resolved THz imaging is firstly applied to a hybrid fiber-reinforced composite laminate. The evolution of intra- and inter-laminar damage throughout the thickness of the laminate subject to low-velocity impact is evaluated. Inter-laminar damage at the interface and the intra-laminar damage close to the same interface can be differentiated by taking advantage of the sensitivity of the carbon-fiber orientation to the THz polarization. Comparative studies with ultrasonic imaging are also involved in the chapter.

Chapter 4 focuses on developing advanced THz deconvolution techniques to enhance the capability of THz imaging for the stratigraphic characterization of multi-layered structures with optically thin layers in the THz regime. Generally, layers with thicknesses smaller than 100 μm cannot be easily resolved based on the raw THz signals, due to the depth-resolution achieved by a typical THz TDS system, which further limits the applications of THz imaging. Deconvolution, if applied properly, can yield sub-wavelength or sub-pulse-width depth resolution. In the context of THz imaging, three kinds of deconvolution methods are developed in this chapter. Conventional deconvolution, such as THz frequency-wavelet domain deconvolution (FWDD), which is based on inverse filtering is introduced. The depth-resolution achieved by

FWDD is about 55 μm in air. A case study for the characterization of various failure modes in polymer-coated with FWDD is also presented. However, depth-resolution achieved by FWDD cannot satisfy the real applications of THz imaging. In order to further enhance the depth-resolution, sparse representation is exploited, and sparse deconvolution based on an iterative shrinkage algorithm is developed. With an up-sampling approach, sparse deconvolution with super-resolution is also developed to overcome the time resolution limited by the sampling period in the measurement. A simple but effective time-domain model for describing the temporal pulse spreading due the frequency-dependent loss is also designed and introduced into the algorithm, which significantly improves the performance of sparse deconvolution in processing time-varying pulses during the propagation of THz waves in materials. The depth-resolution achieved by sparse deconvolution is about 45 μm in air. Finally, a novel method for enhancing the depth-resolution of THz deconvolution based on autoregressive spectral extrapolation is developed. An autoregressive process is modeled based on the THz frequency components with high SNR, and the missing frequency components in the low SNR regions are extrapolated based on the autoregressive model. In this way, the entire THz frequency spectrum of the impulse response function is recovered. This method is able to provide a 'quasi-ideal' impulse response function, and therefore, significantly enhances the depth-resolution for resolving optically thin layers in the THz regime. The depth-resolution achieved by this method is about 27 μm in air. The deconvolution techniques developed and presented in this chapter greatly enhance the capability for resolving optically thin layers in the THz regime, and provide a powerful tool to the entire THz community for a broad applications.

Chapter 5 is addressed to THz reflectometry of art paintings. Based on the advanced deconvolution techniques developed in Chapter 4, THz reflectometry with enhanced depth-resolution presents great potentials for the characterization of stratigraphy in historical paintings in this chapter. Compared with other techniques, THz

reflectometry can provide 3D global mapping of the stratigraphy quantitatively. Two historical paintings are well-studied via THz reflectometry. The first one is a 19th century Italian oil painting on paperboard, *After Fishing*. Based on the deconvolved signals achieved by FWDD, the stratigraphy and subsurface features are clearly revealed. The second historical painting is a 17th century Italian easel painting, *Vièrge en priere*. Sparsity-based THz reflectometry is applied to characterize the detailed stratigraphy. Based on the sparsity-based deconvolved signals, the detailed layer structure, including the canvas, the ground, imprimatura, underpainting, pictorial, and varnish layers are clearly identified. In addition, a hitherto unidentified restoration of the varnish has been found. It is important to note that, it is the first time to our knowledge THz reflectometry has resolved multiple layers in an easel paintings. Based on this work, the full promise of THz reflectometry to provide a global and detailed account of an easel painting's stratigraphy has been unlocked by exploitation of the sparse deconvolution.

Chapter 6 is divided into three sections. Firstly, the conclusion part summarizes the results and contributions of this thesis. Secondly, the further possible research directions are proposed in the perspective part. The peer-reviewed publications achieved and conferences attended during the time of Ph.D. study are listed in the end of this chapter.

CHAPTER 2
EQUIPMENT AND IMAGING CONTRASTS

This chapter gives a brief introduction of the main experimental equipment, as well as the basic imaging contrasts utilized in this thesis.

2.1 Terahertz time-domain spectroscopy system

A THz time-domain spectroscopy (TDS) and imaging system (Teraview TPS Spectra 3000) is employed in this thesis, shown schematically in Fig.2.1. The GaAs photoconductive antenna is excited by an ultrafast (femtosecond) laser to produce roughly single-cycle THz pulses with bandwidth extending from 60 GHz to 3 THz. The ultrafast laser used here is an Er-doped fiber laser that emits 780 nm pulses with sub-100 femtosecond pulse duration at a repetition rate of 100 MHz and has an average output power in excess of 65 mW. Coherent detection of the THz radiation is performed in a similar photoconductive antenna circuit. By gating the photoconductive gap with a femtosecond pulse synchronized to the THz emission, a current proportional to the THz electric field is measured. By varying the optical path length, the reflected THz time-domain pulse can be sampled, resulting in both temporal amplitude and phase information. By taking the Fourier transform, spectroscopic information can be obtained. The power of the THz radiation used for measurement is below 1 μW, so no thermal strain is induced in the samples.

Both reflection and transmission imaging can be performed in this system. The sample is raster-scanned by a set of motorized stages moving in X and Y directions. The amplitude and phase of the THz pulse transmitted or reflected through the sample is measured. Refractive-index discontinuities as a function of depth produce multiple reflections off the various associated interfaces in the samples. These reflec-

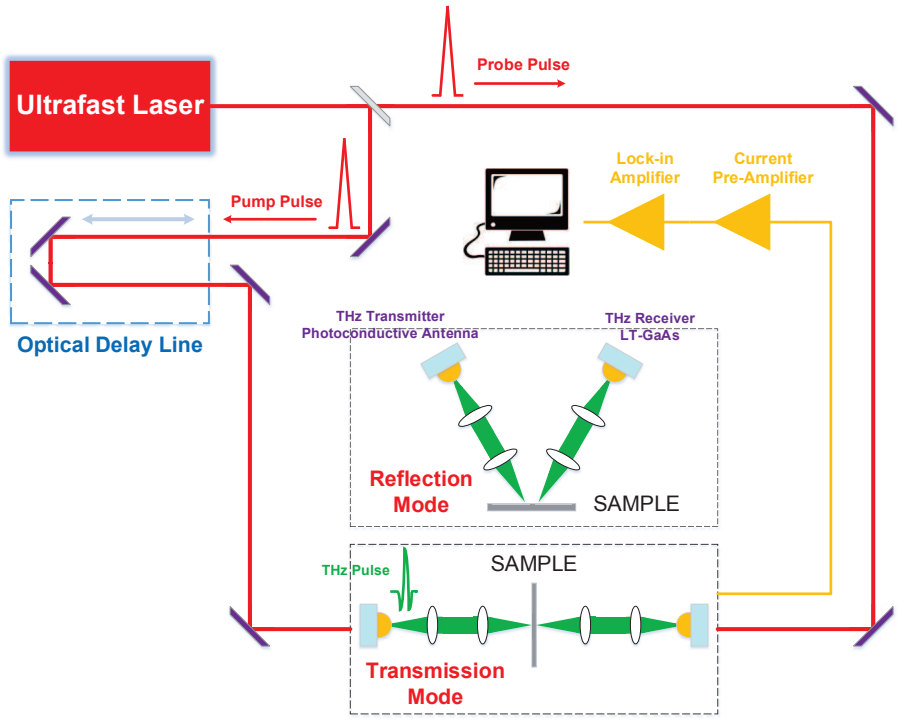

Figure 2.1: Schematic diagram of THz time-domain spectroscopy (TDS) system in both reflection and transmission configurations.

tions are manifested in the transmitted or reflected pulse containing several peaks at corresponding time delays. By analyzing these peaks together with knowledge of the refractive indices of the constituents, we can reconstruct the features of the samples.

In conjunction with the fiber probes on the existing TDS system, a remote stage is established to mount the probes and allow angular measurement and raster-scanning of a sample. The sample will be positioned on a horizontal motorized XY stage with the emitter and detector probes on manually repositioned mounts to allow angle coverage from reflection to transmission of the sample. This module, shown in Fig.2.2, has the following features: (1) Measurement in both specular and diffuse reflection; (2) Angular movement of the detector and emitter from near normal incidence accommodate reflections from rough surfaces. Manual adjustment of the incidence angle of the emitter will also be provided to change the incidence angle in reflection mode. (3) 30 cm by 30 cm scanning area. (4) XY point spacing down to 50 μ m step size

in the raster-scanning. (5) Purged lines to both emitter and detector probes.

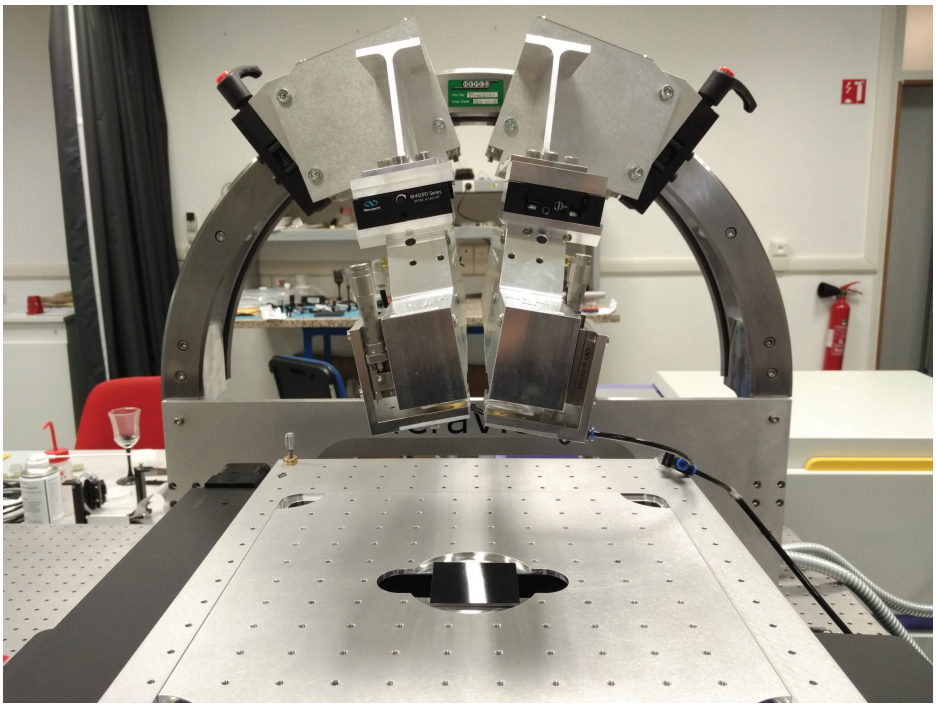

Figure 2.2: Image of the advanced variable angle reflection/transmission scan module.

2.2 Imaging contrast mechanisms

Generally speaking, the applications of THz imaging in the fields of industry and cultural heritage conservation science will most likely involve the the analysis of solid samples that are highly transparent to THz radiation and where contrast is achieved by a change in refractive index, absorption coefficient or scattering.

The main contrast mechanism that is typically exploited in THz imaging is the difference in refractive index between two materials. In time-domain THz imaging, the electric field E of the electromagnetic waves, rather than its intensity, is measured and the power reflectivity R is

$$R = \frac{{E_{interface}}^2}{{E_0}^2} = \frac{(n_1 - n_2)^2}{(n_1 + n_2)^2}, \tag{2.1}$$

where $E_{interface}$ denotes the electric field of THz waves of the reflection from the sample interface and E_0 is the reflection from a reference, and n_1 and n_2 are the refractive indices of the two media that the THz pulse is propagating through. As the THz pulse is propagating through the sample, a reflection will occur whenever there is a change in refractive index. This change in refractive index corresponds to the change of the dielectric constants.

Besides the change of the refractive index, in some crystalline materials, the intermolecular vibrational modes fall into the THz range, and therefore, a significant change in the absorption coefficient at specific frequencies can be observed, which correspond to the distinct frequencies of the vibrational modes. Polar liquids can lead to strong attenuation of the THz radiation, which provides the potential of THz imaging for moisture detection. Moreover, the conductivity σ of the sample is also related to the dielectric constants, which means, with increasing conductivity, both the absorption coefficient and refractive index also increase.

Besides the imaging contrast based on the amplitude of THz pulse, the phase information of THz pulse, such as the time of flight and time of arrival, can also be utilized as a contrast.

CHAPTER 3
TERAHERTZ NONDESTRUCTIVE EVALUATION OF FIBER-REINFORCED COMPOSITES

In this chapter, THz reflective imaging is systematically carried out for nondestructive evaluation of various damages or defects in fiber-reinforced composites. For glass fiber-reinforced composites, THz waves can be utilized to detect both surface and underlying defects, including mechanical/heat damage, voids, delaminations, intrusions, and moisture contamination. For carbon fiber-reinforced composites, due to the conductivity of carbon fibers, THz imaging can be used to detect surface or near-surface damages, such as impact-induced matrix cracking and fiber distortions/breakage.

This chapter presents three case studies. The first study is to characterize forced delaminations in glass fiber-reinforced composite laminates. This is a perfect example to show the capabilities of THz imaging for the NDE of fiber-reinforced composites. In this case, we find high-resolution, low-artifact THz C-scan and B-scan images locating and sizing the delamination in three dimensions, which enable us to determine the thicknesses of the delamination and of the layers constituting the laminate. Comparative analysis between THz imaging and ultrasonic C-scans with regard to spatial resolution is carried out demonstrating that THz imaging provides higher spatial resolution for imaging, and can be regarded as an alternative or complementary modality to ultrasonic C-scans for this class of glass fiber-reinforced composites.

The second study is to characterize a woven glass fiber-reinforced composite laminate with a small region of forced delamination, which is below the THz axial resolution, resulting in one featured echo with small amplitude in the reflected signal. However, low-amplitude components of the temporal signal due to the ambient water vapor produce features of comparable amplitude with features associated with the

delamination, which suppress the contrast of THz C- and B-scans. Wavelet shrinkage de-noising is performed to remove water-vapor features, leading to enhanced THz C- and B-scans to locate the delamination in three dimensions with high contrast.

The third study is novel, as the THz polarization is employed to enhance the imaging capability of THz radiation. In this study, THz reflective imaging is applied to characterize a hybrid fiber-reinforced composite laminate subject to low-velocity impact. The hybrid fiber-reinforced composite laminate comprises unidirectional glass/epoxy and carbon/epoxy plies with a cross-ply stack pattern. Both impact-induced intra- and inter-laminar damages are successfully detected, and the damage evolution throughout the thickness is also evaluated. The interaction between the THz polarization and carbon fiber orientation is investigated in detail. Inter-laminar damage at the interface and the intra-laminar damage close to the same interface can be differentiated via polarization-resolved imaging.

3.1 Terahertz imaging of forced delaminations in glass fiber-reinforced composites

3.1.1 Terahertz 3D quantitative imaging

Glass fiber-reinforced composite laminates in polyetherimide resin are studied via THz reflective imaging in this section. The samples contain eight layers with a total thickness of 1.85 mm, and the fiber volume fraction is about 50 vol%. Two different circular sizes of defects with diameter 6 mm and 12 mm were intentionally introduced by adding release Teflon-film disks, with thickness approximately 250 μm, to create forced delamination. 64 samples were obtained by cutting the laminate and the defects are spread throughout the laminate and are inserted between various layers.

Reflective pulsed imaging was performed on all the 64 samples. THz C-scan image of sample 1 in reflection is shown in Fig.3.1. The image is acquired with a 0.2 mm spatial step size over the image domain. The contrast mechanism chosen for this image

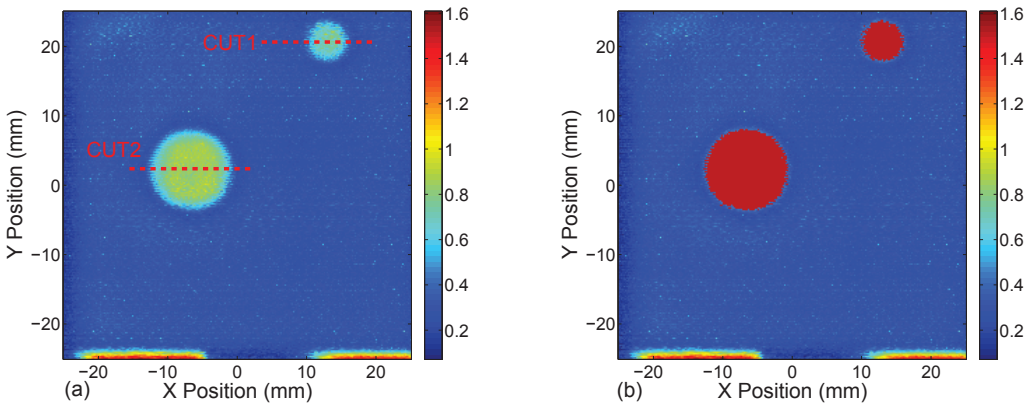

Figure 3.1: (a) THz C-scan image of sample 1 with the contrast mechanism associated with the peak-to-valley difference of the reflected THz pulse within the time window 13-20 ps. (b) THz C-scan image after applying 50% rule for sizing the delaminations.

is the difference between the maximum and minimum values of the reflected THz pulse in a selected time slice between 13 ps and 20 ps. This was chosen to maximize contrast between regions containing delamination and regions without delamination. The THz pulse encountering a region containing a delamination leads to higher difference between the maximum and minimum reflected amplitude in the relevant time window due to the higher difference of the refractive index, which corresponds to the lighter two circular regions in Fig.3.1(a). 50% rule or 6 dB drop method can be utilized to estimate the size of the delamination. This method locates the pixel with the highest value in the C-scan image and assigns this a value of 100%, then colors all pixels red that have a value of at least 50% of the maximum. Fig.3.1(b) shows the C-scan image after applying this method. The dimension of THz focal spot mainly determines the accuarcy of sizing the delamination. Diffraction effects at the edge of the Teflon film may also be responsible for the errors of sizing the delamination in the C-scan images.

THz B-scan images in Fig.3.2 provide information in depth along cross-sections (labeled Cut 1 and Cut 2 in Fig.3.1(a)) through the two delaminations. Eight layers can be clearly identified. The narrow bright band near an optical delay of 10 ps coincides with the top surface of the sample on the side of the incident THz pulses.

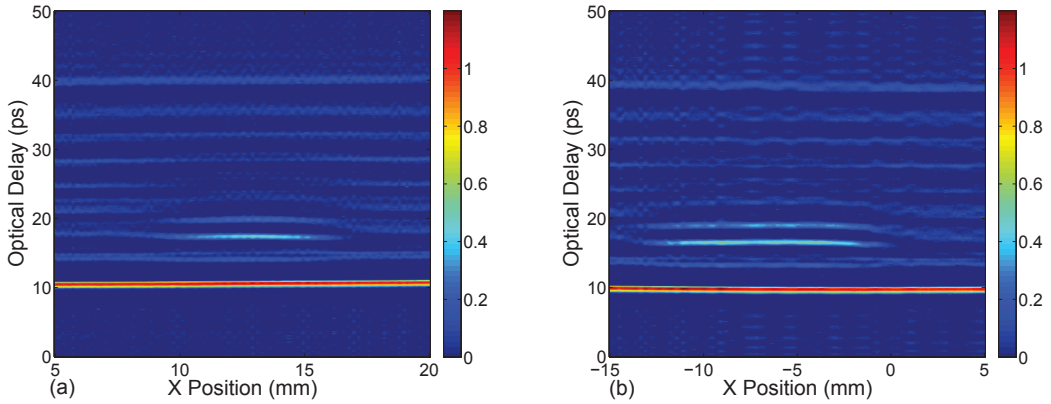

Figure 3.2: THz reflection B-scan images through the cross-sections labeled in Fig.3.1(a) with the contrast mechanism associated with the amplitude of the reflected THz pulse.

The localized lighter bands between resin layers 2 and 3 correspond to the depth locations of the delaminations. Besides these two-dimensional imaging results, Fig.3.3 shows the three-dimensional THz image of the sample which clearly exhibits the locations of the delaminations.

A detailed investigation of the data in Fig.3.4 provides *quantitative* information on the lamina and delamination thicknesses. In this case, these distinguishable reflections characterized by their optical delay in conjunction with the refractive indices of the constituent materials enable us to identify layer thicknesses and locations. With THz spectroscopy, the refractive index of the sample can be obtained across the THz band, which varies little in this range and has the value of 2.16 in the frequency range from 0.3 THz to 1.3 THz. Hence, the thickness of any single resin layer can be calculated. Similarly, using the published value of the refractive index of Teflon and the time delay $\Delta\ t$ shown in Fig.3.4 between the reflections associated with the interfaces between the Teflon and the adjoining polyetherimide layers, the thickness of the Teflon film can also be calculated.

THz images of all 64 samples are obtained with the delaminations identified and the thicknesses of Teflon film disks measured. Representative results based on the THz

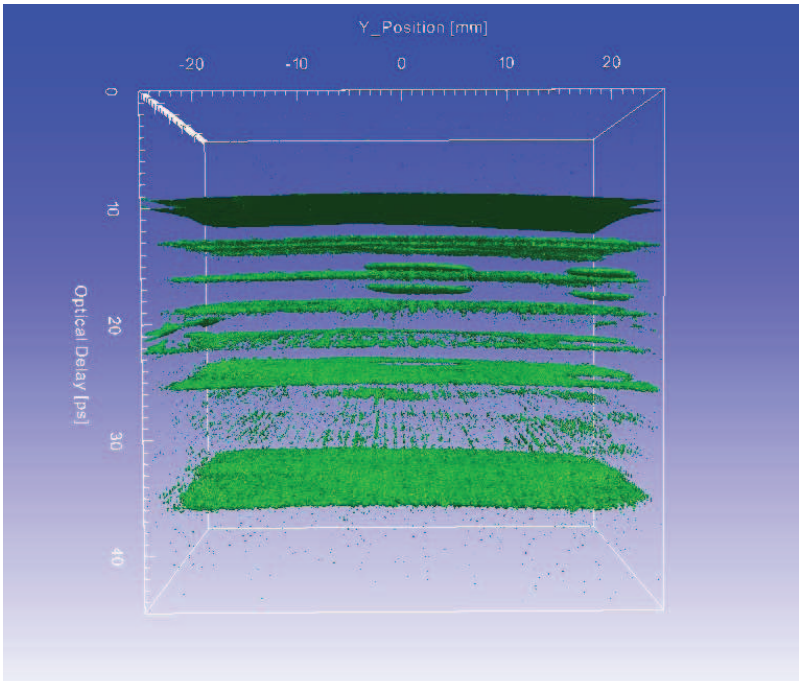

Figure 3.3: Three-dimensional THz imaging for sample 1.

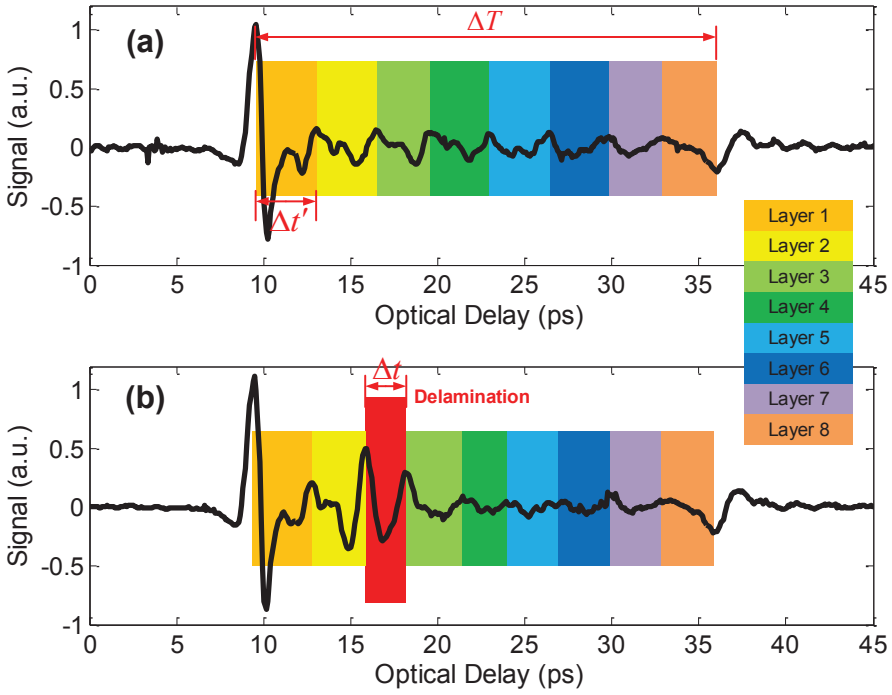

Figure 3.4: Time traces of detected reflected THz signals (a) in the absence of delamination and (b) with delamination.

images on samples with various defect patterns are shown in Fig.3.5 corresponding to the THz C-scans, B-scans, and time-domain waveforms. All the detailed results and analysis show that THz imaging can provide low-artifact images (time domain C-scan and B-scan) and thus three-dimensional information as well as quantitative information on delamination in glass fiber-reinforced composite laminates.

3.1.2 Comparison with ultrasonic C-scans

A customer-designed ultrasonic scanner fabricated by Inspection Technology Europe BV is used for ultrasonic C-scan experiment. The transducer chosen for this investigation is a focused-immersion transducer with a manufacturer-provided central frequency of 5 MHz considering both the attenuation and resolution. Ultrasonic C-scans were performed on the samples with water coupling under both transmission (pitch-catch) mode and reflection (pulse-echo) mode.

Fig.3.6 shows the ultrasonic C-scan images for samples 51 and 57 in both transmission and reflection, showing that ultrasonic C-scans can also successfully identify the delamination areas. The contrast for ultrasonic C-scans are based on the absolute value of the amplitude of the ultrasonic transmitted or reflected wave. The typical transmitted and reflected waveforms obtained with and without the delamination are compared in Fig.3.7. Note the much larger timescale of the ultrasound pulses versus the THz pulses. In the transmission mode shown in Fig.3.7(a), the transmitted waveform in the windowed time slice is chosen to provide sharper contrast for the ultrasonic C-scans, because this transmitted waveform travels the samples three times. In the reflection mode shown in Fig.3.7(b), the second echo which is also in the windowed time slice, is chosen to obtain the ultrasonic C-scan images, since the first echo is mainly the specular reflection from the sample surface.

With the ultrasonic waveforms in reflection mode, the ultrasonic B-scan images can also be obtained, shown in Fig.3.8. In the B-scan images, we can still clearly

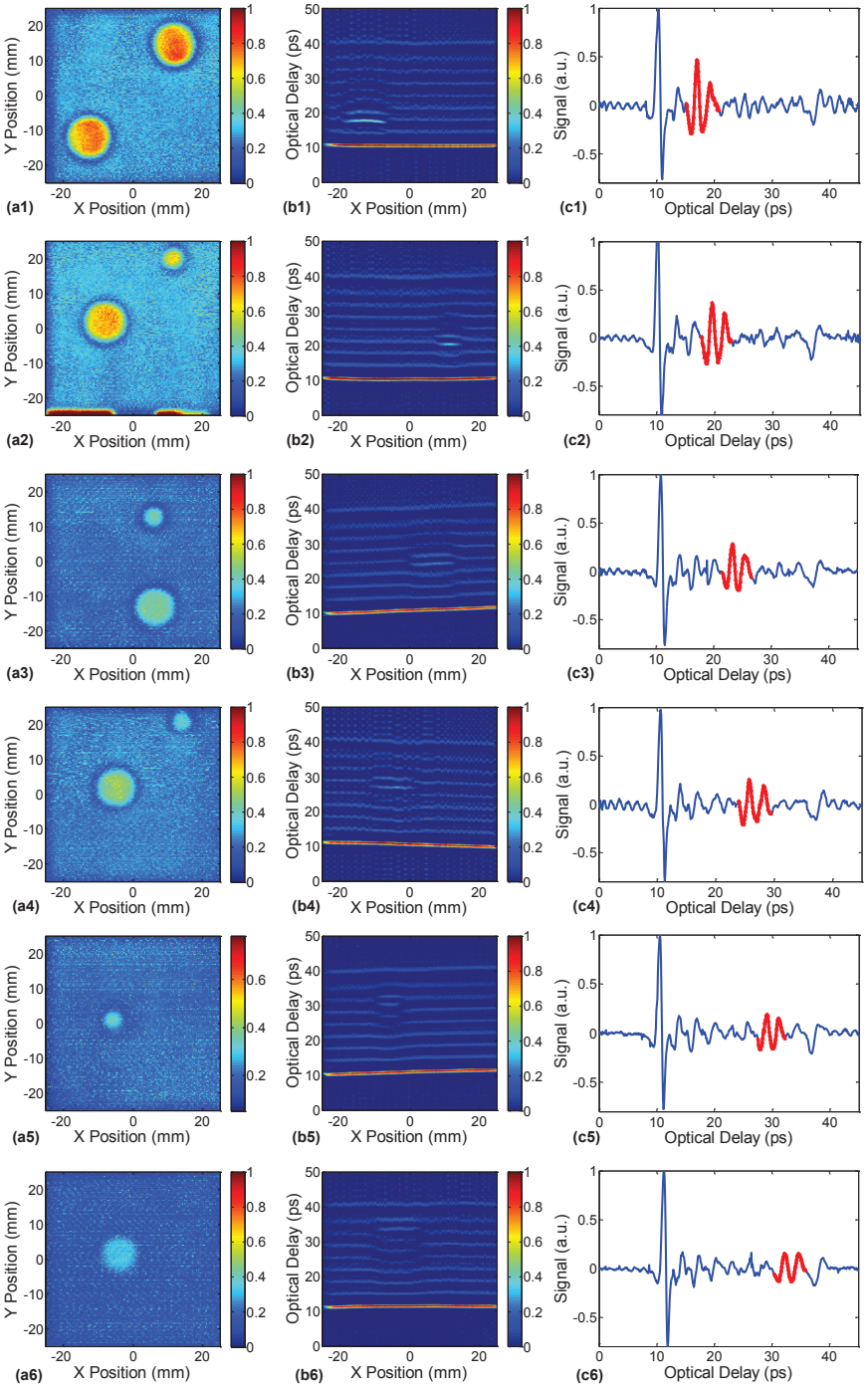

Figure 3.5: THz reflection images of representative samples. THz C-scans (a1) to (a6), B-scans (b1) to (b6), and time-domain waveforms (c1) to (c6) corresponding to samples 23, 10, 60, 46, 51, and 57, respectively.

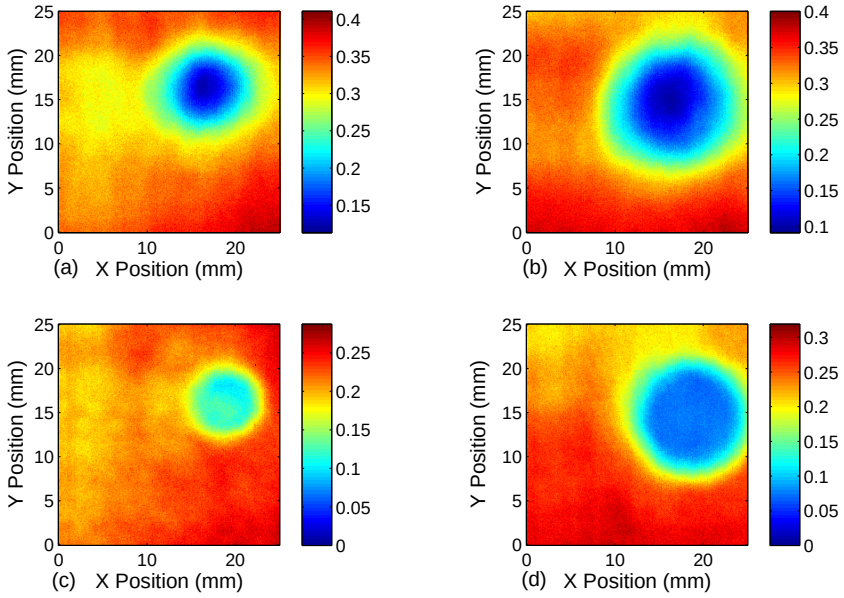

Figure 3.6: Ultrasonic imaging C-scan results for samples 51 and 57. (a) 51 in transmission, (b) 57 in transmission, (c) 51 in reflection, and (d) 57 in reflection modes.

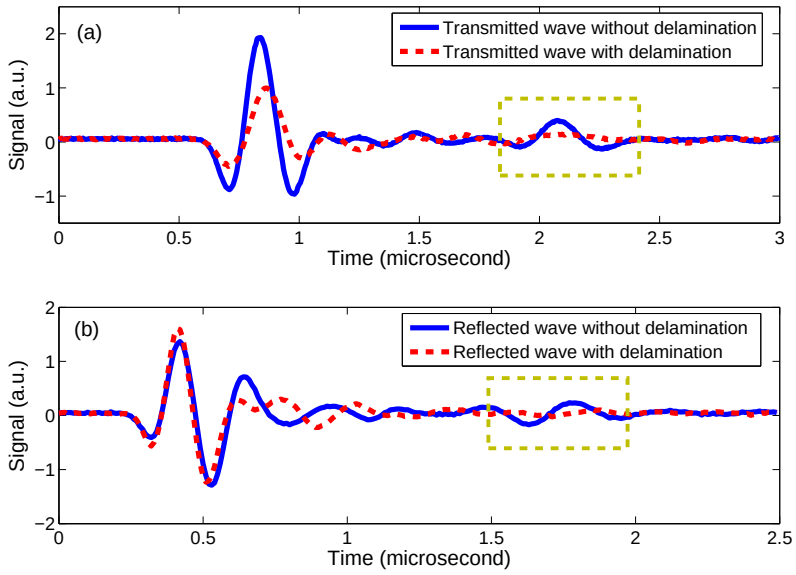

Figure 3.7: Ultrasonic time-domain waveforms without and with delamination for sample 51 in (a) transmission mode and (b) reflection mode.

see the delamination region and can roughly locate the delamination in depth. Four signal peaks can be observed between the echoes from the top and bottom of the sample. However, unlike the THz B-scans, these four peaks cannot be identified as the layers in the samples. Overlapping echoes coming from the top surface, the bottom surface and the interfaces between different layers and delaminations cause the local maximums in the signal making it difficult to identify the laminae and the delaminations inside the samples from the ultrasonic B-scans.

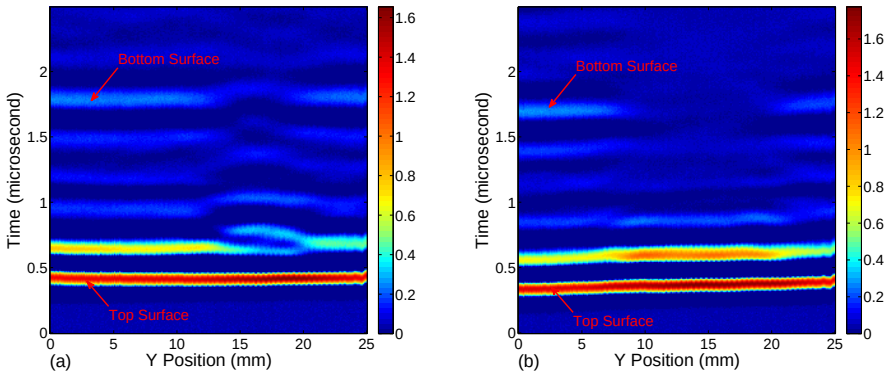

Figure 3.8: Ultrasonic B-scan images for (a) sample 51 with x position at 18 mm, (b) sample 57 with x position at 18 mm.

Comparison between THz imaging and ultrasonic C-scans can be performed with respect to the spatial resolution of images obtained from both cases. Spatial resolution contains two parts: lateral and axial resolution. Lateral resolution is the minimum distance that can be differentiated between two point scatters across the scan plane. The lateral resolution is high when the focal spot size of the beam is small. For THz imaging, the focal spot size of THz beam is frequency dependent, the higher the frequency, the smaller the spot size. For the THz TDS system used in this thesis, the lateral resolution at the surface is about 0.3 mm at 1 THz. For ultrasonic C-scans, lateral resolution is 1.95 mm for the focused transducers at 5 MHz. Therefore, THz imaging can achieve higher lateral resolution than ultrasonic C-scans, which can be corroborated by the comparison between the results of sizing the delamination

by both techniques. THz imaging can provide more accurate results of sizing the delamination than ultrasonic C-scans, especially for the small delamination.

Axial resolution is the minimum distance that can be differentiated between two points in depth. Axial resolution is equal to half the spatial pulse length; it is high when the spatial pulse length is short. For THz imaging, the axial resolution is determined by

$$d = \frac{c\Delta T_w}{2n}, \tag{3.1}$$

where $\Delta\ T_w$ is the temporal width of the THz pulse. The axial resolution in the THz TDS system is estimated to be about 45 μm with $\Delta\ T_w = 0.65$ ps. For ultrasonics, thee spatial pulse length is equal to the product of the number of cycles in a pulse and the wavelength. The acoustic wavelength at a frequency of 5 MHz is about 500 μm in the glass fiber composite samples. The different axial resolution can also be identified from THz and ultrasonic waveforms. As mentioned before, the various time-domain features associated with the THz pulse encountering each lamina interface as well as the delamination. By contrast, the timescale of ultrasonic pulses are quite different. The relatively long time of duration of ultrasonic pulse leads to overlapping echoes in the small thickness-to-wavelength ratio samples and makes it difficult if not impossible to clearly identify features on the length scale of the laminae thickness and delamination. The fundamental point is that the ultrasonic axial resolution is not sufficient to obtain detailed B-scan images in this case. Employing considerably higher acoustic frequencies with shorter wavelength, but the attenuation in this frequency range is prohibitively high in the samples, which in turn led to no discernible second echo signal in reflection.

Therefore, THz imaging can provide higher spatial resolution than the ultrasonic C-scan technique for imaging the glass fiber-reinforced composite samples. Ultrasonic axial resolution is not sufficient to provide the quantitative information in depth to identify the number of laminae nor the thickness of the delamination.

3.2 Enhanced terahertz imaging of small delaminations in woven glass fiber-reinforced composites

In this study, THz imaging is applied to characterize small forced delamination in woven glass fiber-reinforced composites. The forced delamination is created by inserting Upilex film with thickness only about 25 μm. THz echoes reflected from the front and rear interfaces of the forced delamination cannot be readily separated in the raw signal, leading to only one distinguishable echo in time associated with the delamination. The amplitude of this featured echo is small, and is comparable to the fluctuations resulting from the ambient water vapor. Wavelet shrinkage de-noising is performed here to suppress these fluctuations and to obtain enhanced THz C- and B-scan images for characterizing the delamination in three dimensions.

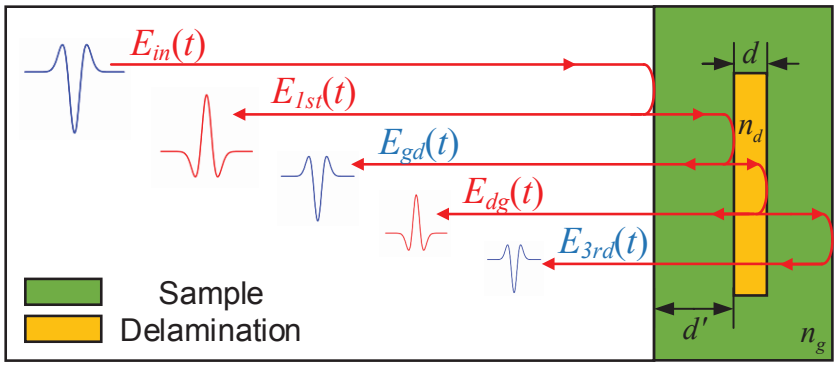

Figure 3.9: Estimated reflected THz pulses in region with delamination indicating the observed features associated with reflections off various interfaces.

In the case of a sample with forced delamination, the temporal reflected THz pulses can be estimated, based on considerations shown schematically in Fig. 3.9. For normal incidence on an interface between two media with refractive indices n_i and n_j, the amplitude reflection coefficient r_{ij} and transmission coefficient t_{ij} are

$$r_{ij} = \frac{n_i - n_j}{n_i + n_j} \tag{3.2}$$

$$t_{ij} = \frac{2n_i}{n_i + n_j} \tag{3.3}$$

In our study, the subscripts (i,j) for different media are: a-air, g-glass fiber-reinforced composites and d-forced delamination.

The reflected THz time-of-flight waveform is composed of the echoes off interfaces between various media. In principle, the temporal separation between echoes is proportional to the distance between interfaces (the thickness of the forced-delamination). And the minimum distance discernable from the signal, *viz.* the axial resolution d_{min}, is

$$d_{min} = \frac{c\Delta T}{2n_d} \tag{3.4}$$

where c is the *in-vacuo* speed of light, ΔT is the temporal width of the THz pulse, and n_d is the group refractive index of the medium within the forced delamination. When the forced-delamination thickness is larger than the axial resolution, two distinct THz echoes from the consecutive interfaces are well separated in time; otherwise, the two THz echoes cannot be easily distinguished. Therefore, in our case with thin delaminations below the axial resolution, the reflected THz waveform $E_{THz}(t)$ is expected to be composed of three clear features,

$$E_{THz}(t) = E_{1st}(t) + E_{2nd}(t) + E_{3rd}(t) \tag{3.5}$$

The first and third terms, $E_{1st}(t)$ and $E_{3rd}(t)$, correspond to Fresnel reflections at the bottom and top surfaces of the sample. And the second term echo, $E_{2nd}(t)$, is the superposition of the two echoes returned from the interfaces associated with the delamination. In our case, we neglect the negligible dispersion in the relevent spectral range, so this featured echo $E_{2nd}(t)$ can be expressed based on the incident THz pulse

$E_{in}(t)$,

$$\begin{aligned} E_{2nd}(t) &= E_{gd}(t) + E_{dg}(t) \\ &= t_{ag} r_{gd} t_{ga} E_{in}(t - \frac{2n_g d'}{c}) e^{-2\alpha d'} \\ &+ t_{ag} t_{gd} r_{dg} t_{dg} t_{ga} E_{in}(t - \frac{2n_g d'}{c} - \frac{2n_d d}{c}) e^{-2\alpha' d'} e^{-2\alpha d} \end{aligned} \tag{3.6}$$

with d' the distance between the delamination and the surface of the sample, d the thickness of the delamination, α' and α the absorption coefficients in the glass fiber-reinforced composites and in the forced delamination. Because the signs of the reflection coefficients (r_{gd} and r_{dg}) at the interfaces between the glass fiber-reinforced composite and the delamination are opposite, the two echoes $E_{gd}(t)$ and $E_{dg}(t)$ will tend to cancel with each other, leading to the small amplitude of the associated signal $E_{2nd}(t)$. Moreover, the signal amplitude decreases with decreasing delamination thickness [47].

3.2.1 Influence of water vapor

In the THz frequency region, many polar gases possess pronounced rotational transitions, leading to numerous spectral resonances. Water vapor, as the third most abundant gas in the terrestrial atmosphere, is known to have many rotational resonances in the THz frequency region [48]. Therefore, THz imaging of a sample in the open air results in a combination of the sample's spectral features and ambient water-vapor resonances. In the time domain, this results in ringing—THz fluctuations—after the dominant THz pulse [49]. Provided the features of interest are sufficiently large, these fluctuations can be ignored. However, when the real features from the sample are of comparable amplitude, they may be obscured by features associated with water vapor, leading to THz images with low contrast. Clearly, ridding the system of ambient water vapor, such as by purging with dry nitrogen, can suppress these fluc-

tuations; however, it is not always possible to enclose the entire THz beam path in many practical laboratory and field applications. Several numerical approaches have been studied to remove the water-vapor fluctuations, including adaptive deconvolution [49], absorbance spectrum fitting [50], artificial neural networks [51], and wavelet de-noising [52].

3.2.2 Wavelet de-noising

Wavelet shrinkage is a signal de-noising technique based on the idea of thresholding the wavelet coefficients. Mittleman [53] first suggested the use of wavelet transforms for THz signal processing because the THz pulse is similar in form to common wavelet basis functions. Compared with the general discrete wavelet transform (DWT), the stationary wavelet transform (SWT) is never sub-sampled and instead up-sampled at each level of decomposition. SWT decomposes a $1D$ signal $x(n)$ into the approximation coefficients vector $cA_{k,l}$ and detail coefficients $cD_{k,l}$ by convolving with a low-pass filter Ψ and a high-pass filter Φ along the temporal axis at each level [54], shown in Fig. 3.10. Wavelet coefficients with small absolute values can be considered as noise, and wavelet coefficients with large absolute values are regarded as the main featured information of the signal. Removing the small absolute value coefficients by thresholding and then reconstructing the signal is expected to produce a signal in which the contribution of noise has been reduced.

In general, wavelet shrinkage de-noising with soft thresholding is performed via the following procedure [54, 55]:

1. Determine the wavelet coefficients by taking the SWT,

$$[cA, cD] = SWT(x(n)) \tag{3.7}$$

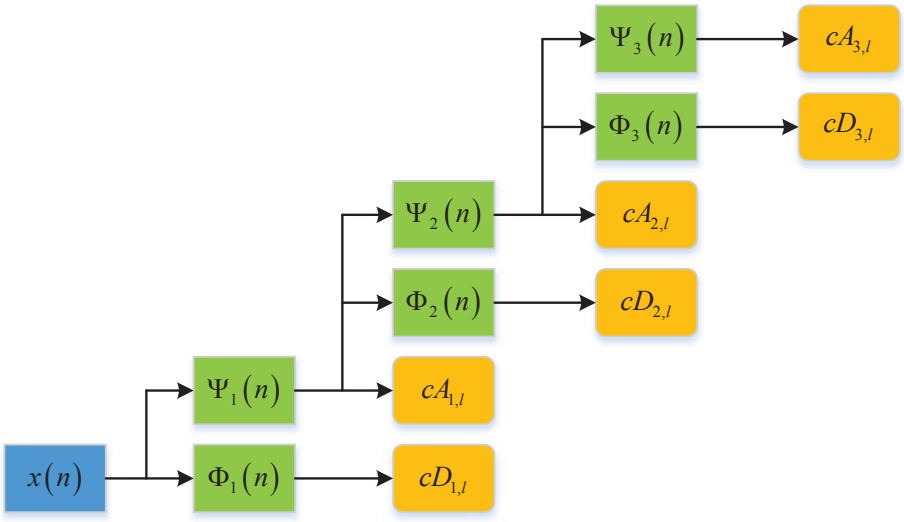

Figure 3.10: Schematic level-3 decomposition of a signal with stationary wavelet transform (SWT).

2. Calculate the threshold value T,

$$T = \sigma\sqrt{2log_e N} \tag{3.8}$$

where σ is the noise level and N is the number of sampling points.

3. Threshold the wavelet coefficients $cD_{k,l}$ with solft-thresholding

$$c\hat{D}_{k.l} = \begin{cases} cD_{k,l} - T & cD_{k,l} \geq T, \\ cD_{k,l} + T & cD_{k,l} \leq -T, \\ 0 & |cD_{k,l}| < T. \end{cases} \tag{3.9}$$

4. Perform the inverse stationary wavelet transform ($ISWT$) to recover the time domain signal $\hat{x}(n)$,

$$\hat{x}(n) = ISWT([cA, c\hat{D}]) \tag{3.10}$$

3.2.3 Enhanced terahertz imaging with wavelet de-noising

A woven (2 × 2 twill weave) E-glass fiber reinforced nylon matrix laminate, shown in Fig. 3.11, is employed in this study. The dimensions of the laminate are 50 mm (length) × 50 mm (width) × 1.54 mm (thickness), and the surfaces are flat. The laminate is composed of three glass fabric layers stacked as (0°/90°) with fiber volume fraction about 50 vol.%. The size of the fiber bundles is 1200 tex (weight in grams per kilometer of yarns), shown in the inset of Fig. 3.11. Delamination was introduced between the first and second fabric layer by incorporating a Upilex (ultra-high heat-resistant polymide) release film disk with thickness about 25 μm and diameter about 12 mm prior to consolidation of the laminate.

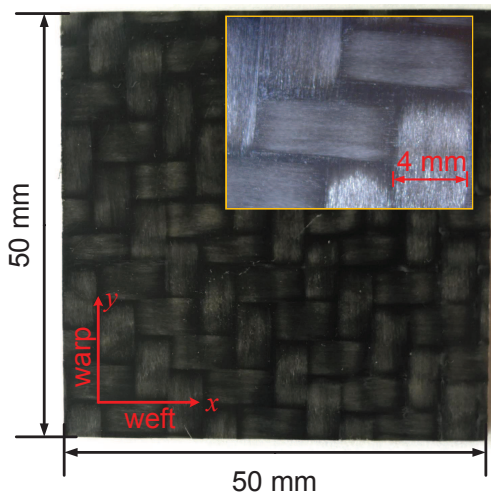

Figure 3.11: The photograph of the woven E-glass fiber reinforced nylon matrix laminate. Inset: Amplification of the photograph to show the size of the fiber bundles.

THz imaging is performed in reflection mode at almost normal incidence from the bottom surface of the sample. The polarization of the THz beam is in the y direction, which is parallel to the warp direction of the sample. Experiments were carried out in an air-conditioned laboratory with temperature at 22°C. The humidity in the laboratory was 48%, but no provision was made for backfilling with dry nitrogen. Before imaging the sample, a THz reference signal was recorded by setting a metal

plate at the sample position. The reference THz pulse and spectrum are shown in Fig. 3.12. Pronounced fluctuations behind the main THz pulse due to atmospheric water-vapor absorption can be clearly observed. The sample is raster-scanned by a set of motorized stages moving in the x and y directions with a 0.2 mm spatial step over a 45 mm $\times$ 45 mm region of the sample. Each recorded reflected THz pulse contains 4096 data points and the signal is averaged over 5 shots per pixel.

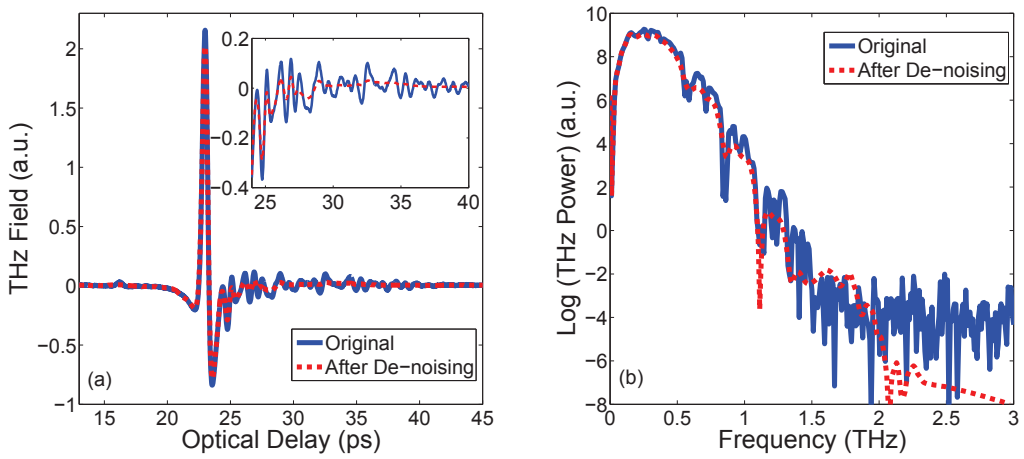

Figure 3.12: THz reference signal with and without wavelet de-noising in (a) time domain and (b) frequency domain. The inset in (a) shows the fluctuations in the signal due to ambient water vapor.

Before performing wavelet shrinkage de-noising to the reflected THz pulses, we implemented a numerical parameter fitting method based on multiple regression analysis [15] to make sure that the echoes between the featured echoes corresponding to the bottom and top surfaces in the reflected THz signals are mainly due to the water vapor. A typical measured THz waveform without delamination, shown in Fig. 3.22, is considered as the objective function. Echoes reflected from the bottom and top surfaces of the samples can be clearly identified in this reflected waveform. (Multiple reflections are small and correspond to features in the reflected THz pulse that occur at later times.) A model function is defined to simulate the objective function as

$$E_{model} = aE_{in}(t - \Delta t) \tag{3.11}$$

where a and Δt are the regression parameters. We consider the original THz reference signal shown in Fig. 3.12 as the incident THz pulse $E_{in}(t)$ and ignore the echo from the top surface in this simulation. In short, we use an amplitude-decreased and time-shifted reference signal to match the first echo in the measured signal. Initial values should be carefully set so that the regression analysis can converge to a characteristic global minimum. Then multiple regression analysis with least-squares minimization is performed to estimate the regression parameters, and the results are shown in Fig. 3.13. Signals between the Fresnel reflections from the bottom and top surfaces of the sample match quite well with the model function with regression parameters. The coefficient of determination R^2 is also used here to provide information about the goodness of fit. In the time slice between 24 and 34 ps, the coefficient of determination equals to 0.9827, which demonstrates that these features mainly originate from the water vapor.

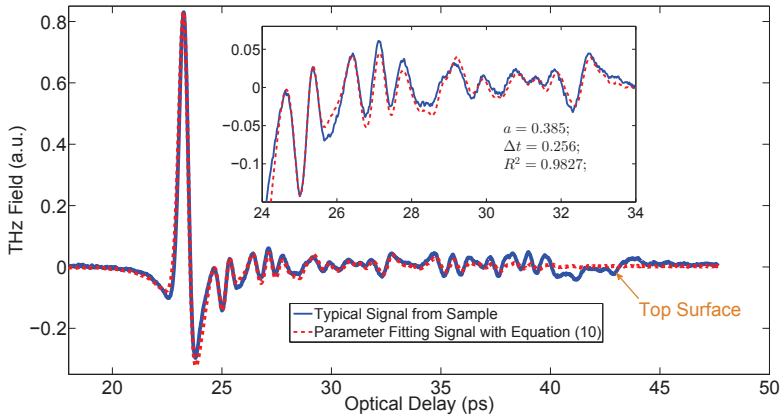

Figure 3.13: Multiple parameter regress analysis of measured THz waveform without delamination to identify the water-vapor effect.

It should be noted that featured echoes corresponding to the reflections from the internal interfaces between the fabric layers cannot be identified in the typical THz reflected waveform. Due to the complex internal structure of the woven fiber-reinforced composites with big size of fiber bundles, the echoes reflected from the internal inter-

faces are very small (comparable or even smaller than the features introduced by the water vapor), and these small echoes are immersed in the reflected waveform. This is also the reason why a small mismatch can be found in Fig. 3.13 in the time slice between 27 and 29 *ps*, which corresponds to the location of the first internal interface between fabric layers.

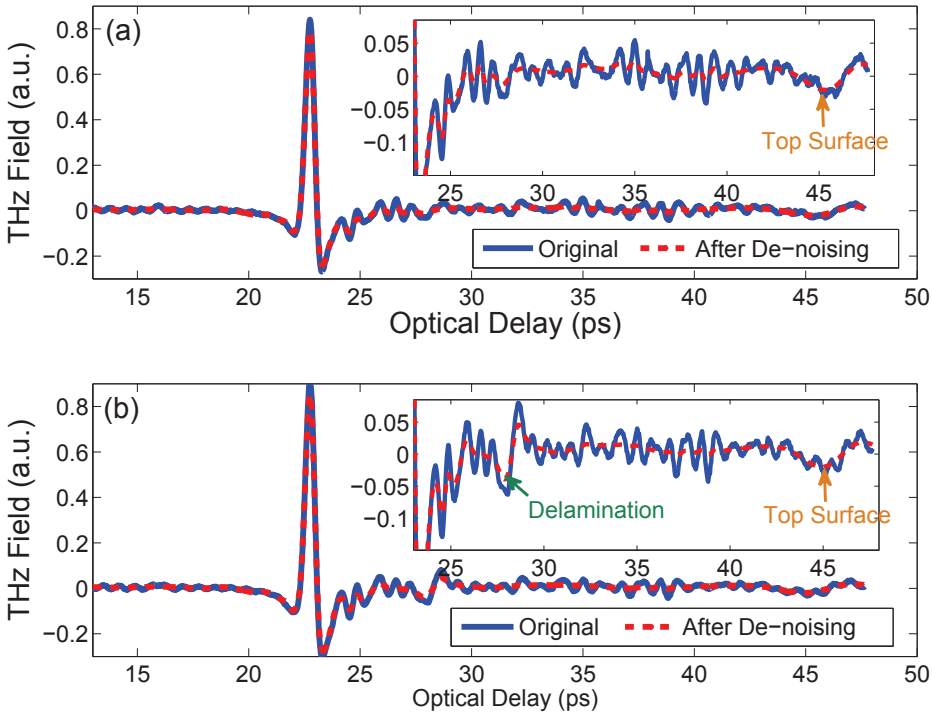

Figure 3.14: Typical reflected THz waveforms with and without wavelet de-noising in the region (a) without and (b) with delamination.

Next, wavelet shrinkage de-noising is performed to process the reference signal and the THz pulses in regions with and without delamination, respectively. In this study, we choose the *symlet* (sym4) wavelets, which are a modified form of *Daubechies* wavelets. A maximum level of 7 is used for the wavelet decomposition as no significant improvement was observed for higher levels to justify the extra computational expense. The position of the noise interval is set to the region of the fluctuations just after the main THz pulse in the original reference signal, which locates in the

temporal region between 24 and 40 ps.

The time-domain THz reference signal and its spectrum after wavelet de-noising are shown in Fig. 3.12 for comparison. In time domain [Fig. 3.12(a)], most of the water-vapor fluctuations are removed without losing much energy in the main THz pulse. In the frequency domain [Fig. 3.12(b)], the major water-vapor absorption dips are successfully suppressed.

To provide B- and C-scans, we processed the THz raw data obtained by raster-scanning with wavelet de-noising for each pixel. Typical reflected THz pulses without and with delamination and the comparison before and after wavelet de-noising are shown in Fig. 3.14. The echo associated with delamination [Fig. 3.14 (b)] can be located with small amplitude comparable to the level of fluctuations. After wavelet de-noising, most of the fluctuations between the echoes from the bottom and top surfaces are successfully removed. However, the features associated with the structure, including the echoes from the delamination and the bottom and top surfaces of the sample, are evident. In this way, the signal-to-noise ratio is also be increased providing higher contrast for THz C- and B-scans.

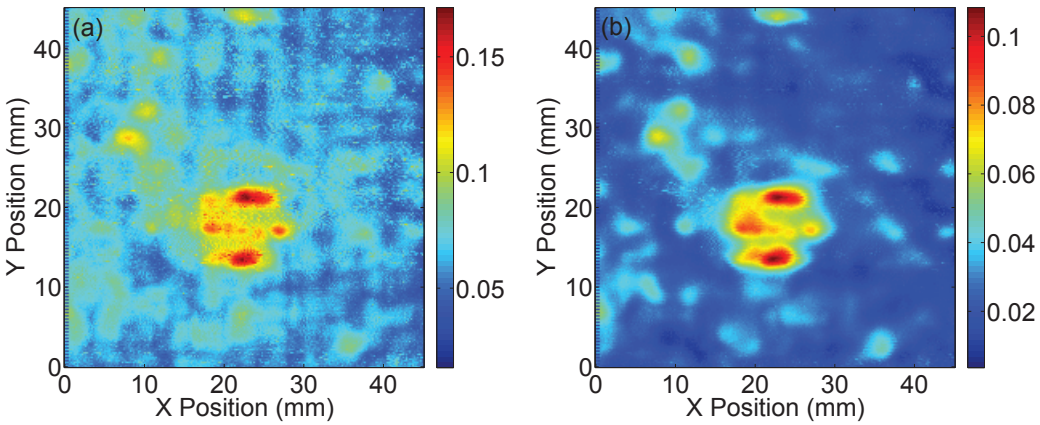

Figure 3.15: THz C-scan images based on THz waveforms (a) without and (b) with wavelet de-noising.

THz C-scans without and with wavelet de-noising are shown in Fig. 3.15. The contrast mechanism chosen here is the difference between the maximum and minimum

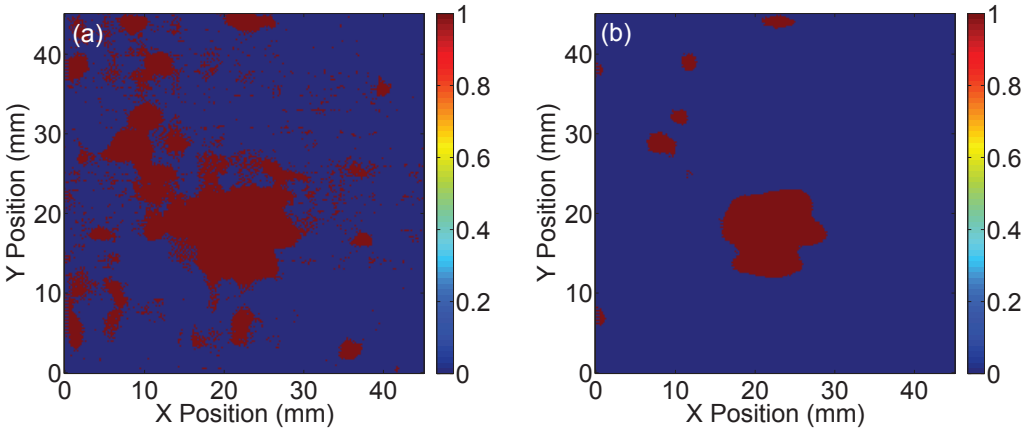

Figure 3.16: Binary THz C-scan images based on THz waveforms (a) without and (b) with wavelet de-noising.

values of the reflected THz signal within a selected time slice between 27 and 29 ps, which corresponds to the location of the delamination. THz C-scans with wavelet de-noising show higher contrast with regard to the delamination area and better enable us to differentiate the edge of the delamination from the background. This delamination is of roughly circular shape corresponding to the 12 mm diameter Upilex film disk. Due to the big size of the fiber bundles, the thin Upilex film inside is deformed and the woven fiber fabric produces the vague grid pattern in the C-scan. We can further apply the 50% rule [56] to obtain binary THz C-scans, which only consists two areas, denoting the suspected delamination area as '1', and others as '0'. This method locates the pixel with the highest value in the C-scan and assigns to it a value of 100%, then colors all pixels red that have a value of at least 50% of the maximum. Binary THz C-scans are frequently used for sizing delaminations [5]. The binary THz C-scans based on the data without and with wavelet de-noising are shown in Fig. 3.16. Despite the presence of small artifacts, the binary THz C-scan based on the processed data provides a significantly better image to locate and size the delamination.

THz B-scans without and with wavelet de-noising are shown in Fig. 3.17. Fluctuations in the original THz waveforms lead to the multiple horizontal lines in the THz B-scan in Fig. 3.17(a). These horizontal lines may be misinterpreted as internal layers

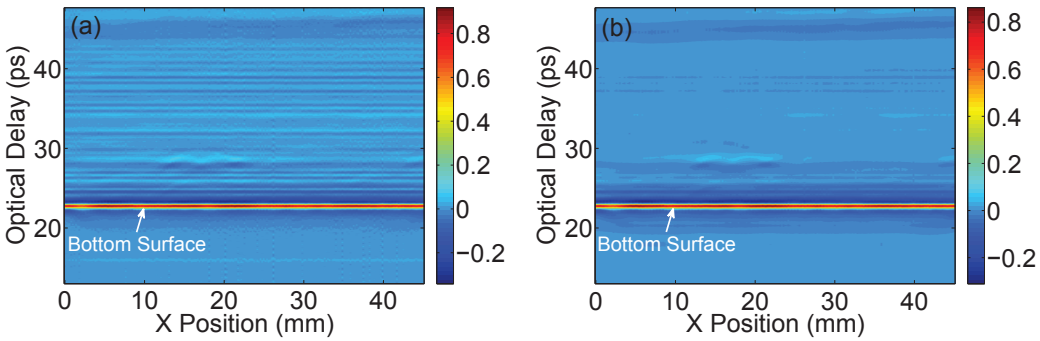

Figure 3.17: THz B-scan images based on THz waveforms (a) without and (b) with wavelet de-noising.

in the samples. By applying wavelet de-noising, the horizontal artifacts associated with water vapor are suppressed, shown in Fig. 3.17(b). Again, we apply the 50% rule to obtain binary THz B-scan images. In this case, we assign the highest value within the time slice between 27 and 29 ps as 100%, then color all pixels red that have a value of at least 50% the maximum. The binary THz B-scans based on the data without and with wavelet de-noising are shown in Fig. 3.18, which also shows that the binary THz B-scan based on processed data provides better image to locate the delamination in depth.

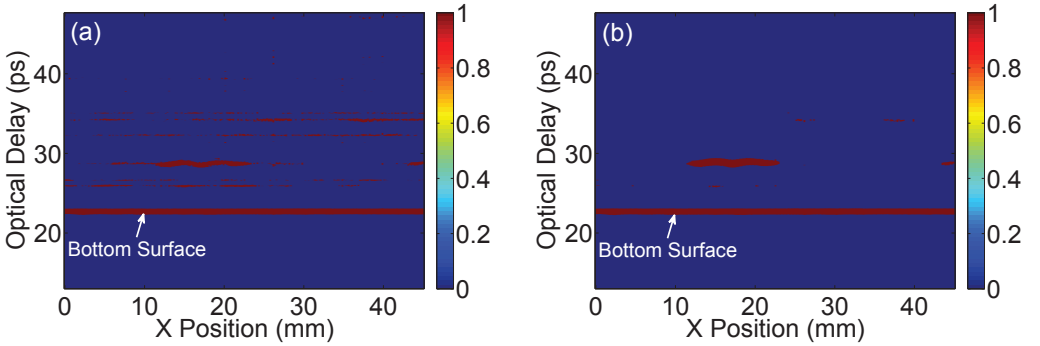

Figure 3.18: Binary THz B-scan images based on THz waveforms (a) without and (b) with wavelet de-noising.

Finally, it is important to note that this approach is of great interest in cases where undesired features associated with atmospheric water vapor of other material resonances may obscure features to be detected. In view of the difficulty and expense

in purging with dry nitrogen to physically remove the water-vapor features in many cases, the demonstrated results will be of great interest for a range of laboratory- and field-based THz NDE applications.

3.3 Polarization-resolved terahertz imaging of impact damages in hybrid fiber-reinforced composites

In this study, THz imaging is firstly applied to a hybrid fiber-reinforced composite laminate, comprised of unidirectional glass/epoxy and carbon/epoxy laminae with a cross-ply stack pattern. The evolution of intra-laminar and inter-laminar damage throughout the thickness of the laminate (1.65 mm) subject to low-velocity impact is evaluated. Inter-laminar damage at the interface and the intra-laminar damage close to the same interface can be differentiated by taking advantage of the sensitivity of the carbon-fiber orientation to the THz polarization. THz C- and B-scan images are obtained to exhibit the propagation of the damage from the top to the bottom surface in three dimensions.

3.3.1 Terahertz polarization versus carbon fiber orientation

The conductivity of carbon fibers severely limits the penetration ability of THz waves into the material. For unidirectional carbon fiber-reinforced composites, the conductivity is anisotropic and depends on the THz polarization and fiber orientation, which can be expressed as [57]

$$\sigma(\theta) = \sigma_l \cos^2\theta + \sigma_t \sin^2\theta \tag{3.12}$$

where θ is the angle between the THz polarization and fiber orientation and σ_l and σ_t are the longitudinal and transverse conductivities, respectively. Along the fiber direction, the electric current flows through the carbon fibers, so the longitudinal conductivity depends on the conductivity of carbon fibers σ_f and on the fiber volume

fraction ν_f,

$$\sigma_l \approx \sigma_f \nu_f \tag{3.13}$$

For the transverse conductivity, because the resin material is nonconductive, the flow of electric current only occurs due to random contact between adjacent carbon fibers, which depends on the manufacturing process and the quality of the composites [57]. Therefore, the longitudinal conductivity is much higher than the transverse conductivity. Based on the literature [58], longitudinal conductivity rangs from $1\times\ 10^4\ S/m$ to $6\times\ 10^4\ S/m$, and the transverse conductivity varies from 2 S/m to 600 S/m.

By analyzing the electric conductivity, one finds that (1) when the THz polarization is parallel to the orientation of carbon fibers, the electric conductivity is maximum and the THz reflectivity also reaches the maximum; (2) when the THz polarization is perpendicular to the carbon fibers, conductivity and reflectivity achieve their minimum. The ideal amplitude reflection coefficient $R_{\_ideal}$ can be expressed as

$$R_{\_ideal} \approx 1 - \sqrt{\frac{2\omega\epsilon_0}{\sigma}} \tag{3.14}$$

where ω is the THz frequency, and ϵ_0 is the permittivity of free space. The reflection coefficient approximately equals to 1 when THz polarization is parallel to the carbon-fiber orientation.

Monitoring the reflection coefficient across the surface of carbon fiber composites with THz imaging can be utilized as a method to characterize the impact damage on the surface. When carbon fiber-reinforced composites suffer from impact damage, carbon fiber distortion and fracture will occur in the damage area, which will lead to spatial variation of the reflection coefficient as well as the polarization anisotropy. The reflection coefficient in regions with and without impact damage can be more easily distinguished with polarization parallel to the carbon-fiber orientation [59].

3.3.2 Polarization-resolved terahertz imaging

The tested sample is a cross-ply hybrid fiber-reinforced composite laminate, shown in Fig. 3.19. The dimension of the laminate is 120 mm (length: x direction) $\times$ 120 mm (width: y direction) $\times$ 1.65 mm (thickness: z direction). The laminate is formed from prepregs of unidirectional E-glass fibers with epoxy resin, and prepregs of unidirectional carbon fibers with epoxy resin. For the prepreg of glass/epoxy, the fiber volume fraction is 60 vol.% and the resin content is 33 wt.%, the orientation of the glass fibers is along the direction of length (x direction); for the prepreg of carbon/epoxy, the fiber volume fraction is 60 vol.% and the resin content is about 42 wt.%, the orientation of the carbon fibers is along the direction of width (y direction). The stacking sequence of the laminate is $[0\,^{\circ G}_{2}/90\,^{\circ C}_{3}]_s$, corresponding to the thicknesses $[0.400mm/0.425mm]_s$. The electric conductivity of the carbon fiber is $5.88 \times 10^4\ S/m$ in our case. Damage was generated by controlled free-fall impact: an impactor of 50 g struck the center of the top surface of the laminate at a speed of 9.5 m/s, schematically shown in Fig. 3.20.

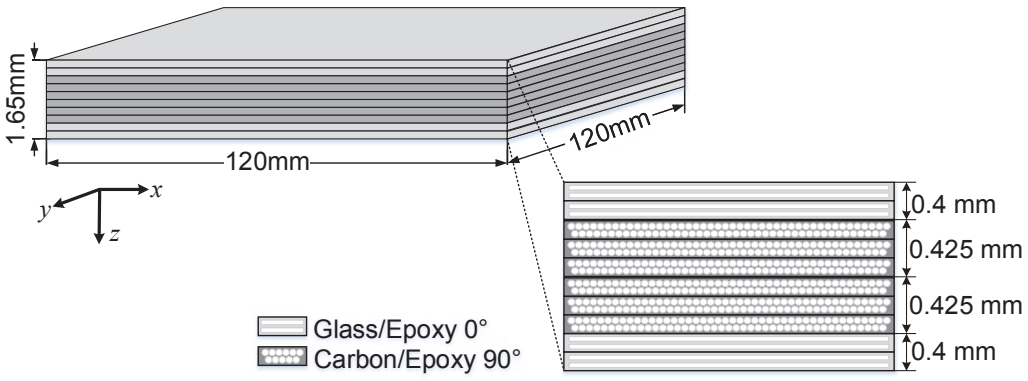

Figure 3.19: Schematic diagram of hybrid fiber-reinforced composite sample indicating dimensions and internal structure.

This damaged sample was firstly scanned with ultrasonic waves to get initial knowledge of the damage pattern and also to provide a point of comparison for the

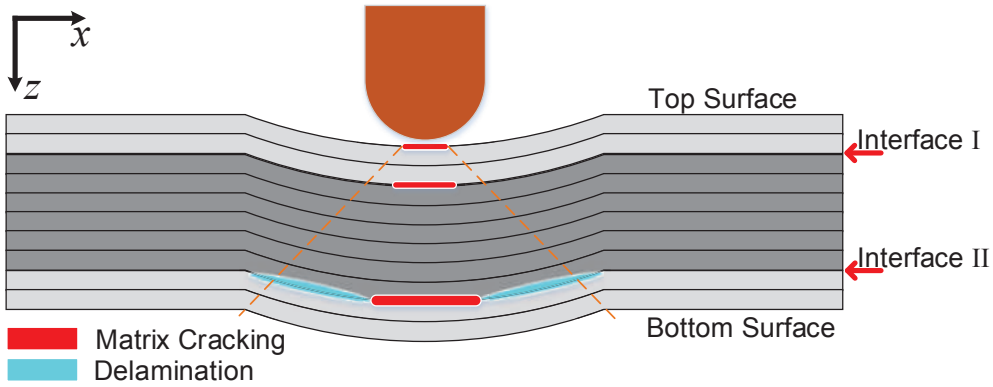

Figure 3.20: Schematic diagram (edge view) of sample subjected to low-velocity impact damage with highlighted damage types.

THz imaging results. A customer-designed ultrasonic scanner fabricated by Inspection Technology Europe BV was used for the ultrasonic C-scan experiment. The transducers chosen for this investigation are focused immersion transducers with a manufacturer-provided central frequency of 5 MHz, since this frequency provides a balance between the attenuation and resolution. Ultrasonic C-scans were performed on the sample with water coupling under both transmission (pitch-catch) mode and reflection (pulse-echo) mode over an area of 50 mm $\times$ 30 mm with a 0.2 mm scan step size. The ultrasonic C-scan in transmission, shown in Fig. 3.21(a), exhibits the accumulative damage pattern through the sample, since the surface bending, inter- and intra-laminar damages all lead to the attenuation of ultrasonic waves; the ultrasonic C-scan in reflection, shown in Fig. 3.21(b), can highlight the inter-laminar damage region, since the delamination (gap) leads to higher reflection.

However, due to the limited axial resolution, ultrasonic C-scans cannot provide information in depth to observe the morphology and evolution of the impact damage throughout the thickness of this laminate. Therefore, polarization-resolved THz imaging is performed in the following.

THz imaging is performed in reflection mode at almost normal incidence. Before imaging the sample, a THz reference signal was recorded by setting a metal plate

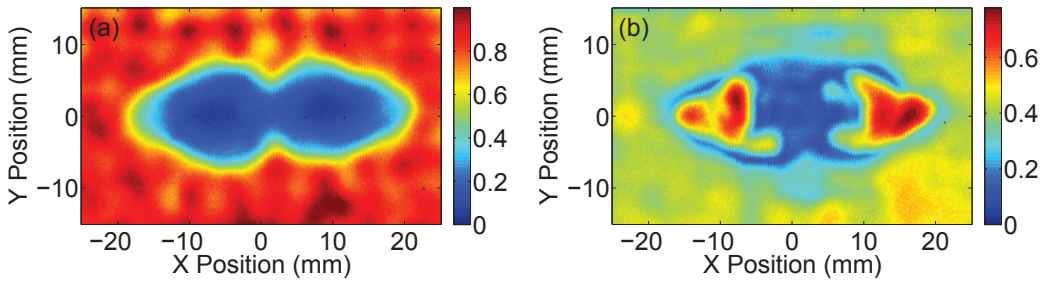

Figure 3.21: Ultrasonic C-scan results (a) in transmission and (b) in reflection modes. The ultrasonic waves are incident from the top surface of the sample. The contrast is based on the absolute value of the amplitude of the second-round signal in transmission and the second echo in reflection.

at the sample position. The time domain waveform and the spectrum of this reference signal are shown in Fig. 3.12. The THz pulse [Fig. 3.12(a)] is composed of approximately one electromagnetic cycle, and its duration is a few picoseconds. The spectrum [(Fig. 3.12(b)], obtained by Fourier transforming the temporal pulse, extends from ∼100 GHz to ∼3 THz. Pronounced atmospheric water-absorption lines can be observed [60]. The power of the THz radiation is below 1 μW so no thermal strain is induced in the sample.The sample is raster-scanned by a set of motorized stages moving in x and y directions with a 0.2 mm spatial step size over the center area (50 mm × 30 mm) of the sample plane. THz waves cannot penetrate the entire sample thickness due to the carbon fibers in the central layer. Therefore, we separately imaged the sample from both the top and bottom surfaces. In order to consider the interaction between the THz polarization and carbon-fiber orientation, the THz polarization was set first in the x direction (perpendicular to the carbon-fiber orientation). After completing the scans from both surfaces, the polarization was rotated to the y direction (parallel to the carbon-fiber orientation). In total, four sets of images were acquired in this study.

Based on the sample structure, we expect THz temporal waveforms reflected off the various interfaces in Fig. 3.22. In the case of a region without impact damage [Fig. 3.22(a)], the first echo is determined by the Fresnel reflection at the surface

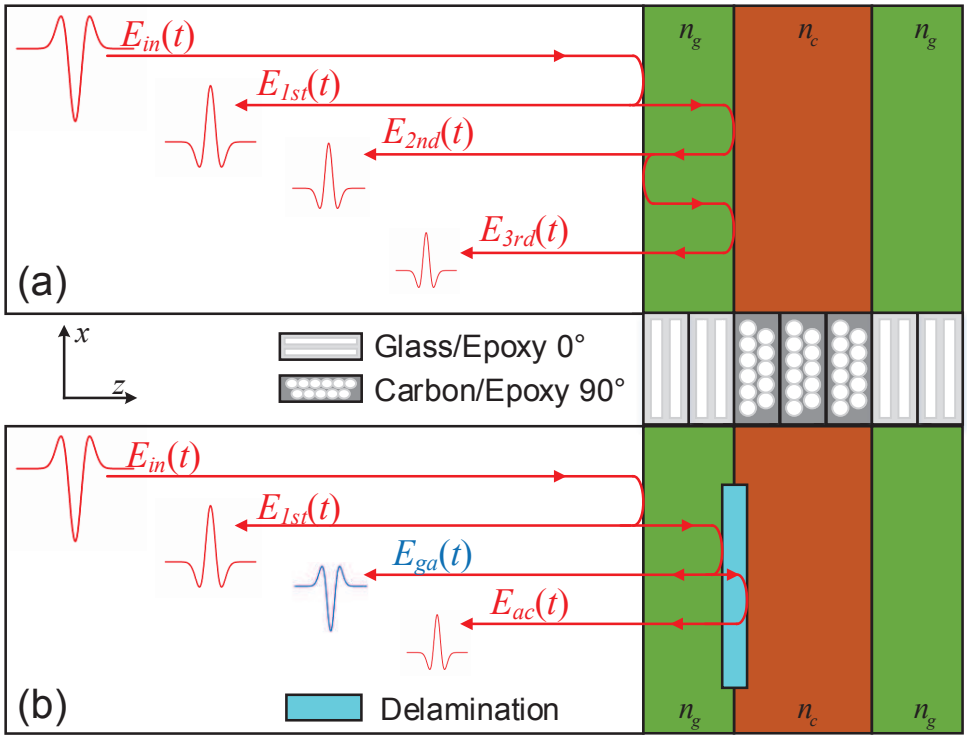

Figure 3.22: Estimated reflected THz waveforms (a) in undamaged region and (b) in region with delamination.

of the sample, and the second echo corresponds reflection at the interface between the glass/epoxy and carbon/epoxy layers with multiple reflections inside the sample following. For normal incidence on an interface between two media with refractive indices n_i and n_j , the amplitude reflection coefficients r_{ij} and transmission coefficients t_{ij} are

$$r_{ij} = \frac{n_i - n_j}{n_i + n_j} \tag{3.15}$$

$$t_{ij} = \frac{2n_i}{n_i + n_j} \tag{3.16}$$

In our study, we consider the THz reference signal shown in Fig. **??**(a) as the incident THz pulse $E_{THz}(t)$, and we also neglect the negligibe dispersion in the relevant spectral range. The reflected THz waveform is

$$E_{THz}(t) = E_{1st}(t) + E_{2nd}(t) + E_{3rd}(t) \tag{3.17}$$

with

$$E_{1st}(t) = r_{ag}E_{in}(t) \tag{3.18}$$

$$E_{2nd}(t) = t_{ag}r_{gc}t_{ga}E_{in}(t - \frac{2n_g d}{c})e^{-2\alpha d} \tag{3.19}$$

$$E_{3rd}(t) = t_{ag}r_{gc}r_{ga}r_{gc}t_{ga}E_{in}(t - \frac{4n_g d}{c})e^{-4\alpha d} \tag{3.20}$$

where c is the *in vacuo* speed of light, d is the thickness of the glass/epoxy layer, n_g is the refractive index of glass/epoxy layer, α is the absorption coefficient in the glass/epoxy layer, t_{ag} and t_{ga} are transmission coefficients from air to glass/epoxy and glass/epoxy to air, r_{gc} are r_{ga} reflection coefficients from glass/epoxy to carbon/epoxy and glass/epoxy to air, and we only consider one multiple reflection.

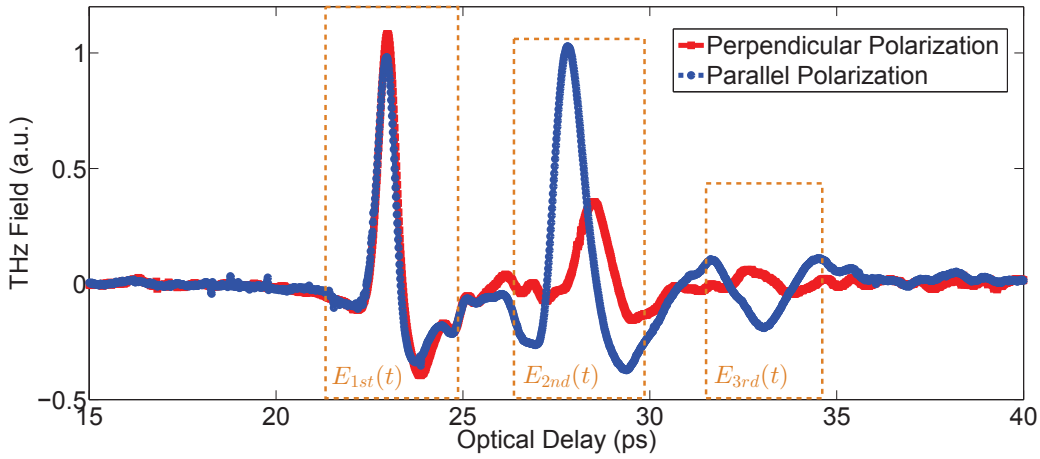

Figure 3.23: Typical time-of-flight waveforms from an undamaged region with THz polarization parallel and perpendicular to the carbon fibers.

Typical THz waveforms with polarization parallel and perpendicular to the carbon-fiber orientation from the undamaged region in experiments are shown in Fig. 3.23. The significant difference of the amplitudes of the second echoes, which reflect from the interface between the glass/epoxy and carbon/epoxy plies, illustrates the change of reflection coefficient under different polarization. In addition to the difference in amplitude, a temporal delay of the second echoes for the two polarizations is also observed, indicating that the group velocity depends on polarization in the glass/epoxy plies. The refractive index of glass/epoxy n_g can be estimated from the time delay ΔT between the first and second echoes and the thickness of the glass/epoxy layer d as

$$n_g = \frac{c\Delta T}{2d} \tag{3.21}$$

In our case, with the polarization parallel to the glass fibers, the refractive index is $n_{g,\parallel}$=2.124; with polarization perpendicular to the glass fibers, the refractive index is $n_{g,\perp}$=1.950. This polarization anisotropy underlies previously observed THz birefringence in unidirectional glass fiber-reinforced composites [61].

First, we discuss the THz images when the THz pulse is incident on the top surface of the sample. Polarization-resolved C-scans obtained from the top surface

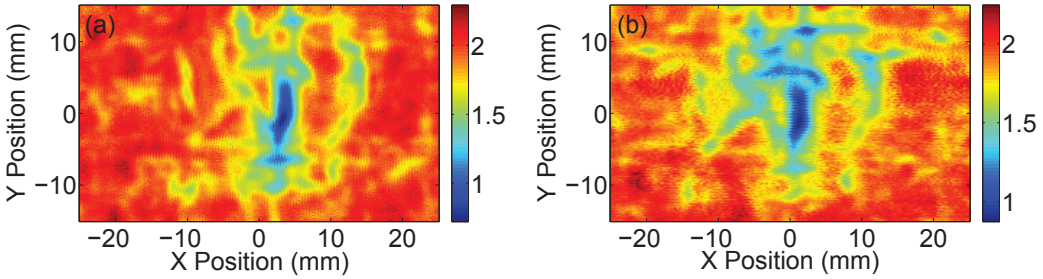

Figure 3.24: THz C-scans of the top surface with polarization perpendicular (a) and parallel (b) to the carbon-fiber orientation.

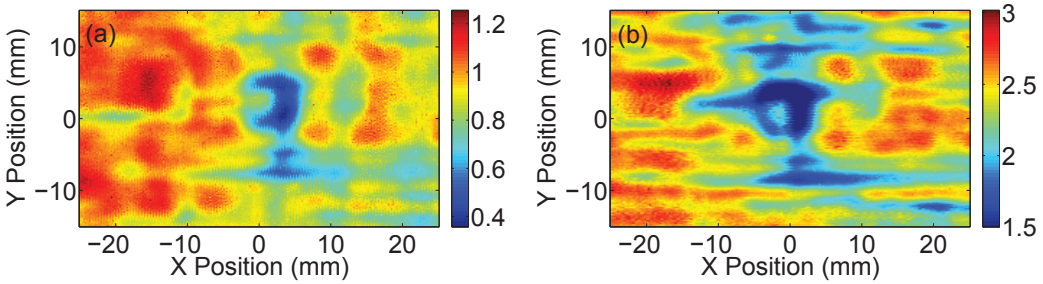

Figure 3.25: THz C-scans of the Interface I with polarization perpendicular (a) and parallel (b) to the carbon-fiber orientation.

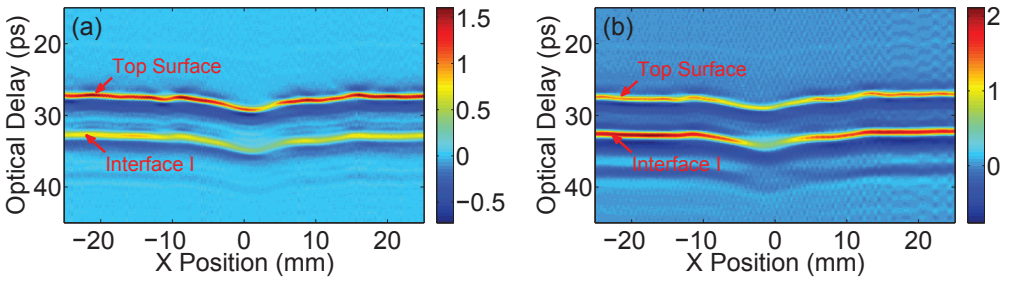

Figure 3.26: THz B-scans incident on the top surface (along section y=0) and with polarization perpendicular (a) and parallel (b) to the carbon-fiber orientation.

and interface I are shown in Fig. 3.24 and Fig. 3.25. The selected contrast mechanism for all the THz images in this study is the peak-to-valley amplitude difference of the corresponding echoes. Impact damage on the surface can be clearly seen in Fig. 3.24, and there is no significant difference between C-scans with different polarization. However, polarization dependence in the C-scans associated with interface I is pronounced due to influence of carbon fibers, as shown in Fig. 3.25. Impact-induced matrix cracking and fiber distortion/fracture in the carbon/epoxy layer lead to the decrease of the reflection coefficient at interface I for both perpendicular and parallel polarizations. By contrast, we observe parallel polarization is more sensitive to the region with fiber distortion/fracture, and leads to a further decrease of the reflected pulse amplitude compared with that for perpendicular polarization, which provides better contrast for locating the damage area in C-scan. B-scan images across the section y=0 provide depth information, as shown in Fig. 3.26. Indentation on the surface and damaged regions can also be located in THz B-scans. The combination of the THz C-scan and B-scan images exhibit the evolution of the impact-induced damage from the top surface to the first interface between glass/epoxy and carbon/epoxy in three dimensions.

Images incident on the bottom surface of the sample are now discussed in the following. Fig. 3.27 shows C-scans of the bottom surface, which evidence the protrusion on the bottom surface introduced by the propagation of the impact damage from the top surface. Again, no significant polarization dependence is observed for this glass/epoxy layer. C-scans of interface II between the carbon/epoxy and glass/epoxy layers are shown in Fig. 3.28. Unlike the previous results, the C-scans in this case show quite different damage patterns for the two polarizations. For parallel polarization, the damaged region shows lower contrast due to the existence of matrix cracking and fiber distortion/fracture, which is consistent with the previous results. However, for perpendicular polarization, the damaged region shows higher contrast. This higher

contrast indicates the existence of an air gap originating in the separation of the carbon/epoxy and glass/epoxy plies, i.e., delamination.

The THz waveforms in region of delamination can also be estimated, as shown in Fig. 3.22(b). Usually, the air gap associated with the delamination is thin; thus, the second echo $E_{2nd}(t)$ received is the superposition of the two echoes reflected from the glass/epoxy-air interface $E_{ga}(t)$ and from the air-carbon/epoxy interface $E_{ac}(t)$, which can be expressed as

$$\begin{aligned} E_{2nd}(t) &= E_{ga}(t) + E_{ac}(t) \\ &= t_{ag} r_{ga} t_{ga} E_{in}(t - \frac{2n_g d'}{c}) e^{-2\alpha d'} \\ &+ t_{ag}^2 r_{ac} t_{ga}^2 E_{in}(t - \frac{2n_g d'}{c} - \frac{2d_{gap}}{c}) e^{-2\alpha d'} \end{aligned} \tag{3.22}$$

where d' is the thickness of the glass/epoxy layer with deformation due to the impact damage, d_{gap} is the thickness of the air gap, and the absorption in the narrow air gap is neglected. Because of the opposite sign of the reflection coefficient r_{ga} at the interface between glass/epoxy and air gap, the THz pulse will be inverted at this interface.

The change in the peak-to-valley difference of the second echo in the damaged region depends mainly on two factors: (1) the thickness of the air gap d_{gap} (a narrower air gap leads to a smaller difference in the peak-to-valley differences due to partial cancellation of the negative and positive peaks) and (2) the reflection coefficient r_{ga} (impact-induced matrix cracking and fiber distortion/fracture in the carbon/epoxy will lower the value of the reflection coefficient, which will further decrease the peak-to-valley difference). Therefore, for C-scans with perpendicular polarization, the thickness of the delamination dominates the change of the contrast, and the C-scans reveal the delamination area at the interface. For C-scans with parallel polarization, the reflection coefficient at the interface dominates the change of

the contrast. Thus, the C-scan in this case evidences the matrix cracking and fiber distortion in the carbon/epoxy layer.

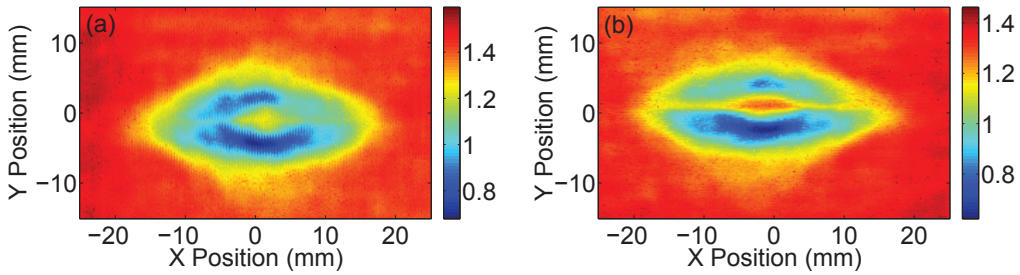

Figure 3.27: THz C-scans of the bottom surface with polarization perpendicular (a) and parallel (b) to the carbon fiber orientation.

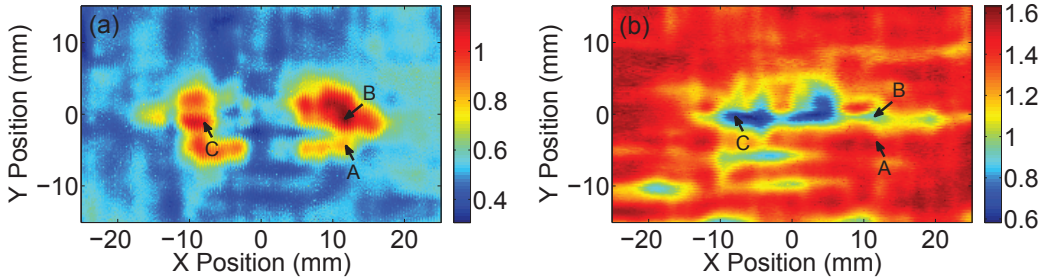

Figure 3.28: THz C-scans of the Interface II with polarization perpendicular (a) and parallel (b) to the carbon fiber orientation.

We implemented a numerical parameter fitting method based on multiple regression analysis [15] to estimate the delamination thickness and the reflection coefficient at the interface between the air gap and carbon/epoxy layer. The measured second echo is considered as the objective function, and a model function E_{model} is defined based on the equation (3.22) to stimulate the objective function as

$$E_{model} = a_1 E_{in}(t - t_1) + a_2 E_{in}(t - t_1 - \Delta t) \tag{3.23}$$

where a_1, a_2, t_1 and Δt are the regression parameters. Initial values should be carefully set so that the regression analysis can converge to a characteristic global minimum. Then multiple regression analysis with least-squares minimization is performed to es-

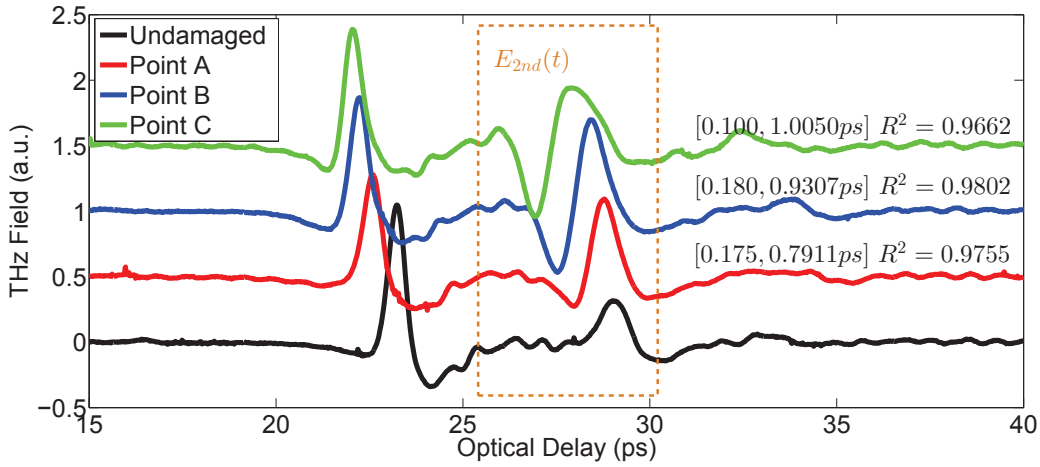

Figure 3.29: Temporal waveforms for perpendicular THz polarization at selected positions on sample (see Fig. 11).

timate the regression parameters. In our case, our desired parameters are a_2 and Δt, which contain the information about the delamination thickness and the reflection coefficient between the air gap and the carbon/epoxy layer. Fig. 3.29 shows the temporal waveforms with perpendicular THz polarization at selected points (shown in Fig. 3.28) and the estimated parameters $[a_2, \Delta t]$ obtained by the multiple regression analysis. The coefficient of determination R^2 is also used here to provide information about the goodness of fit of the regression model function. The corresponding delamination thicknesses are 118.67 μm, 139.61 μm and 150.08 μm for Points A to C respectively. Although d_{gap} is largest at Point C, the signal here does not exhibit the highest contrast in Fig. 3.28(a). The reason is that a_2 is smaller at Point C compared with at Point B, indicating matrix cracking and fiber distortion is more severe at Point C, which is also observed in Fig. 3.28(b).

B-scans obtained incident from the bottom surface are shown in Fig. 3.30. Typical damage features can be observed in depth, including surface bending, inter- and intra-laminar damages. Therefore, the total set of C- and B-scans exhibits the evolution of the impact-induced damage from the top to the bottom surface in three dimensions, which fits quite well with theoretical simulation results in Ref. [62, 63]. The size of the

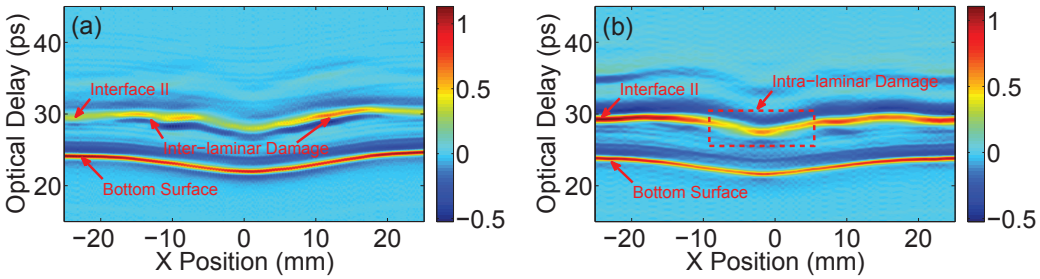

Figure 3.30: B-scans incident from the bottom surface (along section y=0) and with polarization perpendicular (a) and parallel (b) to the carbon-fiber orientation.

delamination area can be calculated by applying the '50% rule' to the THz C-scan, and the thickness of the delamination can also be obtained with the parameter fitting method based on multiple regression analysis. Therefore, the delamination can be characterized quantitatively in three dimensions.

In this section, THz C-scans exhibit the great capability of evaluating the morphology of the damage at various interfaces, which provide a clear representation of the propagation of the damage throughout the thickness. Moreover, depth information is obtained from THz B-scans, together with a parameter fitting method based on multiple regression analysis, enabling us to characterize the delamination quantitatively. The effect of THz polarization in distinguishing features around the interface, where both intra- and inter-laminar damages exist, is investigated. Inter-laminar damage at the interface and the intra-laminar damage close to the same interface, which most NDE techniques are ill-suited to resolve, are successfully differentiated by exploiting the sensitivity of the carbon-fiber orientation to the THz polarization.

CHAPTER 4
TERAHERTZ DECONVOLUTION FOR STRATIGRAPHIC CHARACTERIZATION OF MULTILAYERED STRUCTURES

Due to the penetrative capability of THz radiation, THz imaging has attracted considerable interest as a noninvasive, noncontact, and nonionizing modality to characterize various non-metallic multi-layered structures in industrial, biomedical, and cultural-heritage fields. THz reflective imaging provides information in depth by analyzing the reflected THz signal with an incident approximately single-cycle THz pulse. Due to dielectric discontinuities with depth, reflected temporal THz echoes associated with the Fresnel coefficients between various interfaces are recorded as a function of transverse position in amplitude and time delay. The successful characterization of multilayered structures relies on the precise extraction of echo parameters from the reflected THz signal. For example, characterization of the stratigraphic properties is based on the estimation of arrival times of echoes. In practice, the echoes may partially or totally overlap; therefore, when no prior knowledge of the structures is available, THz deconvolution is usually required in order to precisely resolve the overlapping echoes and extract the arrival times of superimposed echoes from noisy measurement.

THz deconvolution is essentially an effective technique to increase the depth-resolution of THz imaging by retrieving the impulse response function of the testing sample. However, the deconvolution technique in the THz regime is not mature, and only limited effort has been made to enhance the depth-resolution, which limits the ability of THz imaging in resolving optically thin layers in the THz regime.

In this chapter, advanced THz deconvolution techniques are developed to enhance the capability THz imaging for the stratigraphic characterization of multilay-

ered structures with optically thin layers in the THz regime. Conventional deconvolution technique based on inverse filtering is introduced in the first section. THz frequency-wavelet domain deconvolution (FWDD), which is based on the inverse filtering, is specifically designed to enhance the deconvolution process by first employing frequency-domain filtering and then further improving the signal-to-noise ratio (SNR) by wavelet de-noising. The depth-resolution achieved is about 55 μm. A case study for the characterization of various failure modes in polymer-coated with FWDD is presented to show the effectiveness of FWDD in resolving polymer coatings with thicknesses about 50 μm.

In the second section, THz sparse deconvolution based on an iterative shrinkage algorithm is developed. With an up-sampling approach, sparse deconvolution with super-resolution is also developed to overcome the time resolution limited by the sampling period in the measurement and increase the precision of the estimation of echo arrival times. A simple but effective time-domain model for describing the temporal pulse spreading due to the frequency-dependent loss is also designed and introduced into the algorithm, which significantly improves the performance of sparse deconvolution in processing time-varying pulses during the propagation of THz waves in materials. Numerical simulations and experimental measurements verify the algorithms and show that sparse deconvolution can be considered as an effective tool for THz nondestructive characterization of multilayered structures. The depth-resolution achieved by sparse deconvolution is about 45 μm.

In the third section, a novel method for enhancing the depth-resolution of THz deconvolution based on autoregressive spectral extrapolation is developed. An autoregressive process is modeled based on the THz frequency components with high SNR, and the missing frequency components in the low SNR regions are extrapolated based on the autoregressive model. In this way, the entire THz frequency spectrum of the impulse response function, corresponding to the material structure, is recovered.

This method, which is verified numerically and experimentally, is able to provide a 'quasi-ideal' impulse response function, and therefore, significantly enhances the depth-resolution for resolving optically thin layers in the THz regime. The depth-resolution achieved with this method is about 27 μm.

4.1 Terahertz Deconvolution Based on Inverse Filtering

For samples with layered structure, time-domain THz imaging can provide information in depth by analyzing the reflected THz signals with an incident approximately single-cycle THz pulse. Due to dielectric variations with depth, reflected temporal THz echoes associated with the Fresnel coefficients between various layers are recorded as a function of transverse position in amplitude and time delay. The echo amplitudes provide information on the various refractive indices, while the time delays between THz echoes provide the optical thickness of successive layers. With a knowledge of the refractive indices of the corresponding materials, the physical layer thickness can be extracted. When the layer thickness is optically thin, THz echoes will partially or totally overlap; therefore, the amplitude and time delay cannot be directly extracted from the time-domain waveform. In this case, THz deconvolution can be utilized to resolve the overlapping echoes and reconstruct the intrinsic impulse-response function, and hence the physical structure of the sample studied.

In the time domain, the THz reflected signal (electric field) $r(t)$ is the convolution of the incident THz pulse $i(t)$ with the impulse-response function $h(t)$, which corresponds to the structure and properties of the sample at a given two-dimensional position,

$$r(t) = i(t) \otimes h(t). \tag{4.1}$$

Deconvolution retrieves the impulse response function $h(t)$ by applying the inverse

Fourier transform based on the convolution theorem,

$$h(t) = FFT^{-1}\left[\frac{FFT\big(r(t)\big)}{FFT\big(i(t)\big)}\right], \tag{4.2}$$

where FFT denotes the Fourier transform and FFT^{-1} the inverse Fourier transform.

4.1.1 Terahertz frequency-wavelet domain deconvolution (FWDD)

Frequently, successful deconvolution cannot be expected by directly applying Eq. (4.2), since division by small numbers will give rise to large spikes in the reconstructed impulse-response function, especially in the high frequency region, leading to severe ringing in the time domain. Therefore, deconvolution process is usually further augmented by frequency-domain filtering to suppress the high-frequency noise, which can be expressed as,

$$h'(t) = FFT^{-1}\left[FFT\big(f(t)\big)\times\frac{FFT\big(r(t)\big)}{FFT\big(i(t)\big)}\right], \tag{4.3}$$

with $f(t)$ the filter function in the time domain. In order to obtain a successful reconstruction, the temporal duration of $f(t)$ should be short enough to resolve the time intervals between featured echoes, and $f(t)$ should not contain extra signal cycles before or after the main peak, which will obscure the real featured echoes in the reconstructed signal; however, the selection of $f(t)$ is also a compromise between time resolution and frequency-domain filtering [64]. If the duration of $f(t)$ is too short, its frequency spectrum will include large spikes at high frequencies, which will degrade the reconstructed signal in the time domain.

A double Gaussian filter or Wiener filtering can be selected to serve as the frequency-domain filtering [54], and a tapered cosine apodisation function has also been found to work well [65]. Considering the complexity and effectiveness, a Hanning window function is chosen as the filter function $f(t)$ in this study, and its frequency

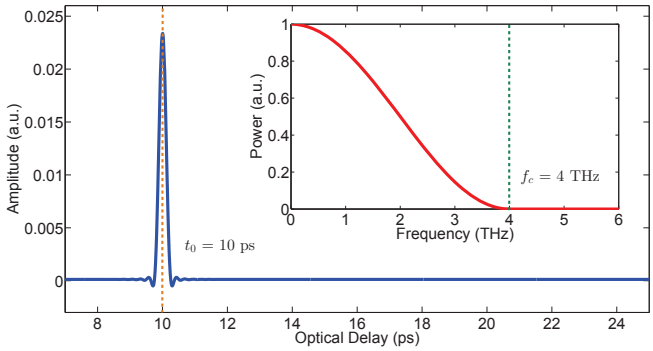

Figure 4.1: Hanning window function with typical values, t_0=10 ps and f_c=4 THz, in the time domain and its Fourier transform (power spectrum) in the inset.

spectrum $F(\omega)$ can be expressed as

$$F(\omega) = \begin{cases} e^{i\omega t_0}\cos^2(\frac{\omega}{4f_c}) & \mid \omega \mid \leq 2\pi f_c, \\ 0 & \mid \omega \mid > 2\pi f_c, \end{cases} \tag{4.4}$$

where t_o corresponds to the arrival time of the main peak in the time domain and f_c is the cutoff frequency. This frequency-domain filtering is easy to manipulate just by changing the cutoff frequency f_c. An example of $f(t)$ and its frequency spectrum $F(\omega)$ for typical parameters ($t_0 = 10$ ps and $f_c = 4$ THz) is shown in Fig. 4.1.

Quite often, deconvolution only with frequency-domain filtering cannot guarantee a satisfactory signal-to-noise ratio when a relatively high value of f_c is selected. Stationary wavelet shrinkage is applied to further attenuate the residual noise. This technique decomposes a 1D signal into the approximation coefficients vector and detail coefficients by convolving with a low-pass filter and a high-pass filter along the temporal axis at each level. Wavelet coefficients with small absolute values can be considered as noise, and wavelet coefficients with large absolute values are regarded as the main featured information of the signal [54][66]. Removing the small absolute-value coefficients by thresholding and then reconstructing the signal is expected to produce a signal in which the contribution of noise has been reduced. Sometimes, the

signal after frequency-wavelet deconvolution contains slow fluctuations corresponding to the low frequency noise due to the THz source being deficient in the low THz frequency region. This kind of low-frequency noise can be canceled by subtracting the baseline of the deconvolved signal.

4.1.2 Characterization of failure modes in polymer-coated steel with FWDD

In this subsection, a case study about the implementation of FWDD for real industrial application is presented. THz reflective imaging is applied to characterize the failure modes in a polymer coating on a steel plate, and FWDD is implemented to resolve the temporally overlapping echoes in order to quantitatively characterized of different failure modes, *viz.* corrosion, delamination, and blistering. THz images in three dimensions clearly exhibit the coating thickness distribution across the entire damaged coating, highlighting the THz features associated with different failure modes, thus demonstrating that THz imaging can be considered as an effective modality for characterizing damage mechanisms in polymer coatings on metals.

In this study, THz imaging is performed in reflection at almost normal incidence. Before imaging the sample, a THz reference signal, shown in Fig.4.12, was recorded by setting a bare metal plate (i.e., an excellent THz reflector) at the sample position. The tested sample, shown in Fig. 4.2(a), is a one-layered polymer (polyester) coating on a zinc-coated steel substrate. Prior to the application of the polymer coating, a thin ($\sim$5 μm) proprietary primer coating was applied. Both the primer and polymer were roll coated onto the substrate. The coating was initially scratched through the coating in the center, and after a multi-month accelerated-corrosion exposure, various types of failure, including corrosion, delamination, and blistering, are visually evident in the coating. Optical microscopy was employed to estimate the thickness of the coating, shown in Fig. 4.2(b). (The primer coating was not evident in the optical micrographs.) The thickness of the coating is about 0.05 mm based on observation

from the edge of the sample. We then proceeded with the THz imaging. This sample was raster-scanned by a set of motorized stages moving in x and y directions in 0.2 mm steps over a 33 mm $\times$ 55 mm region of the sample plane, corresponding to 165 $\times$ 275 pixels. Each recorded reflected temporal THz waveform contains 4096 data points, and the signal is averaged over 10 shots per pixel. After completing the scanning, a 3D volume raw data set was acquired.

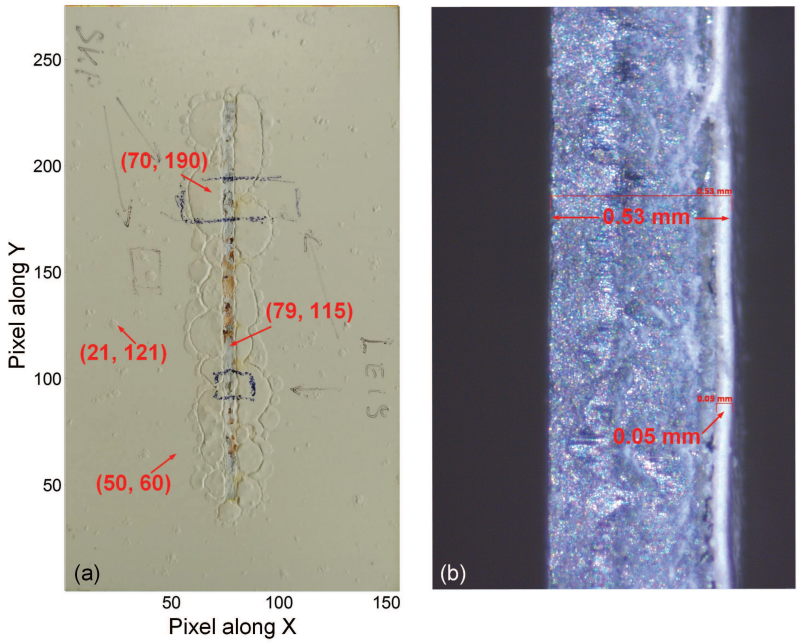

Figure 4.2: (a) Visible photograph of the surface of the coating sample with four typical positions highlighted to represent different failure modes. This photograph is also labeled with the pixel number which is the same as the THz C-scans in the following section. (b) Optical micrograph from the edge of the coated sample to roughly estimate the thicknesses of the coating and the steel plate.

Based on the observation of the coating surface features, four typical positions, which exemplify different failure modes, are selected in Fig.4.2(a). The received THz signal at position (50, 60), where no evidently visible damages exist, is shown in Fig.4.3(a1). Overlapping THz echoes at this pixel are observed due to the optically thin coating. In order to resolve the overlapping echoes and reveal the structure, THz frequency-wavelet domain deconvolution introduced previously is applied to the raw reflected THz signal at each pixel. In order to make the time resolution as high as

possible, the cutoff frequency f_c chosen for all the waveforms is 4 THz. In the wavelet denoising procedure, the *symlet* (sym4) wavelets are selected with a maximum level of 7 for the wavelet decomposition, as no significant improvement can be achieved for higher levels to justify the extra computational expense. After deconvolution, a 3D deconvolved data set is obtained. Peak detection is performed on the deconvolved signals for identifying the existence of an echo. A threshold value for peak detection is set for all pixels, above which we consider a feature as a valid peak.

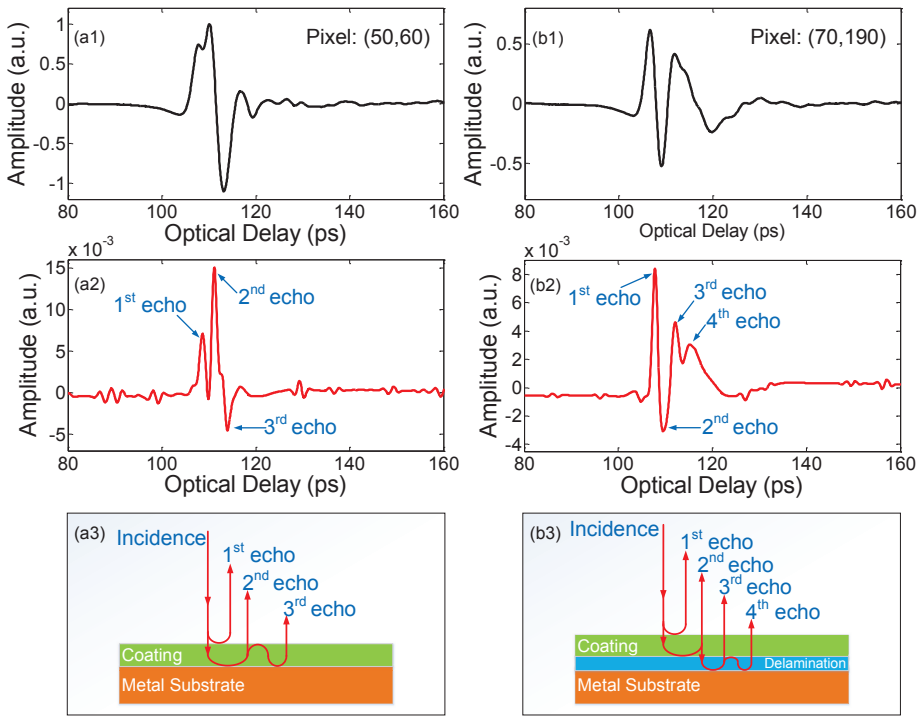

Figure 4.3: The THz raw signals [(a1) and (b1)] and deconvolved signals [(a2) and (b2)] at positions (50, 60) and (70, 190), with the corresponding representations of round-trip echoes in [(a3) and (b3)].

The deconvolved THz signal at position (50, 60) is shown in Fig.4.3(a2). Two positive peaks and one negative peak are clearly identified, which are illustrated in Fig. 4.3(a3). The first two positive peaks correspond to the echoes from the air/coating interface and the coating/substrate interface respectively. The third peak, corresponding to the second round echo, is negative due to the phase shift at the

coating/air interface. We consider pixels with this kind of deconvolved signal as normal *i.e.*, undamaged, since no features related with damages can be identified. The optical thickness of the coating can be acquired by calculating the optical delay between the first and the second peaks, which is ∼0.5 ps. The refractive index of polyester in the THz range is ∼1.7 [67], therefore, the physical thickness of the coating is ∼44 μm, which is close to the value we estimated with the optical micrograph in Fig.4.2(b).

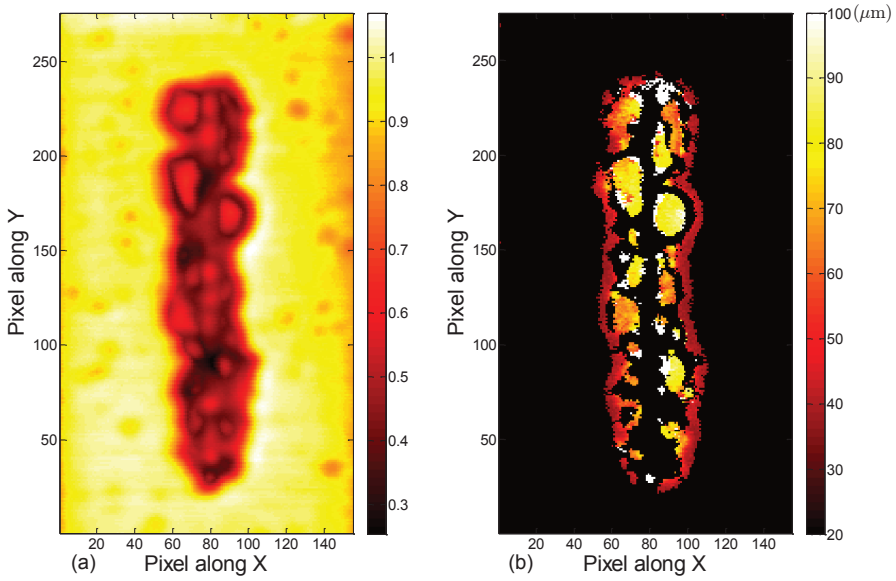

Figure 4.4: (a) THz C-scan based on the raw signals with the contrast mechanism as the maximum amplitude of the received signal, which is similar to the optical photograph in Fig. 4.2(a); (b) THz C-scan based on the deconvolved signals associated with the delamination, which indicates the regions with delamination and the physical thicknesses of the delamination across the coating plane.

The THz raw signal and deconvolved signal at position (70, 190) are shown in Fig.4.3(b1) and (b2). Compared with the normal THz deconvolved signal in Fig.4.3(a2), three positive peaks and one negative peak are identified. In this case, the second peak is negative, which indicates the separation between the coating and the substrate, corresponding to the existence of delamination (air gap). The round trip of the identified echoes are illustrated in Fig.4.3(b3). Compared with the raw

THz signal at this pixel, the deconvolved THz signal clearly reveals the prominent feature associated with the delamination, which is the most important type of adhesive failure. Moreover, the severity of delamination can be evaluated by calculating its physical thickness. With the knowledge of refractive index of air and the measurement of the optical delay between the first peak (positive) and the second peak (negative), the delamination can be characterized quantitatively.

THz C-scans can be plotted to provide a two dimensional presentation of data as a top or planar view of features in the coating system. The THz C-scan based on the THz raw data with contrast mechanism as the maximum amplitude value is firstly plotted in Fig.4.4(a), which is similar to the optical photograph in Fig.4.2(a). Based on the expected features in the deconvolved signal associated with delamination, we can extract all the pixels with this feature present and calculate the physical thickness of the delamination as a function of position. The THz C-scan in Fig.4.4(b) clearly exhibits the delamination areas where the existence of air gap is indicated by the THz deconvolved signals. We also obtain the physical thickness of the delamination across the coating plane, which demonstrates that the delamination has been successfully characterized in three dimensions quantitatively by THz imaging.

The THz raw signal and deconvolved signal at position (79, 115), where the scratch was initially located and the metal oxide first developed upon aging, are shown in Fig.4.5(a1) and (a2). The amplitude of the raw and deconvolved signals are relatively small because of the diffuse reflection at the rough surface of the corrosion area. In addition, compared with the signals at the undamaged area, a larger time delay between the first and the second echoes can be observed both in the raw and deconvolved signals. The optical delay in this case corresponds to the thickness of the grown metal oxide due to corrosion at the scratch area.

Next, we discuss the signal features at the blisters. The THz raw signal and deconvolved signal at position (21, 121), where a blister is clearly observed, are shown

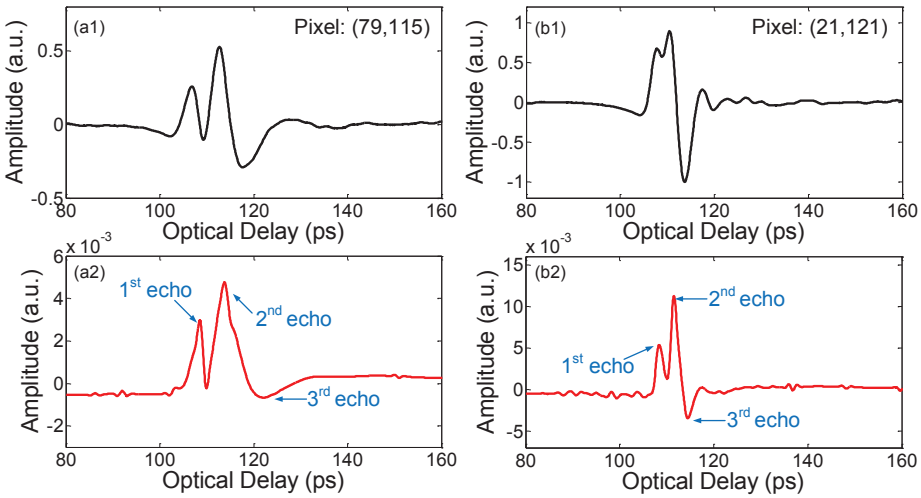

Figure 4.5: THz raw signals [(a1) and (b1)] with the corresponding deconvolved signals [(a2) and (b2)] at positions (79, 115) and (21, 121) where a blister is visually present.

in Fig.4.5(b1) and (b2). Both THz raw and deconvolved signals present quite similar features compared with the signals at the undamaged area. However, by careful comparison with the THz deconvolved signal at the undamaged area in Fig.4.3(a2), we observe: (1) the optical delay between the first and the second echoes is larger in blisters; (2) the amplitude of the second echo is smaller in blisters. Based on these two features, THz C-scans are plotted in Fig.4.6 to reveal all the blisters in the coating. In Fig.4.6(a), THz C-scan is plotted based on the optical delay between the first two positive peaks of the deconvolved signals, which represents the optical distance between the coating surface and the top surface of the metal substrate. The blistering areas, represented as red spots in the image, are clearly revealed. Compared with the undamaged areas, the blisters are associated with a slightly larger optical thickness, and the delamination and corrosion areas around the scratch exhibit much larger optical distance due to the existence of the air gap under the delaminated coating or the metal oxide, respectively. In Fig.4.6(b), THz C-scan is plotted based on the amplitude of the second positive peak, which indicates the condition of adhesion, because the second peak corresponds to the echo bouncing back after reflecting off the

substrate. Compared with the undamaged areas, the blisters show smaller amplitude which indicates a weaker adhesion with the substrate, with the delamination areas exhibit much weaker adhesion, *viz.* adhesion failure.

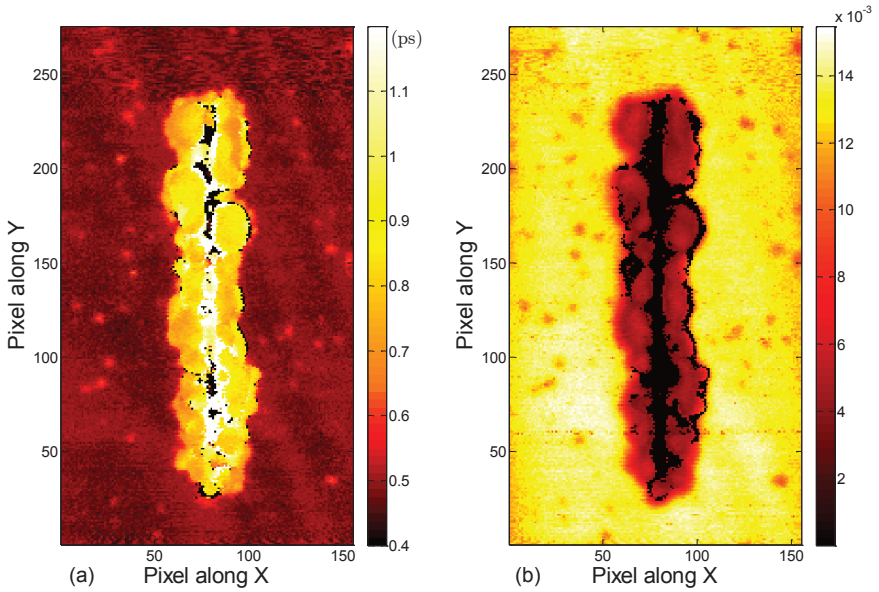

Figure 4.6: (a) THz C-scan based on the optical delay between the first positive peak and second positive peak in the deconvolved signals, which represents the optical distance between the coating surface and the top surface of the metal substrate; (b) THz C-scan based on the amplitude of the second positive peak in the deconvolved signals, which indicates the adhesive condition.

The physical origin of the contrast between blisters and the surrounding undamaged regions are now discussed. Compared with the undamaged area, the relatively large optical delay between the first two positive peaks at the locations of the blisters is due to the separation between the coating and the substrate and the existence of the air gap. However, the air gap under the blisters is too small to be resolved even in the deconvolved signals. In this case, the negative peak corresponding to the echo from the coating/air interface and the positive peak corresponding to the echo from the air/substrate are not well-separated and largely cancel with each other. The result of this overlap and cancellation is only one observable positive peak with a later arrival time and smaller amplitude compared with the peak corresponding to the echo from

the coating/substrate interface in undamaged areas [68][47]. Another reason, which is also responsible for the smaller amplitude of the second positive peak, is the presence of oxidization of the metal substrate in blisters locations induced by the accelerated aging. The oxidized substrate under the blisters provides a smaller reflection compared with the normal steel under the undamaged coating, where the coating and the substrate adhere tightly and an almost total reflection can be expected.

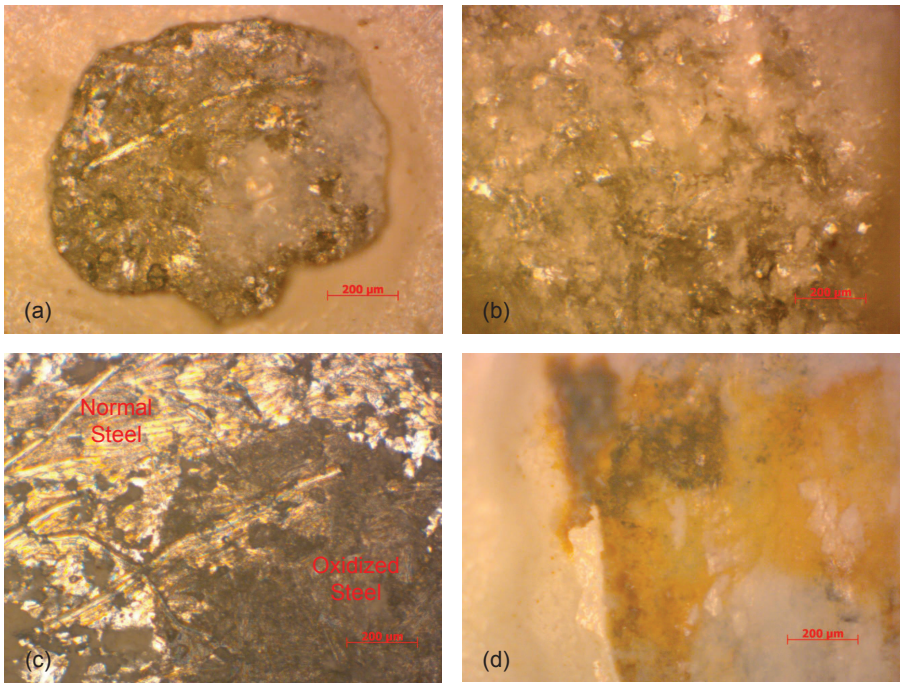

Figure 4.7: Optical micrographs associated with different failure modes after peeling off the coating. (a) Oxidized substrate in the blistering area; (b) Oxidized substrate in the delamination area; (c) Comparison between the steel substrate at the undamaged area and the blistering area by peeling off the coating at one blister area and the adjacent undamaged area; (d) Grown metal oxide due to corrosion along the scratch.

Optical microscopy was next employed to verify the physical explanations above. In order to observe the conditions of adhesion associated with different failure modes, the coating at representative positions is carefully removed. Compared with the undamaged areas, the coating at delamination and blistering areas is easier to peel off due to the existence of an air gap. Optical micrographs in areas with blistering, delamination and corrosion along the scratech are shown in Fig.4.7(a), (b), (d), re-

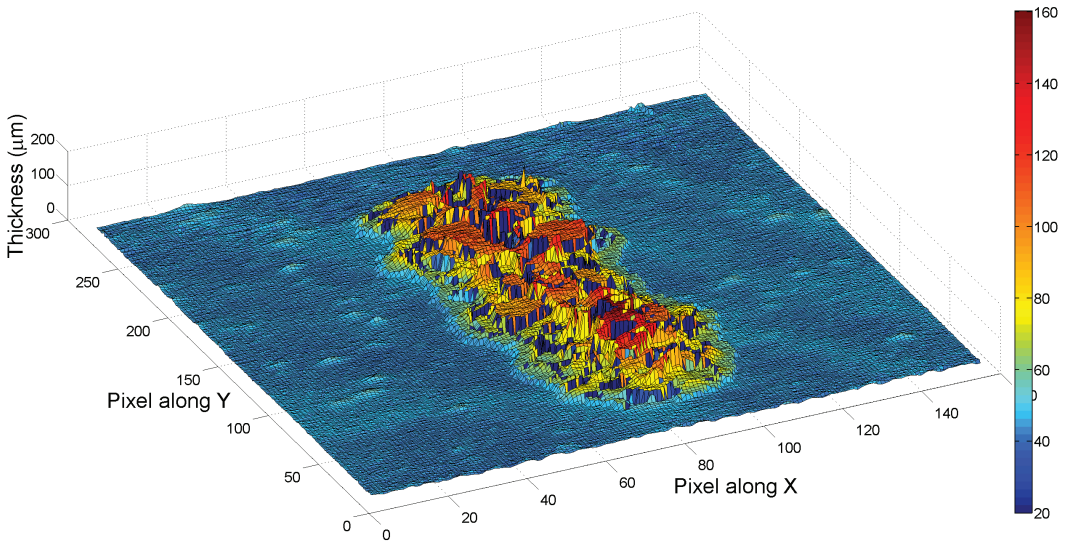

Figure 4.8: THz image of the thickness distribution, as well as the surface topology, of the coating. Different failure modes, including corrosion, delamination, and blistering, have been characterized quantitatively in three dimensions.

spectively. Oxidized substrate is observed under both the blister and delamination. Comparison between the substrate in the undamaged area and under the blister is shown in Fig. 4.7(c) by peeling off the coating at one blister and the adjacent undamaged area. The substrate in the undamaged area is visually shiny; on the contrary, the oxidized substrate under the blister appears black in the optical micrograph. The optical micrographs support our conclusions above based on the THz images concerning the compromised adhesion of the coating in these areas.

Based on the analysis above, the characteristics of various failure modes, including corrosion, delamination, and blistering, have been successfully revealed using time-domain THz reflective imaging. The thickness distribution of this damaged coating can be estimated, as shown in Fig.4.8. To do this, we assume that the refractive indices of the corrosion (metal oxide) is similar to that of the coating [69]. We note in the image the metal oxide is grown in the scratch area, on both sides of which are raised areas of delaminations. Beyond this is a relatively flat area with isolated raised areas due to blisters. With this 3D image, the thicknesses associated with

various failure modes, as well as the surface topology of the coating system are clearly reconstructed, exhibiting the capability of THz imaging for the quantitative NDE of polymer coatings on metals.

In this study, THz reflective imaging was demonstrated to characterize different failure modes in a polyester-coated zinc-coated steel plate. THz frequency-wavelet domain deconvolution was adapted to resolve the optically thin coating. Based on the deconvolved signals, the characteristics of various failure modes, including corrosion, delamination, and blistering, have been successfully identified. The THz deconvolved signals also enable us to evaluate the condition of adhesion, especially for the delamination and blisters, which are related with adhesion failure. The thickness distribution across the entire damaged coating, as well as its surface topology is also obtained. These interpretations were supported by optical microscopy. Based on these results, we conclude that THz imaging, which can provide a noninvasive, noncontact, and nonionizing modality for characterizing coatings quantitatively in three dimensions, can be utilized as an effective tool for investigating the damage mechanisms and monitoring the corrosion process in polymer-coated metals.

4.2 Terahertz Sparse Deconvolution

The reflected signals from multi-layered structures are a class of very special signals comprised of a limited number of echoes, and the corresponding impulse response functions have a *sparse* representation, which means only a limited number of data points have non-zero values. This feature enables us to exploit the sparse constraint and retrieve the impulse response function by sparse deconvolution. Compared with conventional deconvolution, sparse deconvolution is a pure time-domain method, therefore, there is no introduction of the high- and low-frequency noises mentioned above, and it can be expected to achieve a more clear representation of the material structures with super-resolution. For one-dimensional NDE problems,

super-resolution techniques seek to recover a high-resolution signal sequence from one or a set of low-resolution acquisition systems. However, sparse deconvolution has not been studied in detail nor has it been extensively used to process THz NDE signals, and to our knowledge, only one attempt has been reported so far. In [70], sparse deconvolution is briefly introduced and used to process THz signals reflected from a human palm.

In this section, the principle of sparse deconvolution and a computationally efficient iterative shrinkage algorithm for sparse deconvolution are demonstrated to process THz signals reflected from multi-layered structures. In order to increase the time-resolution, which is limited by the data sampling period, a super-resolution model for sparse deconvolution is developed by an up-sampling approach. Based on the assumption that the THz echoes are the time-shifted, amplitude-scaled replicas of the THz reference signal, both FWDD and sparse deconvolution are mainly limited to deconvolve reflected THz signals with time-invariant pulses. However, in practice, the temporal pulse spreading caused by frequency-dependent attenuation and dispersion during the propagation of THz waves in materials does occur and, therefore, lowers the performance of deconvolution. In order to solve this problem, a simple but effective time-domain model for describing the pulse spreading is designed and introduced into the algorithm for sparse deconvolution to enhance its ability to deconvolve *time-varying* echoes. Both numerical simulations and experimental measurements are performed to prove the effectiveness of sparse deconvolution, and the results are also compared with those obtained by FWDD.

4.2.1 Terahertz sparse deconvolution with data-resolution

In the time domain, the THz reflected signal (electric field) $y(t)$ is the convolution of the incident THz pulse $h(t)$ with the impulse-response function $f(t)$, which corresponds to the structure and properties of the sample at a given point of interest,

$$y(t) = h(t) \otimes f(t) = \int_{-\infty}^{+\infty} h(\tau) f(t-\tau) d\tau. \tag{4.5}$$

For reflective THz imaging, the incident THz pulse $h(t)$ can be obtained by first recording the THz signal reflected from a metal plate (THz reference signal), and then multiplying the reference signal by a factor of -1 for phase correction. In practice, we should consider the discrete form of Eq.4.5 with the sampling period T_s,

$$y_n = \sum_{m=0}^{M-1} h_m f_{n-m} + e_n, \tag{4.6}$$

where $y_n = y(nT_s)$, $h_m = h(mT_s)$ and e_n accounts for the noise originating from the measurement system and materials with n and m as the indices of data points, and M as the length of the data points. Let column vectors $\mathbf{y}$, $\mathbf{h}$, $\mathbf{f}$ and $\mathbf{e}$ collect the samples of y_n, h_n, f_n and e_n, respectively. Then Eq. (4.6) can be expressed as

$$\mathbf{y} = \mathbf{H}\mathbf{f} + \mathbf{e}, \tag{4.7}$$

where $\mathbf{H}$ is the convolution matrix whose rows are delayed versions of the reversed vector of $\mathbf{h}^\mathsf{T}$ or, equivalently, whose columns are delayed versions of $\mathbf{h}$.

The basic idea of sparse deconvolution is to achieve the impulse response function by exploiting the sparse constraint. It aims at approximating the received THz signal $\mathbf{y}$ with $\mathbf{Hf}$ where $\mathbf{f}$ is a sparse sequence; that is, $\mathbf{f}$ has only few non-zero components. In this case, the sparse vector $\mathbf{f}$ can be computed by solving the l_0 regularized optimization problem, which is defined as

$$\min_{\mathbf{f}} \frac{1}{2} \|\mathbf{H}\mathbf{f} - \mathbf{y}\|_2^2 + \lambda \|\mathbf{f}\|_0, \tag{4.8}$$

where $\|\mathbf{f}\|_0$ is the l_0-norm of $\mathbf{f}$, which is defined to be the number of nonzero entries in $\mathbf{f}$, and λ is the regularization parameter, which controls the tradeoff between the

sparsity of $\mathbf{f}$ and the residue norm.

Solving the non-convex l_0 regularized optimization problem in Eq. 4.8 is known to be nonpolynomial (NP) hard and the global optimum cannot be guaranteed. It has already been shown that this non-convex optimization problem can be approximated with a convex optimization problem by replacing the l_0 penalty with the l_1 penalty as

$$\min_{\mathbf{f}} \frac{1}{2}\|\mathbf{Hf} - \mathbf{y}\|_2^2 + \lambda\|\mathbf{f}\|_1, \tag{4.9}$$

where $\|\mathbf{f}\|_1$ is the l_1-norm of $\mathbf{f}$, which is defined as the sum of the absolute values of its components. Since the l_1 norm is convex, a global optimum can be guaranteed.

The iterative shrinkage algorithm, which has been developed recently and is able to address the above optimization problem effectively, is utilized in this paper. Generally speaking, in the iterative shrinkage algorithm, each iteration involves matrix-vector multiplication involving $\mathbf{H}$ and $\mathbf{H}^\mathsf{T}$ followed by a shrinkage or soft-thresholding step. Specifically, the general iterative procedure is given by:

$$\mathbf{f}_{i+1} = S_{\lambda\tau}\left(\mathbf{f}_i - \tau\mathbf{H}^\mathsf{T}(\mathbf{Hf}_i - \mathbf{y})\right), \tag{4.10}$$

where τ is an appropriate step size, which should obey

$$\tau < \frac{2}{\|\mathbf{H}^\mathsf{T}\mathbf{H}\|_2}, \tag{4.11}$$

in order to guarantee convergence, and the shrinkage or soft-thresholding operator $S_{\lambda\tau}$ is defined as

$$S_{\lambda\tau}(f[n]) = \begin{cases} f[n] + \lambda\tau & f[n] \leqslant -\lambda\tau \\ 0 & |\, f[n]\,| < \lambda\tau \\ f[n] - \lambda\tau & f[n] \geqslant \lambda\tau \end{cases}. \tag{4.12}$$

A thorough theoretical analysis in [71] proves the convergence of this iterative shrink-

age algorithm guaranteeing that the solution is the global minimizer for convex $\mathbf{f}$. Obviously, the time-resolution of the obtained impulse response function $\mathbf{f}$ by sparse deconvoltuion depends upon the time-resolution of the reference signal $\mathbf{h}$, which is itself determined by the discretization precision, corresponding to the data sampling period T_s.

4.2.2 Terahertz sparse deconvolution with super-resolution

Compared with conventional deconvolution, one of the advantages of sparse deconvolution is that it can achieve super-resolution. The time-resolution of sparse deconvolution can be increased by an up-sampling approach. Although the reference signal $h(t)$ is measured at the sampling rate of the data T_s, the original discrete $\mathbf{h}$, which contains M data points, can be up-sampled by factor K to form $\mathbf{h}^{sr}$ with time interpolation [72]. In this case, we can consider that the reference signal $h(t)$ is discretized at T_s/K; therefore, the time-resolution of $f(t)$ can also be increased by K times accordingly. The discrete convolution model can be written as the sum of K discrete convolutions as

$$y_n = \frac{1}{K} \sum_{k=0}^{K-1} \left(\sum_{m=0}^{M-1} h_m^k f_{n-m}^k \right) + e_n, \tag{4.13}$$

where h^k are K sub-wavelets with sampling period T_s, such that $h_m^k = h(kT_s/K + mT_s)$, and f^k are the corresponding sparse sub-sequences with M points. In this model, the discrete convolutions based on the original data and $(K-1)$ times more data points from the time interpolation are summed up and averaged to approximate the received signal $\mathbf{y}$. In this model, we do not perform time interpolation on the received signal $\mathbf{y}$, which is still discretized at T_s with the original data-resolution, in order to prevent introducing additional information into $\mathbf{y}$; instead, we apply a sampling and holding approach to deal with $\mathbf{y}$. Then the matrix form of Eq. 4.13 is:

$$\mathbf{y} = \frac{1}{K}\sum_{k=0}^{K-1}\mathbf{H}^k\mathbf{f}^k + \mathbf{e}, \tag{4.14}$$

with $\mathbf{H}^k$ the sub-matrices obtained by taking every Kth row of $\mathbf{H}^{sr}$, which is the convolution matrix based on $\mathbf{h}^{sr}$. By taking this matrix form into the iterative shrinkage algorithm, the general iterative step should be updated to

$$\mathbf{f}_{i+1}^k = S_{\lambda\tau}\left(\mathbf{f}_i^k - \tau\mathbf{H}^{k\mathsf{T}}\left(\frac{1}{K}\sum_{k=0}^{K-1}\mathbf{H}^k\mathbf{f}_i^k - \mathbf{y}\right)\right), \tag{4.15}$$

where the step size τ should satisfy

$$\tau < \min_k \frac{2}{\|\mathbf{H}^{k\mathsf{T}}\mathbf{H}^k\|_2} \tag{4.16}$$

in order to guarantee convergence. By interleaving the obtained K sub-vectors $\mathbf{f}^k$, the final impulse response function with super-resolution $\mathbf{f}^{sr}$, which contains KM data points, can be achieved.

4.2.3 Terahertz sparse deconvolution considering pulse spreading

The performance of sparse deconvolution demonstrated above is mainly limited to the deconvolution of reflective THz signals with time-invariant echoes, which assumes that the THz echoes are time-shifted, amplitude-scaled replicas of the THz reference signal. In practice, however, the reflected THz signals can be both *sparse* and *time-varying* due to the frequency-dependent attenuation and dispersion during the propagation of THz waves in materials. For most materials, this frequency-dependent loss has a low-pass filtering effect on the propagating THz waves and results in temporal pulse spreading [73][74]. For thick multi-layered samples in particular, a shape broadening of echoes, which grows as propagation distance increases, can be clearly observed in the received THz signals. This temporal pulse spreading will definitely degrade the

accuracy of the sparse deconvolution based on time-invariant echoes.

A simple but effective discrete-time pulse spreading model is designed in the following to solve the problem mentioned above. We assume that the temporal spreading of the propagating THz pulse, caused by traveling a distance slice Δz in an attenuative and/or dispersive medium, can be modeled using a linear time-invariant (LTI) system [75], whose impulse response function is $\rho_{\Delta z}(t)$. At depth Δz, the THz pulse $h_{\Delta z}(t)$ can be expressed as:

$$h_{\Delta z}(t) = \rho_{\Delta z}(t) \otimes h_0(t), \tag{4.17}$$

where $h_0(t)$ is the THz pulse at $\Delta z = 0$, corresponding to the original THz reference signal. Accordingly, a model of the pulse spreading associated with traveling a multiple of this distance, $z_n = N\Delta z$, is obtained by serially connecting the above mentioned LTI system N times. The impulse response of the serially connected LTI system is modeled as an N-time self-convolution of the impulse response function of the LTI system associated with a material slice of thickness Δz. Therefore, at depth $N\Delta z$, the THz pulse $h_{z_n}(t)$ will be governed by

$$\begin{aligned} h_{z_n}(t) &= \rho_{\Delta z}(t) \otimes \rho_{\Delta z}(t) \otimes \cdots \otimes \rho_{\Delta z}(t) \otimes h_0(t) \\ &= \rho_{\Delta z}^{(N)}(t) \otimes h_0(t), \end{aligned} \tag{4.18}$$

where $\rho_{\Delta z}^{(N)}(t)$ represents N times self-convolution with the kernel function $\rho_{\Delta z}(t)$.

In the discrete model, the distance slice $\Delta z = cT_s$ corresponds to the data sampling period T_s, with c the propagating speed of THz waves in the material. Because Δz is small, the temporal spreading of the THz pulse between the adjacent distance slices must be relatively small, which implies that the discrete form of the impulse response function $\rho_{\Delta z}[n]$ should be close to a Dirac function delayed one sampling period. This means $\rho_{\Delta z}[n] \approx \delta[n-1]$. In this paper, we model the impulse reponse function $\rho_{\Delta z}[n]$

for describing the temporal pulse spreading with a simple form:

$$\rho_{\Delta z}[n] = \begin{cases} a & n = 0 \\ 1 - 2a & n = 1 \\ a & n = 2 \\ 0 & \text{otherwise} \end{cases}, \tag{4.19}$$

where $0 < a \ll 1$ and a determines the severity of the pulse spreading. Note that $a = 0$ yields $\rho_{\Delta z}[n] = \delta[n-1]$, indicating a simple time delay without temporal pulse spreading. In practice, the parameter a can be found by fitting a specific separate echo at a given depth. Let column vector $\boldsymbol{\rho}$ collects the values of $\rho_{\Delta z}[n]$, then matrix $\mathbf{A}$ for describing the pulse spreading throughout the propagating distance can be expressed as

$$\mathbf{A} = \left[\boldsymbol{\rho}^{(1)}\ \boldsymbol{\rho}^{(2)}\ \boldsymbol{\rho}^{(3)}\ \cdots\ \boldsymbol{\rho}^{(n)}\right], \tag{4.20}$$

where $\boldsymbol{\rho}^{(n)}$ represents n times self-convolution with the kernel vector $\boldsymbol{\rho}$. Therefore, in order to include the temporal pulse spreading effect, the convolution matrix form in Eq. 4.7 should be modified to

$$\mathbf{y} = \mathbf{HAf} + \mathbf{e}, \tag{4.21}$$

where the matrix $\mathbf{HA}$ models the THz pulse with temporal spreading. Each column of $\mathbf{HA}$ now represents a THz pulse with temporal spreading for a traveling distance equals to $n\Delta z$, where n is also identical to the column number. Compared with the THz pulses in the adjacent columns, both amplitude decrease and shape broadening with respect to the traveling distance can be observed.

Accordingly, in order to deconvolve this kind of time-varying THz signal with the iterative shrinkage algorithm, the general iterative step should be further modified to

$$\mathbf{f}_{i+1} = S_{\lambda\tau}\left(\mathbf{f}_i - \tau(\mathbf{HA})^{\mathsf{T}}(\mathbf{HAf}_i - \mathbf{y})\right), \tag{4.22}$$

where the step size τ should obey

$$\tau < \frac{2}{\|(\mathbf{HA})^{\mathsf{T}}\mathbf{HA}\|_2}, \tag{4.23}$$

in order to guarantee convergence. It is important to note that, Eq. 4.21 indicates that the temporal pulse spreading is considered from the beginning of the received THz signal. However, it is not a common case. For example, in a typical THz reflective imaging experiment, the first columns of **H** correspond to the THz pulses propagating in air, which is low loss and involves no pulse spreading. In this case, **A** should be divided into two parts by identifying a typical column number n_0 which corresponds to the air/sample interface. To the left of column n_0, **A** is composed of an identity matrix **I**, which is the same as setting $a = 0$; and then after column n_0, by setting $0 < a \ll 1$, the temporal pulse spreading starts to be involved after the air/sample interface. In the case in which the THz pulse encounters several propagating media, one can build a block diagonal matrix **A** composed of the respective media matrices by setting different values of a.

4.2.4 Numerical and experimental verification

Numerical simulations are first performed to verify the iterative shrinkage algorithm for sparse deconvolution with both data-resolution (DR) and super-resolution (SR). An actual THz reference signal generated by the experimental system described in Section IV, which contains 4096 data points with a sampling period $T_s = 0.0116$ ps, is recorded and used in the simulations. An ideal and simple impulse response function

$f_0[n]$, with the same sampling period and number of data points, is assumed

$$f_0[n] = \begin{cases} 1 & n = 1460 \\ 1 & n = 1550 \\ 0 & \text{otherwise} \end{cases} . \tag{4.24}$$

$f_0[n]$ represents a simple one-layered structure, and the time interval between its two peaks corresponds to the thickness of the structure. $f_0[n]$ is convolved with the reference signal $h[n]$ to simulate the received signal $y_0[n]$. Although $h[n]$ is obtained from an actual noisy measurement, the noise is included in the input signal, which is known as a priori. Therefore, we consider this simulation as a noise-free case.

Both DR sparse deconvolution and FWDD are employed to solve this inverse problem and recover the impulse response function from $y_0[n]$ with the knowledge of $h[n]$. For sparse deconvolution, the convolution matrix $\mathbf{H}$ is formed by $h[n]$, and the iteration based on Eq. 4.10 is performed 2000 times with the regulation parameter $\lambda = 0.4$ and the step size $\tau = 1/\|\mathbf{H}^\mathsf{T}\mathbf{H}\|_2$. For FWDD, a Hanning window function is selected to serve as the frequency-domain filter. Since the depth-resolution achieved by FWDD is highly dependent on the cutoff frequency f_c of the frequency-domain filter, we prefer to choose f_c as high as possible; however, with a high value of f_c, a satisfactory SNR of the deconvolved signal may not be guaranteed even after wavelet de-nosing. In practice, $f_c = 4$ THz is the maximum value we can choose to ensure both a high depth-resolution and a satisfactory SNR. Baseline substraction is performed on the deconvolved signal by FWDD.

The simulation results are shown in Fig. 4.9(a). It can be seen that the deconvolution results, $f_{SP}[n]$ and $f_{FWDD}[n]$, which are obtained from DR sparse deconvolution and FWDD respectively, successfully recover the assumed impulse response function, as the locations of the pulses in $f_{SP}[n]$ and $f_{FWDD}[n]$ exactly match the peaks in $f_0[n]$. The width of the pulses obtained by sparse deconvolution is narrower than

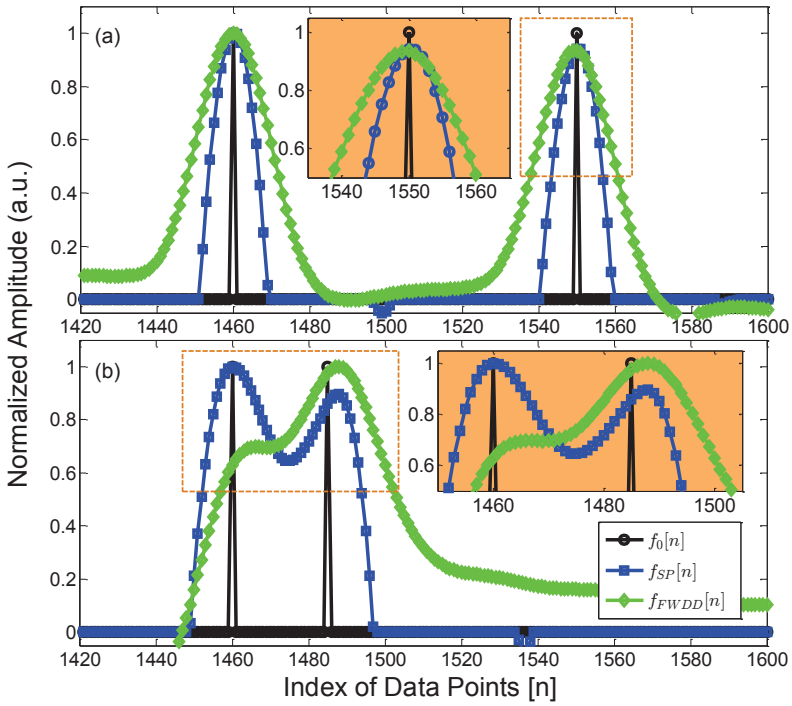

Figure 4.9: Comparisons between the assumed (a)$f_0[n]$ and (b)$f_0'[n]$, and the deconvolution results obtained by sparse deconvolution and FWDD respectively. Insets are the zoom-in images of corresponding boxed peaks.

that obtained by FWDD, which indicates the potential that the minimal time interval resolved with DR sparse deconvolution can be smaller than that with FWDD. The minimal time interval which DR sparse deconvolution is able to resolve can be identified by varying the distance between the two peaks in $f_0[n]$. We determine that the impulse response function with minimal resolvable time interval $f_0'[n]$ is as following:

$$f_0'[n] = \begin{cases} 1 & n = 1460 \\ 1 & n = 1485 \\ 0 & \text{otherwise} \end{cases}, \tag{4.25}$$

in which the time interval between two peaks equals $25T_s$. The deconvolution results are shown in Fig. 4.9(b). We observe that two peaks can be identified based on the results from DR sparse deconvolution, while only one peak can be located based on the results from FWDD. It is important to note that, in practice, for both FWDD and

sparse deconvolution, the minimal thickness resolution, corresponding to the depth-resolution, is dependent on the coherence length, the sampling frequency, and the SNR.

Next, SR sparse deconvolution is utilized to recover $f_0[n]$ and $f_0'[n]$ based on signals with lower time-resolution. Both $f_0[n]$ and $f_0'[n]$ are convolved with the reference signal $h[n]$, and after convolution, the signals are under-sampled by factor 8 to simulate the received signals $y_0[m]$ and $y_0'[m]$, which contain only 512 data points corresponding to a data sampling period $T_s' = 8T_s$. In this case, we consider the time-resolution of $y_0[m]$ and $y_0'[m]$ as the data-resolution. Both DR sparse deconvolution and SR sparse deconvolution are performed based on $y_0[m]$, $y_0'[m]$ and $h'[m]$, which is accordingly the under-sampled version of $h[n]$ by a factor 8. In this simulation, the maximum under-sampling factor is limited by the Nyquist sampling frequency to ensure all the information in the received signal is sampled.

The deconvolution results are shown in Fig. 4.10 for both cases. The DR deconvolution results, $f_{DR}[m]$ and $f_{FWDD}[m]$, which are obtained from DR sparse deconvolution and FWDD respectively, cannot recover the assumed impulse response functions with enough accuracy, as the locations of the peaks in $f_{DR}[m]$ and $f_{FWDD}[m]$ do not exactly match the peaks in $f_0[n]$. In order to increase the accuracy and time-resolution, SR sparse deconvolution based on Eq. 4.15 is employed, and the super-resolution achieved is determined by the up-sampling factor K. In our simulations, with $K = 4$, the SR deconvolution results $f_{SR}[k]$ successfully recover the assumed impulse response function $f_0[n]$, as the locations of the peaks in $f_{SR}[k]$ exactly coincide with the assumed peaks in $f_0[n]$. It is noted that the accuracy of $f_{SR}[k]$ is also affected by the start point in the under-sampling period; in this simulation, with only 4 times up-sampling, we can achieve an accurate recovery. The results thus show that SR sparse deconvolution can overcome the limitation of data-resolution and recover the impulse response function with super-resolution.

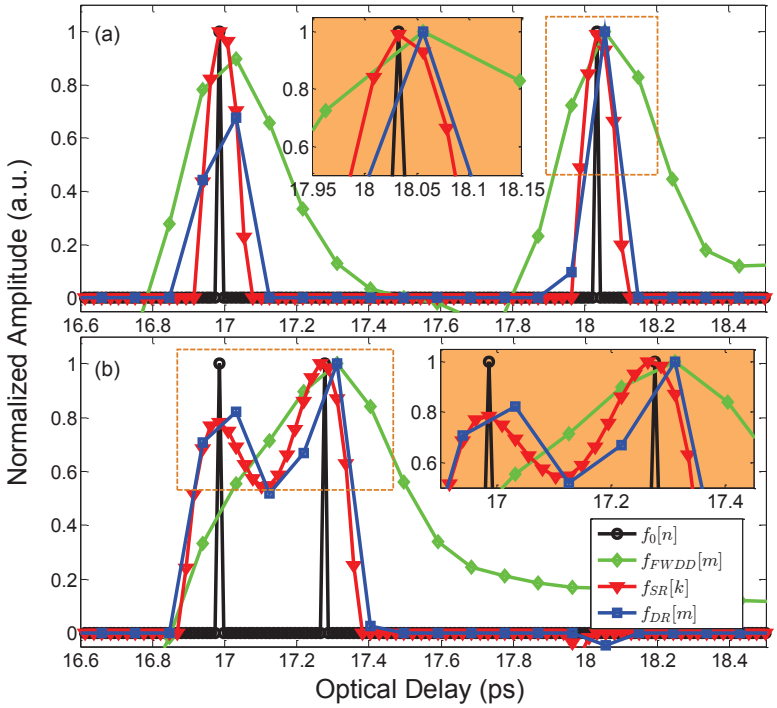

Figure 4.10: Comparisons between the assumed (a)$f_0[n]$ and (b)$f_0'[n]$, and the deconvolution results obtained by DR sparse deconvolution, SR sparse deconvolution with $K = 4$ and FWDD respectively. Insets are the zoom-in images of corresponding boxed peaks.

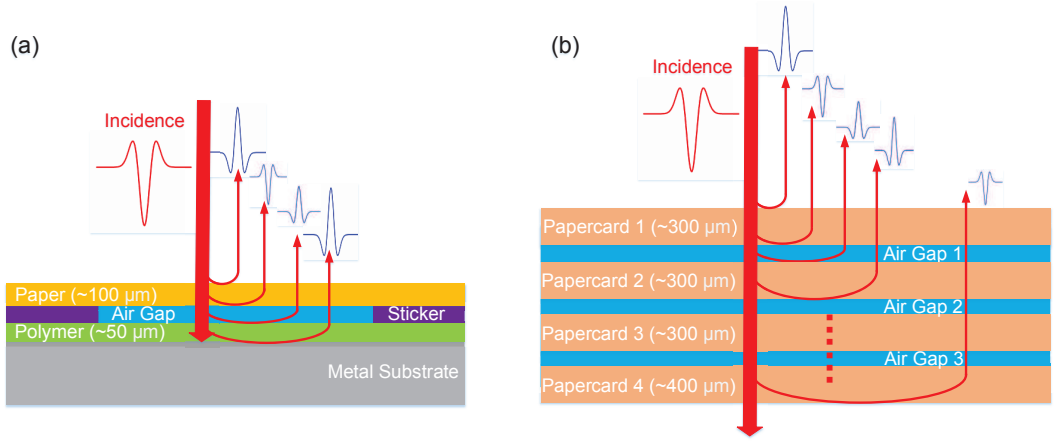

Figure 4.11: Two samples with multi-layered structures. (a) Sample A: a three-layered structure, which is composed of one copy paper, air gap and one polymer coating; (b) Sample B: a seven-layered structure, which is composed of four different papercards with air gaps between them.

Two samples with multi-layered structures are fabricated to verify and evaluate the performance of sparse deconvolution experimentally. The first sample (Sample A), shown in Fig. 4.11(a), is a three-layered structure made by sticking one layer of paper on a polymer-coated steel plate, with an air gap intentionally introduced between the paper (thickness $\sim$ 100 μm) and the polymer coating (thickness $\sim$ 50 μm). The second sample (Sample B), shown in Fig. 4.11(b), is a seven-layered structure obtained by stacking four different papercards. The thicknesses of the first three papers are about 300 μm, and the thickness of the fourth papercard is about 400 μm. Since the papercards are not compressed tightly, air gaps with different thicknesses are also introduced between the papercards.

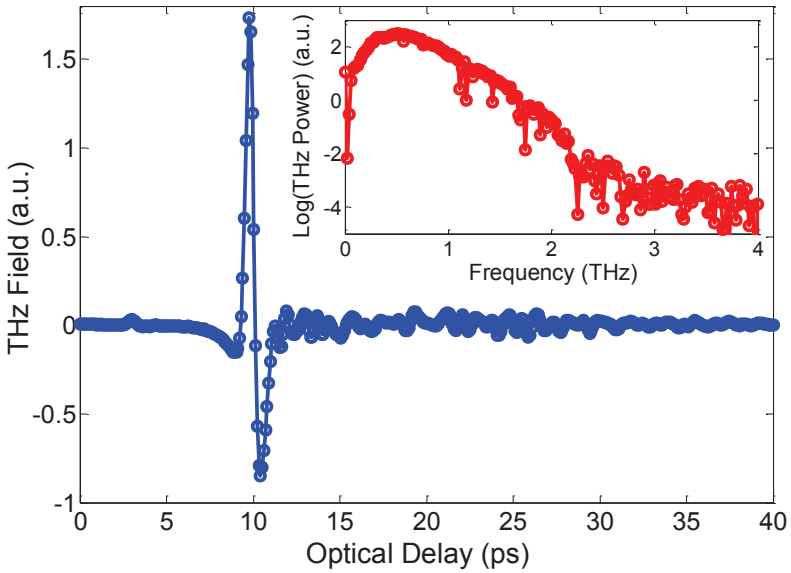

Figure 4.12: The THz reference signal used in the deconvolution of experimental THz received signals, which contains 512 data points with sampling period $T_s = 0.093$ ps. The inset is the frequency spectrum of this reference signal.

The data sampling period in the measurement is set to $T_s = 0.093$ ps. Each recorded reflected temporal THz waveform contains 512 data points, and the signal is averaged over 10 shots. DR sparse deconvolution is applied to reconstruct the sample structures based on the received signals. For the three-layered sample, SR sparse deconvolution is further applied to increase the time-resolution of the arrival times

of echoes. Since both the THz loss and the propagating distance are relatively large in the seven-layered sample, sparse deconvolution including temporal pulse spreading described previously is implemented to increase the accuracy of the reconstruction.

A typical received THz signal reflected from Sample A is shown in Fig. 4.13(a). Since the thickness of each layer is optically thin in the THz regime, this received THz signal is the superposition of several echoes, corresponding to the internal interfaces in the sample. Both DR sparse deconvolution and FWDD are implemented to deconvolve the received signal and the results are compared. It is important to note that, in this section, we consider the THz reference signal (shown in Fig. 4.12) as the input, and the received THz signal as the output; therefore, the actual impulse response function associated with the reflection coefficients should be obtained by multiplying the deconvolved signal by a factor of '-1' for phase correction.

For DR sparse deconvolution, the convolution matrix $\mathbf{H}$ is formed by the experimentally obtained reference THz signal, which contains 512 data points, and the iteration based on Eq. 4.10 is performed 2000 times with the regulation parameter $\lambda = 0.2$ and the step size $\tau = 0.1/\|\mathbf{H}^{\mathsf{T}}\mathbf{H}\|_2$. For FWDD, we utilize the same parameters as the ones we used in the simulations, as $f_c = 4$ THz is the maximum value we can set to ensure the deconvolved signal with both a high depth-resolution and a satisfactory SNR. The deconvolved signals with both methods are shown in Fig. 4.13 (b) and (c). Both of the deconvolved signals can recover the main features of the sample structure. However, by comparison, we can find out that the deconvolved signal from DR sparse deconvolution, which contains sharp peaks and no slow fluctuations, is capable of providing a more clear representation of the various interfaces in the sample than that from FWDD. Furthermore, DR sparse deconvolution is also more effective in resolving small echoes due to the multiple reflections in the samples. The thicknesses of the paper, the air gap and the polymer coating can be calculated based on the measurement of the optical delay between relevant peaks and the knowledge

of the refractive indices. As mentioned before, the time-resolution of the locations of echoes is limited by the sampling period T_s in the experiment.

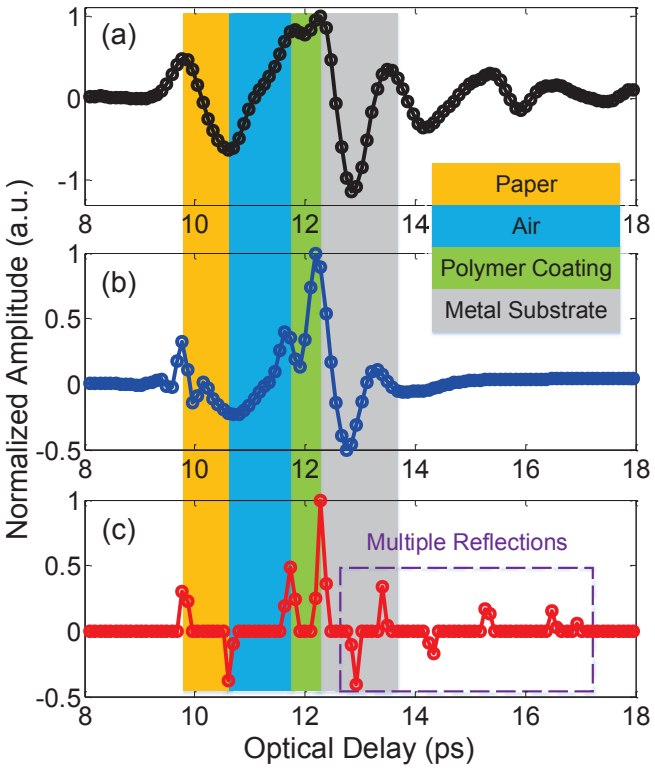

Figure 4.13: The raw and deconvolved signals for Sample A. (a) The received THz signal from Sample A; (b) The deconvolved signal with FWDD; (c) The deconvolved signal with DR sparse deconvolution.

SR sparse deconvolution is further implemented on the received signal from Sample A to increase the time-resolution for more accurate thickness calculation. The SR deconvolved signals with up-sampling factor $K = 2, 4$, and 8 are shown in Fig. 4.14, and are compared with the DR deconvolved signal. As K increases, the accuracy in locating the positions of echoes increases, which leads to a more accurate thickness calculation. It is also noticed that the up-sampling factor K does not need to be too large, as the SR deconvolved signals with $K = 4$ and 8 provide almost the same locations of echoes. The time-resolution achieved here by SR sparse deconvolution is actually limited by the SNR in the received THz signal [76].

Based on the raw and deconvolved signals from Sample A, no temporal pulse

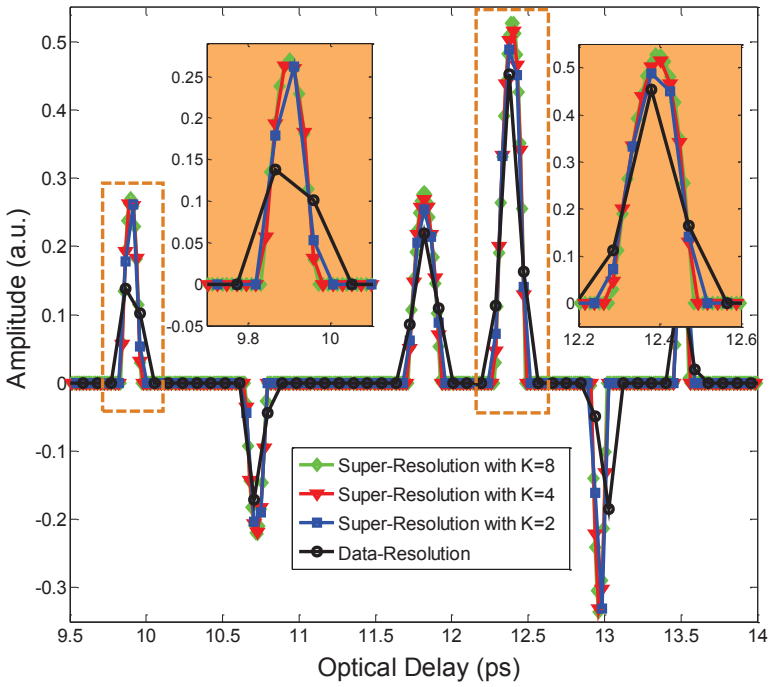

Figure 4.14: Comparison between the DR deconvolved sigal and the SR deconvolved signals with the up-sampling factor $K = 2, 4$ and 8. Two insets are the zoom-in version of the first and fourth peaks.

spreading is clearly observed, since the thickness of sample is relatively small. Sample B, however, is thicker and displays pulse spreading when the THz pulse propagates through. The typical received signal $y_0(t)$ reflected from Sample B is shown in Fig. 4.15 in black. Since the thicknesses of the papercards are large enough, the reflected THz pulses corresponding to the various interfaces between papercards can be clearly identified. However, each pulse indicating the location of the interface is still the superposition of the echoes bouncing back from the front and back interfaces of the air gaps. As the propagating distance increases, a shape broadening can be observed in the THz echoes, which corresponds to the temporal pulse spreading due to the attenuation and dispersion in the papercards. The deconvolved signals with FWDD and DR sparse deconvolution without pulse spreading are shown in Fig. 4.16(a) and (b). Compared with FWDD, sparse deconvolution is more effective in resolving small echoes due to multiple reflections, as smaller amplitudes following the main

pulses corresponding to the air/papercard interfaces can be clearly observed, shown in Fig. 4.16(b). For the deconvolved signal with FWDD, it is obvious that this pulse spreading can also lower the performance of FWDD, as the peaks indicating the locations of interfaces become wider as the propagating distance increases. For the deconvolved signal with DR sparse deconvolution without pulse spreading, the peaks corresponding to the echoes bouncing back from the first and second papercards are quite sharp; however, additional small peaks appear at the last three interfaces, which will definitely obscure the exact locations of the interfaces. The origin of these additional peaks is the temporal pulse spreading. Without including this pulse spreading effect in the algorithm, the input signal is considered as invariant, which is the narrow THz reference signal, and thus a wider THz echo in the received signal will be treated as a combination of several narrow pulses.

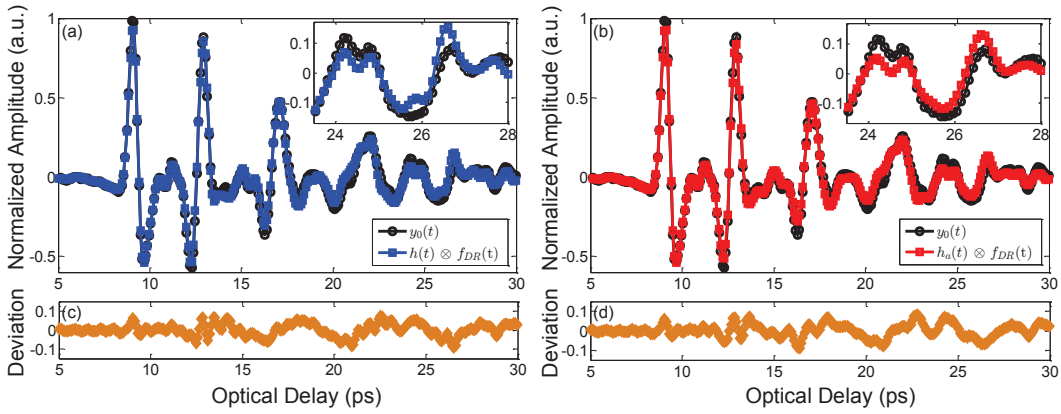

Figure 4.15: Comparsion between the received signal and the re-convolution signal. (a) Comparison between the re-convolution without considering the pulse spreading effect and the actual received signal, and the inset is the zoom-in of the last echo; (b) Comparison between the re-convolution considering the pulse spreading effect and the actual received signal, and the inset is the zoom-in of the last echo; (c) The deviation between $h(t) \otimes f_{DR}(t)$ and $y_0(t)$ in (a); (d) The deviation between $h_a(t) \otimes f_{DR}(t)$ and $y_0(t)$ in (b).

In order to obtain the deconvolved signal with definite and clear locations of interfaces, it is necessary to utilize the sparse deconvolution including pulse spreading to deal with the received signal reflected from Sample B. The most important step in

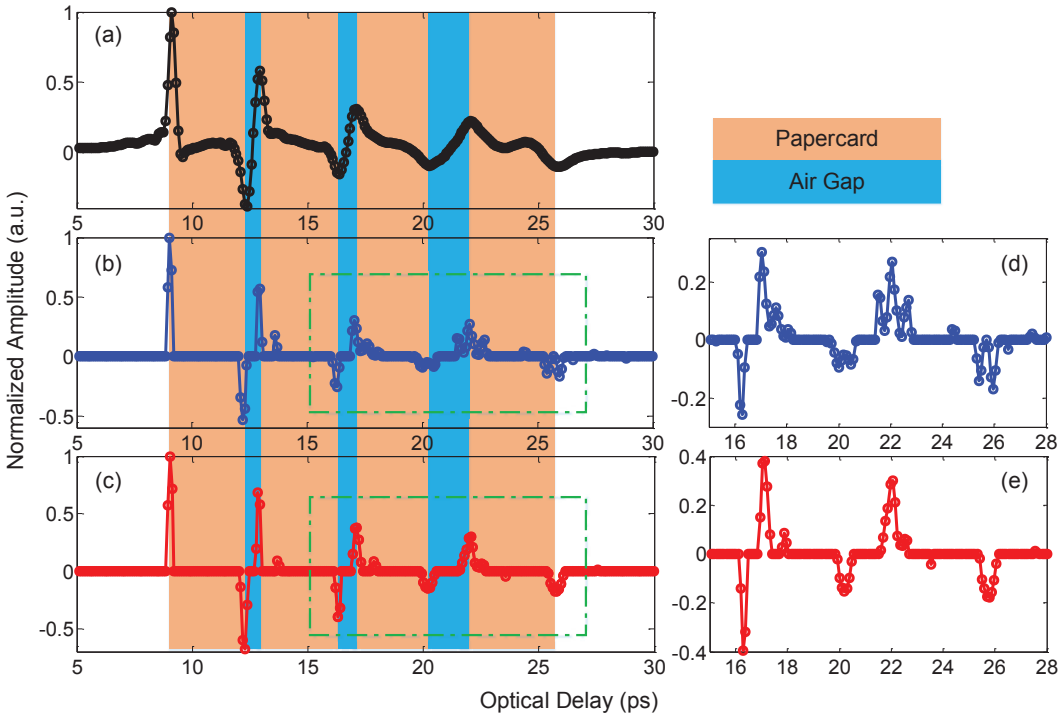

Figure 4.16: Comparison between the deconvolved signals with and without considering the temporal pulse spreading effect. (a) The deconvolved signal with FWDD; (b) The deconvolved signal with sparse deconvolution without considering the pulse spreading; (c) The deconvolved signal with sparse deconvolution including pulse spreading; (d) The zoom-in of the last three interefaces in (b); (e) The zoom-in of the last three interefaces in (c).

this algorithm is the formation of the matrix $\mathbf{A}$. By peak detection, the location of the first air/papercard interface can be identified. This location is considered as the typical column number n_0. Above n_0, $\mathbf{A}$ is filled with an identity matrix, and after n_0, $\mathbf{A}$ is formed based on Eq. 4.20. The key parameter a is determined by multiple trials. In our case, the criterion for the fitness of a is based on the last received THz pulse corresponding to the interface between the back of the last papercard and the air, which should satisfy the following conditions: (1) the deconvolved signal achieved $f_{DR}(t)$ should provide one sharp and clear pulse corresponding to the location of the last interface; (2) $f_{DR}(t)$ is convolved with the input signal including pulse spreading $h_a(t)$, and there should be a good fit between the convolution result $h_a(t) \otimes f_{DR}(t)$ and the received THz signal $y_0(t)$, especially for the last THz pulse. The optimal value we determine in the algorithm is $a = 0.035$, and the corresponding deconvolved signal is shown in Fig. 4.16(c). We observe that, by considering the pulse spreading effect, the spurious peaks, which appear in Fig. 4.16(b), are eliminated, and all the interfaces are clearly located by sharp pulses. Furthermore, the accuracy of the deconvolved signals are confirmed by the re-convolution and the comparison with the actual received THz signal $y_0(t)$, shown in Fig. 4.15. By carefully checking the deviation between the re-convolution and the actual received signal, shown in Fig. 4.15(c) and (d), the deconvolved signal with pulse spreading is more accurate, since smaller ripples in the fluctuations of the deviation can be observed in the region of late-coming echoes. The zoom-in insets of the last THz echoes in Fig. 4.15(a) and (b) further prove the validity of this algorithm.

In this study, sparse deconvolution based on an iterative shrinkage algorithm has been demonstrated for THz characterization of multi-layered structures. Compared with conventional deconvolution, such as FWDD, in which high- and low-frequency noises are inevitably introduced, sparse deconvolution is a pure time-domain technique, which can provide a more clear representation of the impulse response func-

tion with sharp pulses. Since the time-resolution of conventional deconvolution is limited by the discretization precision, a super-resolution version of sparse deconvolution is further developed by an up-sampling approach based on time interpolation, which increases the capability of sparse deconvolution for precise estimation of the arrival times of THz echoes. In addition, the temporal pulse spreading due to the frequency-dependent loss during the THz propagation is also considered in the sparse deconvolution. A simple but effective time-domain model for describing the temporal pulse spreading effect is designed and introduced into the iterative shrinkage algorithm. This model requires little prior knowledge of the properties and structure of the materials, and can greatly improve the performance of sparse deconvolution in processing time-varying THz pulses. The algorithms for sparse deconvolution are all verified with numerical simulations and experimental measurements, which demonstrate that sparse deconvolution is an ideal and effective tool for THz nondestructive characterization of multi-layered structures.

4.3 Terahertz Deconvolution Based on Autoregressive Spectral Extrapolation

Theoretically, the reflected THz signal $r(t)$ is the convolution of the incident THz pulse $i(t)$ with the impulse response function $h(t)$, which should ideally consist of M time-shifted ideal impulses, with the number M corresponding to the material structure; therefore, the Fourier transform of this ideal impulse response function is broadband and should be a sum of M complex sinusoids throughout the entire frequency spectrum. Conventional deconvolution based on direct inverse filtering aims at retrieving the impulse response function by applying the inverse Fourier transform of the transfer function $H_{inv}(f)$, which is the ratio of the reflected to the incident

THz spectra,

$$h_{inv}(t) = FFT^{-1}\big(H_{inv}(f)\big) = FFT^{-1}\left[\frac{FFT\big(r(t)\big)}{FFT\big(i(t)\big)}\right], \tag{4.26}$$

where FFT denotes the Fourier transform and FFT^{-1} the inverse Fourier transform, and $h_{inv}(t)$ is the impulse response function obtained by directly inverse filtering. Frequently, successful deconvolution cannot be expected by directly applying Eq.4.26. Because the THz pulse is band-limited, with a fast-decreasing spectrum outside of the passband (in our case extending from 60 GHz to 3 THz), the division of small values due to the deficiency of THz sources in the low- and high-frequency regions, will give rise to large abnormal values as high spikes and ruin the signal-to-noise ratio there; therefore, $H_{inv}(f)$, as obtained from Eq.4.26 is only valid within the bandwidth with high SNR. Furthermore, these high spikes in the low- and high-frequency regions, where the SNR is low, will introduce severe low- and high-frequency noises in the impulse response function.

THz frequency-wavelet domain deconvolution (FWDD) [54] is specifically designed to enhance the deconvolution process by first employing frequency-domain filtering and then further improving the SNR by wavelet de-noising. Baseline subtraction is also required to cancel the slow fluctuations corresponding to the low-frequency noise. Wiener filtering [54], double Gaussian filter [77] and van Hann filter [65, 68] can serve as the frequency-domain filtering. However, the frequency-domain filtering will narrow the bandwidth of the impulse response function by eliminating the high spikes in the low- and high-frequency regions, and only the frequency components within the bandwidth with high SNR are kept. Therefore, pulses in the impulse response function recovered by FWDD are much wider than the ideal impulses, and consequently, limit the depth-resolution.

In this section, a novel method for enhancing the depth-resolution of THz decon-

volution based on autoregressive spectral extrapolation is developed. This method consists in modeling part of the deconvolved spectrum with high SNR with an autoregressive (AR) process, and to extrapolate the remaining part of the spectrum based on this AR model. What underlies AR spectral extrapolation is the maximum entropy method which consists in determining a spectral estimation that maximizes uncertainty with respect to the unknown information, thus eliminating unreasonable constraints, but that is consistent with the known information [78]. Direct use of the maximum entropy method is marred, however, by the lack of criterion for determining the order of the model used. It has been shown [79] that the maximum entropy method is equivalent to the least squares fitting of an AR process for which mathematical criterion (e.g. Akaike's criterion [80]) exist to determine the length of an AR model. The existence of such a criterion is crucial to avoid over- or under-fitting. In the following, we focus on deconvolution exploiting AR spectral extrapolation, and call this method 'AR deconvolution' for convenience. Unlike FWDD, which discards the frequency components in the low-SNR regions in order to cancel the high spikes, AR deconvolution aims at finding the missing frequency components in the low-SNR regions using an AR model based on the data in the high-SNR regions. With AR deconvolution, the spectrum of the impulse response function throughout the entire frequency band can be estimated, then the inverse Fourier transform leads to a 'quasi-ideal' impulse response function can be achieved, and therefore, the resolution in depth can be enhanced.

4.3.1 Autoregressive model for terahertz spectrum

In an AR process, each data point of H_i of a digitized signal is a weighted sum of its previous p points, plus a noise term N_i,

$$H_i = \sum_{k=1}^{p} a_k H_{i-k} + N_i, \;\; i > p, \tag{4.27}$$

where p is the order of the AR process, a_k are the AR coefficients, and H_i is known within the frequency band ($i_L \leqslant i \leqslant i_H$) with high SNR. This AR model can be used as a prediction filter to find an estimate $\hat{H}_i$ of the unknown values of H_i for $i > i_H$ using the forward prediction equation,

$$\hat{H}_i = \sum_{k=1}^{p} a_k H_{i-k},\ i > i_H. \tag{4.28}$$

Similarly, we can use a backward prediction filter to find the values of H_i for $i < i_L$,

$$\hat{H}_i = \sum_{k=1}^{p} b_k H_{i+k},\ i < i_L, \tag{4.29}$$

where b_k are the coefficients for the backward prediction filter. The optimum values for the coefficients a_k and b_k are determined by minimizing the squared error between the model and the N_{BW} ($N_{BW} = i_H - i_L + 1$) available data points with high SNR.

As mentioned above, the frequency spectrum of the ideal impulse response function, of a multi-layered system, should be the superposition of a limited number of complex sinusoids, each corresponding to a layer interface. It has already been shown that [78], for a noiseless case, this kind of signal, which consists of a sum of complex sinusoids, can be modeled as an AR process with an order equal to twice the number of sinusoids; for a noisy case, this kind of signal should be modeled as an AR process with an order much higher than the number of sinusoids. Akaike's Information Criterion (AIC) [80], which is based on the principle of entropy maximization in information theory, provides a measure for the selection of the model order p, and the AIC of order p can be calculated using the residual sums of squares from regression S_p^2,

$$(AIC)_p = N \ln(S_p^2) + 2p, \tag{4.30}$$

where N is the number of data points, and ln is the natural logarithm. AIC deals with

the trade-off between the goodness of fit of the model and the complexity of the model, and according to Akaike's theory, the most accurate model has the smallest AIC value. For the THz frequency spectrum, both the forward and backward prediction filters are needed to find the missing data in the low- and high-frequency regions, and the AR coefficients are obtained by minimizing the sum of the forward and backward prediction errors ϵ^2,

$$\epsilon^2 = \sum_{i=i_L}^{i_{PL}} |H_i - \sum_{k=1}^{p} b_k H_{i+k}|^2 + \sum_{i=i_{PH}}^{i_H} |H_i - \sum_{k=1}^{p} a_k H_{i-k}|^2, \tag{4.31}$$

with respect to the individual a_k and b_k. In this process, the N_{BW} available data are divided into three parts: (1) data within $[i_{PL}, i_{PH}]$ are the p data which are kept the same and used as the base of the AR model; (2) data within $[i_L, i_{PL}]$ are used for the fitting to find b_k; (3) data within $[i_{PH}, i_H]$ are used for the fitting to determine the a_k. The Burg method is utilized to minimize this error term [81]. By adding the Levinson-Durbin constraint [82], the Burg method enables the AR coefficients to be determined by a fast recursive algorithm, and guarantees a stable prediction filter, which is important to estimate the spectrum throughout the entire frequency band.

4.3.2 Numerical and experimental verification

Teraview TPS Spectra 3000 is employed in this study to perform THz reflective imaging at almost normal incidence in order to obtain the data used in the following numerical and experimental study. The THz reference signal $f_0[n]$, with n as the index of data points, is recorded by setting a metal plate at the sample position, shown in the inset of Fig.4.17. The data sampling period in the measurement is set to $T_s = 0.0116\ ps$. Each recorded reflected temporal THz waveform contains 4096 data points, and the signal is averaged over 10 shots. With this setting, the entire frequency spectrum obtained by Fourier transform is from 0 THz to 85.99 THz, which

also contains 4096 data points.

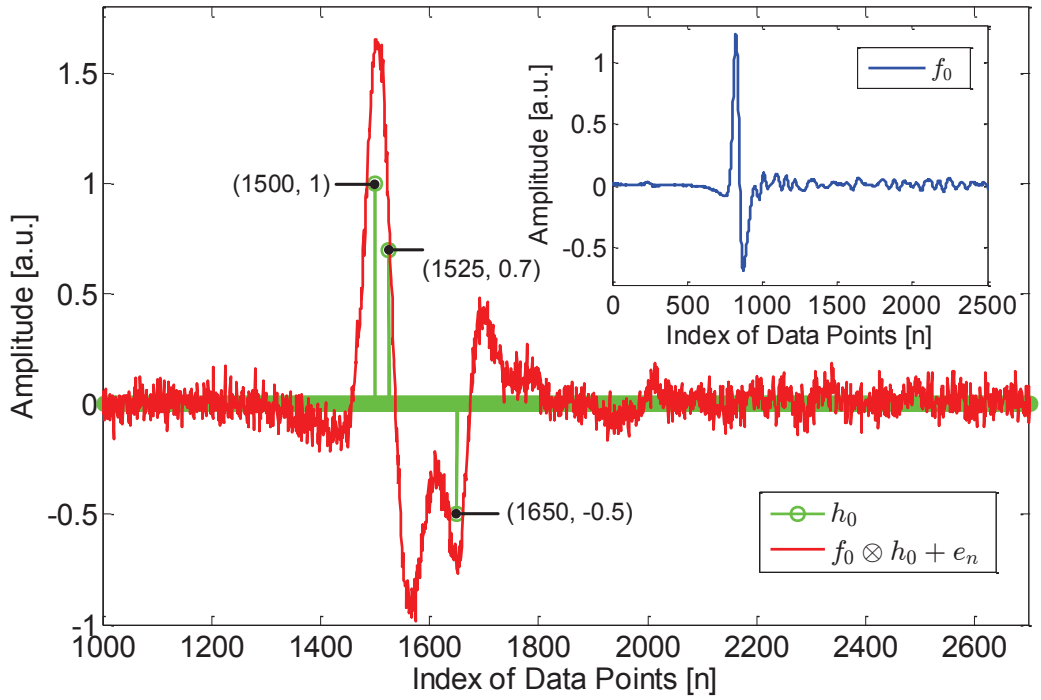

Figure 4.17: The assumed impulse response function h_0 and the simulated received THz signal r_0. The inset shows the actual THz reference signal f_0.

Numerical simulations are first performed to verify the AR deconvolution. An ideal impulse response function $h_0[n]$, which contains 4096 data points with the same sampling period T_s, is assumed and shown in Fig.4.17. $h_0[n]$ represents a simple two-layered structure, and the time interval between the peaks are $25T_s$ and $125T_s$, corresponding to the thickness of each layer. $h_0[n]$ is convolved with the reference signal $f_0[n]$ to simulate the received signal $r_0[n]$. $e[n]$ represents the additive white noise, with which the SNR of r_0 is set to be 10 dB in this simulation.

The assumed frequency spectrum H_0, which ideally consists of a sum of three complex sinusoids and is not bandlimited throughout the frequency band (from 0 THz to 85.99 THz), is obtained by the Fourier transform of h_0. In Fig.4.18(a), H_0 is compared with H_{inv}, which is the direct division of the spectra of r_0 and f_0. By comparison, the low-SNR frequency bands of H_{inv} which contain high spikes corresponding to low- and high-frequency noises, and the high-SNR frequency band

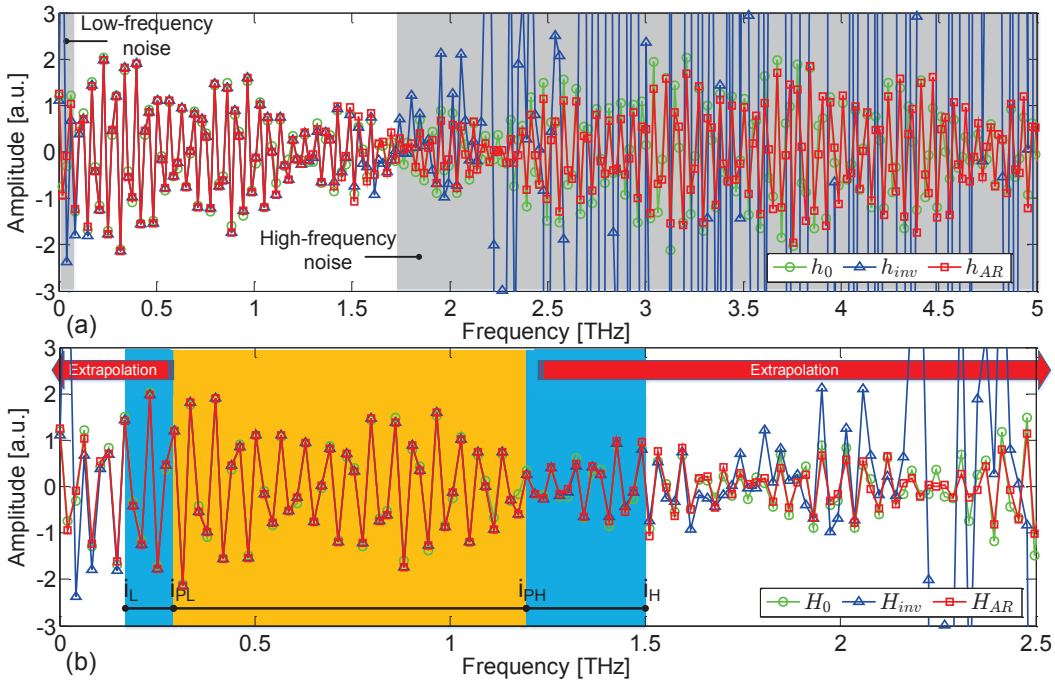

Figure 4.18: (a) Comparison between the assumed frequency spectrum H_0, the deconvolved frequency spectrum by direct inverse filtering H_{inv} and the estimated frequency spectrum by AR spectral extrapolation H_{AR}. (b) The zoom-in of (a), which shows the detailed data allocation for the AR model.

can be well separated and clearly identified. The THz frequency spectrum has a large bandwidth with high SNR, which enables us to establish an AR model with a high order. Considering the THz bandwidth and the SNR of our TDS system, we fit the AR model to the N_{BW} available data with $i_L = 0.17$ THz and $i_H = 1.5$ THz. By setting $i_{PL} = 0.3$ THz and $i_{PH} = 1.2$ THz, we allocate the data within $[0.3, 1.5]$ for the forward prediction filter, and the data within $[0.17, 1.2]$ for the backward prediction filter. AIC values with different orders are calculated and shown in the inset of Fig.4.19. The smallest AIC value is achieved when p equals to 44. Fig.4.18(b) shows the detailed data allocation for this AR process. After fitting this AR model to the N_{BW} available data, we apply this AR model as a prediction filter to extrapolate the data to find the missing data in the regions below 0.18 THz and above 1.5 THz (up to 85.99 THz). Note that this is well outside the bandwidth of our imaging system; the ability to recover data out to this high frequency depends on our having sufficient knowledge of the frequency spectrum to construct an accurate AR model. The estimated frequency spectrum H_{AR} based on this AR model is shown in red in Fig.4.18. By comparison between H_{AR} and H_0, we can find out that the estimated frequency components in H_{AR} match the assumed data in H_0 quite well, which verifies the effectiveness of this AR model to recover the missing data. By simply performing the inverse Fourier transform of H_{AR}, the deconvolved signal h_{AR}, can be achieved.

In Fig.4.19, h_{AR} is compared with h_{FWDD}, which is the deconvolved signal obtained by FWDD, and the assumed impulse response function h_0. For FWDD, van Hann filter is selected to serve as the frequency-domain filter to suppress the high-frequency noise, and the maximum value of the cutoff frequency we can set is $f_c = 3.5$ THz in order to obtain a satisfactory SNR of the deconvolved signal. More details about the FWDD algorithm we use can be found in [83]. With FWDD, only the first and the third interface can be identified, and the first assumed layer with time interval $25T_s$ (corresponding to an air gap with thickness of 43.5 μm) cannot be resolved. In

contrary, h_{AR} is able to resolve all the interfaces, and exhibits a 'quasi-ideal' impulse response function compared with the assumed impulse response function h_0. Based on this simulation, we can conclude that the minimum thickness resolved by THz reflective imaging, is enhanced by AR deconvolution, since the frequency components throughout the entire spectrum are estimated and recovered. It is important to note that the minimum thickness (time interval) resolution , corresponding to the depth-resolution, is mainly dependent on the bandwidth of the THz source, the sampling frequency and the SNR. In our simulations, the minimum time interval which can be resolved by AR deconvolution with the SNR $= 10\ dB$ is $15T_s$ (corresponding to an air gap with thickness of 26.1 μm); on the other hand, the minimum time interval resolved by FWDD with the same SNR is $30T_s$. Therefore, the depth-resolution can be increased by a factor of two using AR deconvolution.

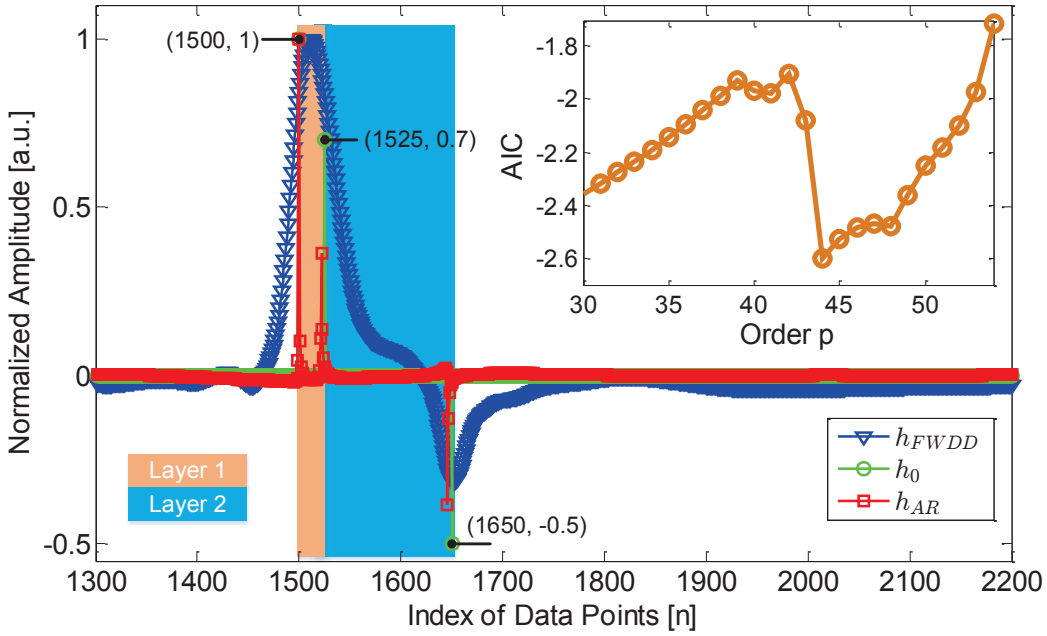

Figure 4.19: Comparison of the simulated deconvolution results obtained by AR deconvolution with $p = 44$, FWDD and the assumed impulse response function. The inset shows the AIC values with different model orders.

Next, a one-layered polymer coating on a steel substrate is employed in this study to verify the effectiveness of AR deconvolution experimentally. The thickness of the

polymer coating is about 22.5 μm, which is thin in the THz regime. THz reflective imaging experiment was performed, and the typical waveform received is shown in the inset of Fig.4.20(a). Since the coating is very thin and the steel substrate provides total reflection, the reflected signal is similar to the reference signal and no overlapping echoes can be observed in time domain. Both FWDD and AR deconvolution are performed to resolve this thin coating layer. In the deconvolution, we consider the THz reference signal as the input and the received THz signal as the output; therefore, the actual impulse response function associated with the Fresnel coefficients can be obtained by multiplying the deconvolved signal by a factor of -1 for phase correction. For FWDD, the maximum cutoff frequency leading to a satisfactory SNR in time domain is 4 THz; For AR deconvolution, we set the parameters the same as the ones we used in the simulation. Based on the AR model, the frequency components outside the frequency window with high SNR are estimated and the entire frequency spectrum of the impulse response function is recovered successfully. The frequency spectrum should ideally consist of two sinusoids, shown in Fig.4.20(b). The deconvolution results based on FWDD and AR deconvolution are shown in Fig.4.20(a). Compared with the deconvolved result by FWDD, which only shows one peak, the deconvolved signal based on AR deconvolution successfully resolves the thin coating layer and presents a clear representation of the sample structure. Therefore, we can conclude that the resolution in depth can be significantly enhanced by AR deconvolution.

In this section, AR deconvolution which is based on autoregressive spectral extrapolation, is presented to enhance the depth-resolution of THz deconvolution. The de-noising procedure in the conventional deconvolution, such as FWDD, narrows the bandwidth of the impulse response function by eliminating the frequency components in the low-SNR regions, and therefore, lowers the resolution in-depth. On the contrary, AR deconvolution aims at recovering the missing frequency components in the low-SNR regions using the AR model based on the frequency components

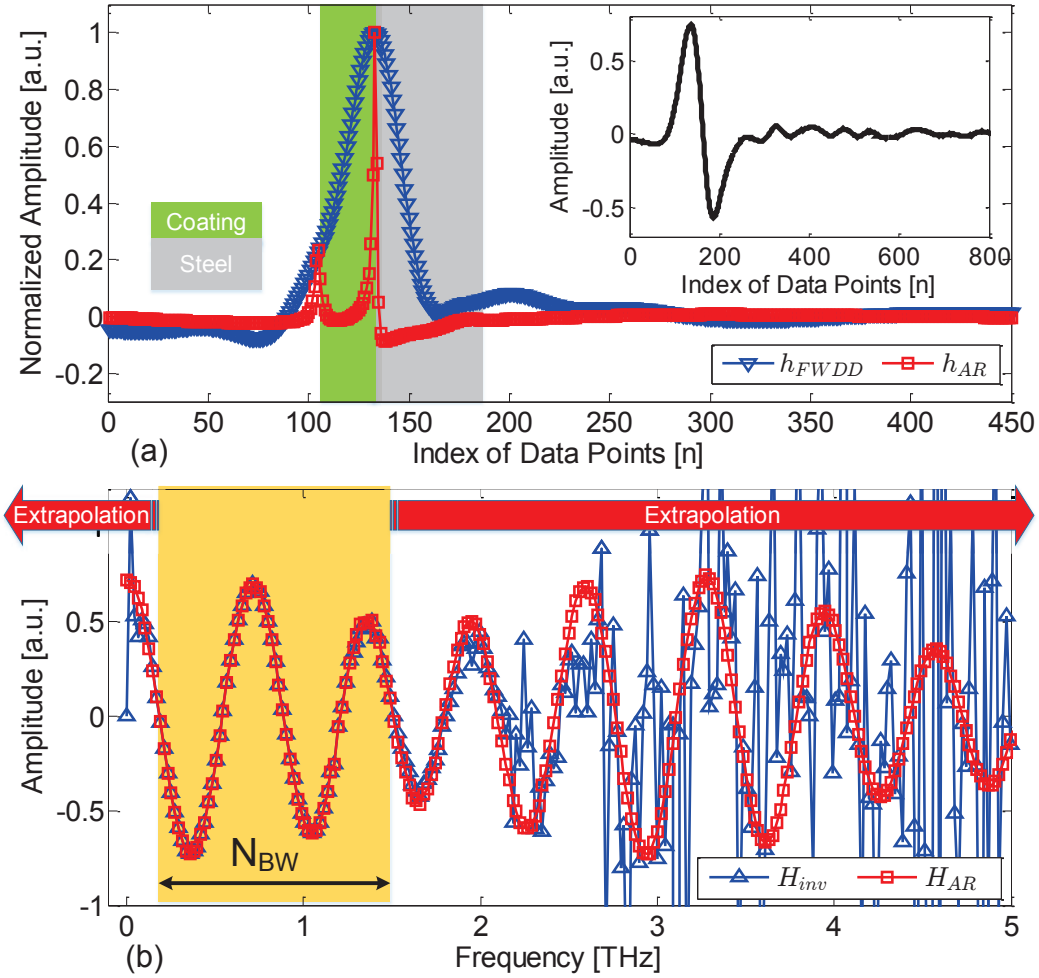

Figure 4.20: (a) The deconvolution results based on FWDD and AR deconvolution. The inset shows the received THz signal reflected from the poly-coated steel sample; (b) The estimated frequency spectrum (up to 5 THz) based on autogressive spectral extrapolation.

in the high-SNR regions. In this way, the entire spectrum of the impulse response function is estimated, and a 'quasi-ideal' impulse response function with enhanced depth-resolution is achieved. We find out AR deconvolution is very suitable to deal with THz TDS signals, as the THz spectrum provides a large bandwidth with high SNR to establish a high-order AR model. It is also important to note that the deconvolution result is sensitive to the selection of parameters and SNR when a high-order AR model is utilized. This method is verified numerically and experimentally with a one-layered polymer coating with thickness of 22.5 μm, which cannot be resolved by FWDD. The thickness is successfully resolved by AR deconvolution, demonstrating that AR deconvolution enables us to beat the limitation of the THz wavelength and enhance the depth-resolution for resolving the optically thin layers in the THz regime.

CHAPTER 5

TERAHERTZ REFLECTOMETRY OF ART PAINTINGS

Studies at the intersection between the quantitative sciences and the humanities have been especially fruitful in the last few decades with the availability of new spectroscopic tools that permit noninvasive studies of art. In particular, physical characterization of art using emerging tools may provide information that conclusively confirms or refutes judgments based on connoisseurship. Determination of the physical characteristics, not only across a painting but also in depth, is one of the most important procedures to gain insight into its structure. The layer-by-layer structure, or stratigraphy, reveals the sequential application of the preparatory and ground layers on the support (e.g., canvas or wood panel), pictorial layers, and varnish, as well as of possible subsequent revisions or restorations. A detailed knowledge of the stratigraphy provides a basis for evaluation of its authenticity and attribution, insight into historical or artist-specific techniques for art-historical studies, as well as the recognition of any decay and of consequent conservation and/or restoration requirements. For paintings, stratigraphic analysis can reveal the way in which the paint layers are applied, and consequently, tell us how the artist worked. The conventional approach to obtain information on the stratigraphy is based on the characterization of the cross-sections of micro-samples taken from the objects with standard micro-analytical tools, such as visible-light and electron microscopy, energy-dispersive X-ray spectroscopy, Raman and infrared spectroscopy [84]. This approach is invasive, resulting in the destruction of the integrity of the painting. Various noninvasive and noncontact modalities which can provide *in-situ* quantitative information in depth, such as confocal X-ray fluorescence (with elemental distribution contrast) [85], femtosecond pump-probe microscopy (with molecular and structural constrast) [86], nuclear magnetic resonance

(with ^{1}H abundance constrast) [87], and optical coherence tomography (with structural constrast) [88], are under active research. Although with micrometer-level high resolution, these methods have limited penetration in depth, or imply probing a small region of interest, as opposed to an extended area, and therefore, cannot generate a 3D global mapping of the layer structure of a painting [89].

Due to the penetrative capability of THz electromagnetic radiation in broad classes of nonmetallic material, THz reflectometry based on THz time-domain spectroscopy (THz-TDS) systems has attracted considerable interest for revealing the stratigraphy in-situ, as well as hidden features of art paintings. THz reflectometry may provide information in depth by analyzing the reflected THz signal with an incident approximately single-cycle THz pulse. Due to dielectric discontinuities with depth associated with the various paint and other layers in the painting, reflected temporal THz echoes associated with the Fresnel coefficients at various interfaces are recorded as a function of transverse position in amplitude and time delay. The stratigraphy of paintings can be reconstructed by precise extraction of THz echo parameters from the reflected THz signal. So far, some panel paintings and wall paintings have been studied by THz reflectometry, in which certain details of the stratigraphy have been revealed. However, the main challenge for THz reflectometric characterization of stratigraphy in historial paintings is to resolve the optically thin paint-layers, which is much less than the time over which the THz pulse propagates within its duration, corresponding to the depth resolution of a typical THz-TDS system.

In the last chapter, it is shown that deconvolution, which can yield sub-wavelength and sub-pulse-width depth resolution, is an effective technique for resolving the overlapping echoes and characterizing the stratigraphy. The resulting impulse-response function provides a new imaging domain, which is entirely dependent on the sample structure. In this chapter, THz reflectometry with enhanced depth-resolution by deconvolution is utilized to characterize the stratigraphy and subsurface features of two

historical paintings. The first one is a 19th century Italian oil painting on paperboard, *After Fishing*, by Ausonio Tanda. The characteristic paint-layer thickness is larger than 50 μm, and FWDD is applied to resolve the overlapping echoes. The subsurface features are clearly revealed and the stratigraphy is successfully reconstructed. The second painting is a 17th century Italian easel painting, *Vièrge en priere*, in which the characteristic paint-layer thickness is smaller than 50 μm. THz reflectometry based on sparsity-based time-domain deconvolution is applied to characterize the detailed stratigraphy in *Vièrge en priere*. The sparsity-based impulse-response function achieved provides a detailed 3D mapping of the layer structure of *Vièrge en priere*, in which the structure of the canvas support, the ground, imprimatura, underpainting, pictorial, and varnish layers are clearly identified. In addition, a hitherto unidentified restoration of the varnish has been found. This is the first time to our knowledge THz reflectometry has resolved multiple layers in an easel painting with such thin layers.

The case studies in this chapter show that THz reflectometry can be considered as an effective modality for in-situ 3D global imaging of historical paintings, as well as a broad range of cultural heritage objects.

5.1 Terahertz stratigraphic and subsurface investigation of a 20th century Italian oil painting on paperboard

In this section, THz reflective imaging in conjunction with advanced signal processing is employed for the stratigraphic and substrate investigation of art painting. In order to resolve the optically thin paint layers, a deconvolution technique is enhanced by the combination of frequency-domain filtering and stationary wavelet shrinkage, and applied to investigate a mid-20th century Italian oil painting on paperboard, *After Fishing*, by Ausonio Tanda, shown in Fig.5.1. Based on the deconvolved THz data, the stratigraphy of the applied paint is reconstructed and subsurface features are clearly revealed, demonstrating that THz frequency-wavelet deconvoltuion can be an

effective tool to characterize stratified systems with optically thin layers.

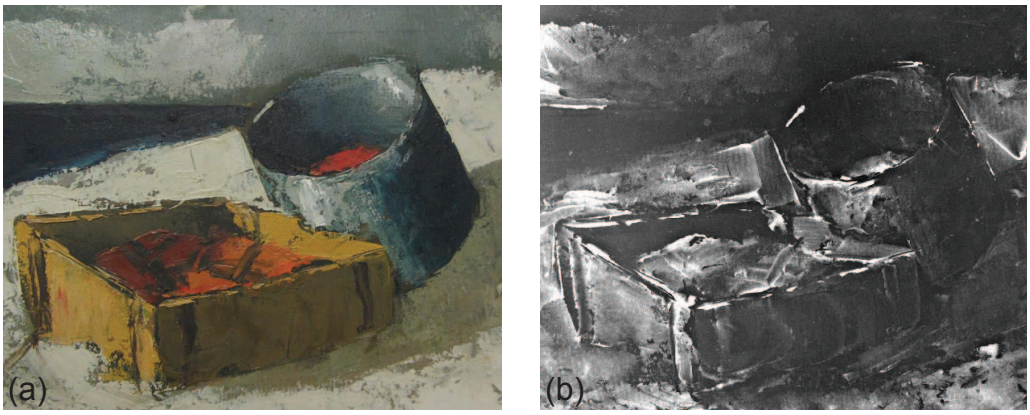

Figure 5.1: Images of *After Fishing* by Ausonio Tanda. (a) Visible photograph of *After Fishing*, and (b) X-ray transmission image of *After Fishing*.

5.1.1 Terahertz raw images of *After Fishing*

In the following, THz imaging results of *After Fishing* based on the raw THz data are presented first, then THz frequency-wavelet domain deconvolution is applied to the THz raw data to obtain the THz deconvolved data, based on which the stratigraphy and subsurface features of the painting are obtained.

The THz C-scan in the time domain, which provides important information about the surface features of the painting, is shown in Fig. 5.2. THz C-scans in the frequency domain can also be obtained by taking the Fourier transform of the waveform at each pixel, shown in Fig. 5.3. Higher frequency, corresponding to shorter wavelength, is helpful for observing small and subtle features. For example, as we progress from Fig. 5.3(a) to (d), in the upper left region (between pixels 0 and 50 in the X direction, and 150 and 200 in the Y direction) a ripple pattern with periodicity approximately in the X direction emerges as the cutoff of the frequency window increases. Note that 1.2 THz corresponds to a wavelength of ~ 0.25 mm, which is on the length scale of the periodicity of the ripples. These features are due to the clarity of the features in the THz C-scan at 1.2 THz, which indicates that the signal-to-noise ratio at 1.2

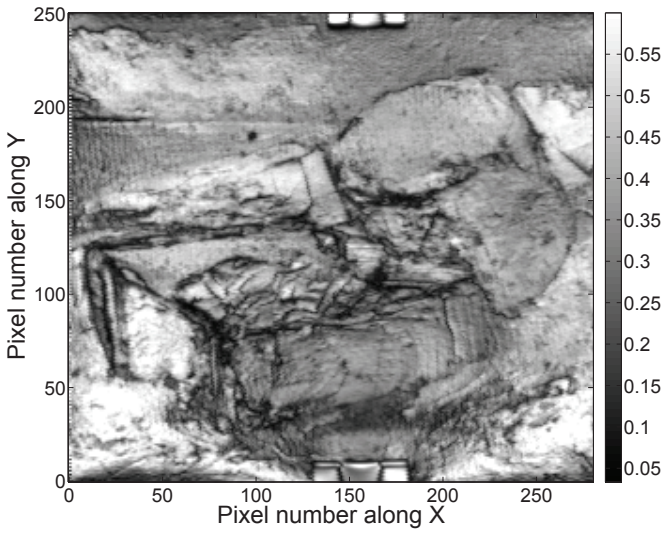

Figure 5.2: THz C-scan image of *After Fishing* in time domain based on the raw data.

THz is still acceptable; consequently, the cutoff frequency f_c can be selected slightly higher than 1.2 THz to obtain higher time resolution in the deconvolution procedure.

By contrast with the X-ray transmission image in Fig. 5.1(b), one striking feature observed are several small and blurred spots randomly distributed in the frequency-domain THz C-scans; these spots are not observed in the X-ray transmission image. By carefully checking the THz waveforms at relevant pixels, small echoes can be found in the time interval 12 to 28 ps, corresponding to the paperboard support. The THz B-scan together with the THz C-scan clearly locate the four highlighted spots in three dimensions, shown in Fig. 5.4. These spots are a result of defects in the paperboard, which is speculated may be due to oil and/or biological growth. Because organic materials containing mainly light atoms present low radiological contrasts, they are difficult to detect by standard X-ray systems [90]. THz B-scans based on the raw data cannot provide the stratigraphic detail, since separation of the paint layers above the paperboard cannot be resolved. Artifacts (weak horizontal lines) due to ambient water-vapor and the system noise also lower the quality of the THz B-scans.

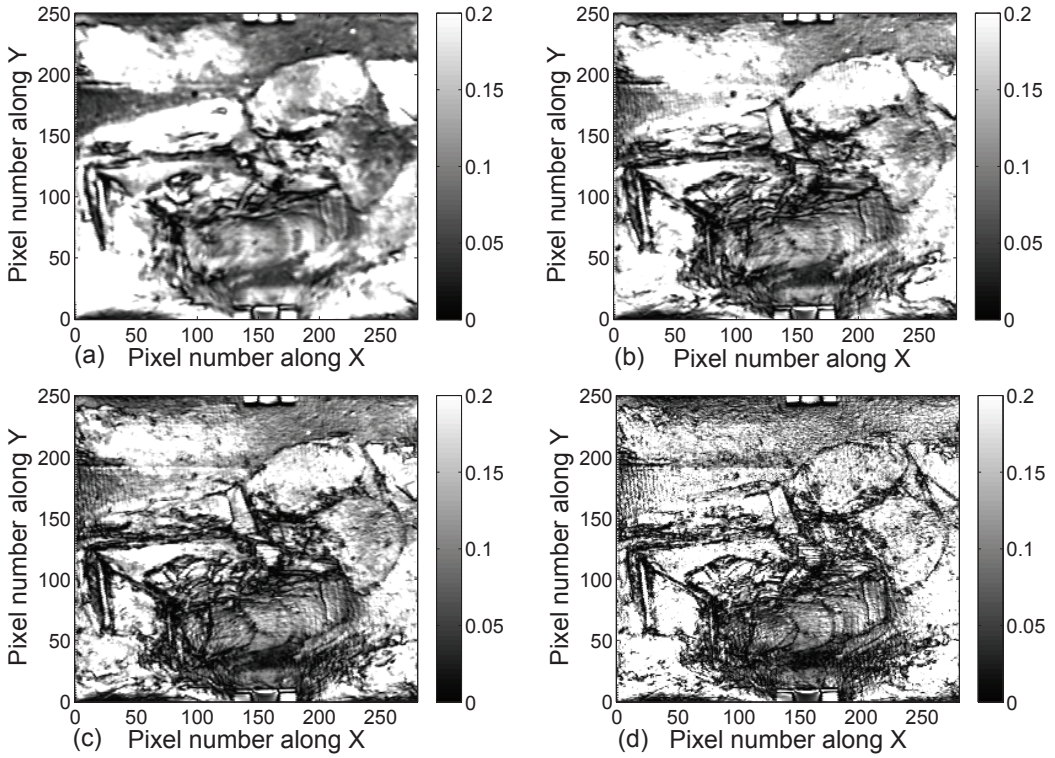

Figure 5.3: THz C-scan images of *After Fishing* in frequency domain at (a) 0.4, (b) 0.6, (c) 0.8, and (d) 1.2 THz.

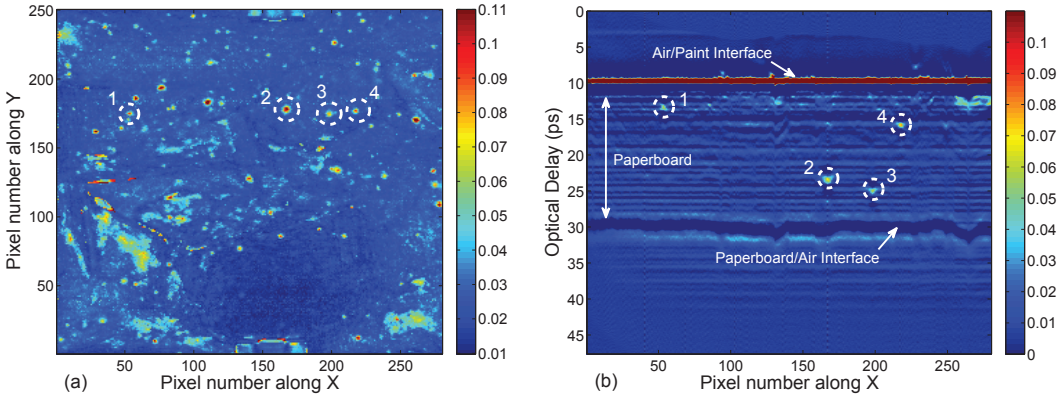

Figure 5.4: THz imaging results of the 'Spots' location in the paperboard.

5.1.2 Reconstruction of stratigraphy based on FWDD

To extract features associated with optically thin layers that might be obscured in the raw THz signals, the THz frequency-wavelet deconvolution technique is employed to the raw reflected THz signal at each pixel. A typical THz waveform reflected from the painting is shown in Fig. 5.5(a). Echoes reflected from the top and bottom surfaces of the painting can be clearly identified, and overlapping echoes due to the internal structure just following the first peak can also be observed. A comparison is made with two different cutoff frequencies in order to choose a suitable f_c in the frequency-wavelet domain deconvolution algorithm. For f_c=1 THz, shown in Fig. 5.5(b), the signal after deconvolution with frequency-domain filtering exhibits a good signal-to-noise ratio; however, the peak indicating the underlying paint layer is not well separated; for f_c=1.5 THz, shown in Fig. 5.5(c), the hidden peak can be well separated and clearly identified, although the signal-to-noise ratio is relatively low. The residual noise in both cases can be effectively attenuated with wavelet de-noising. The final deconvolution result of this typical THz waveform is shown in Fig. 5.5(d), which clearly exhibits the stratigraphy of the painting including one additional underlying paint layer at this single pixel. Therefore, the cutoff frequency f_c chosen for all the waveforms is 1.5 THz. In order to reconstruct the stratigraphy and investigate subsurface features, peak detection is performed on the deconvolved signals for identifying the existence of an interface. A threshold value for peak detection is set for all pixels, above which a feature is considered as a valid peak. Based on the features of the peak detection results, the deconvolved signals can be mainly classified into four types, shown in Fig. 5.6.

THz imaging results in the following are presented according to the classification of the deconvolved THz signals. For Type I, shown in Fig.5.6(a), a small peak occurs before the arrival of the main peak corresponding to the air/paint interface. This feature is due to the diffuse reflection on a rough surface. Since the focus spot of the

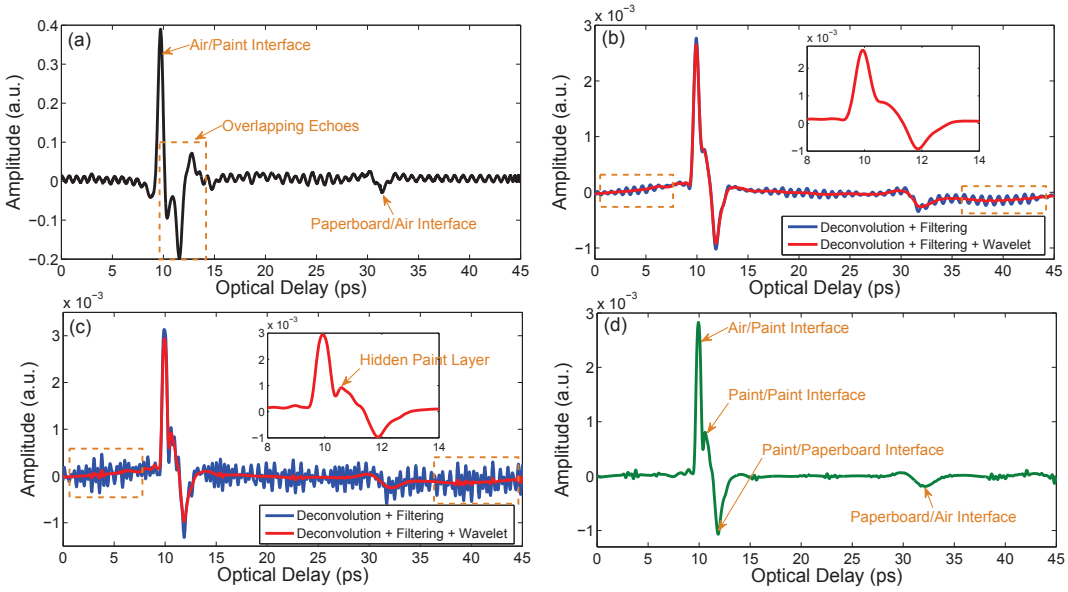

Figure 5.5: THz frequency-wavelet deconvolution result for a typical THz waveform.

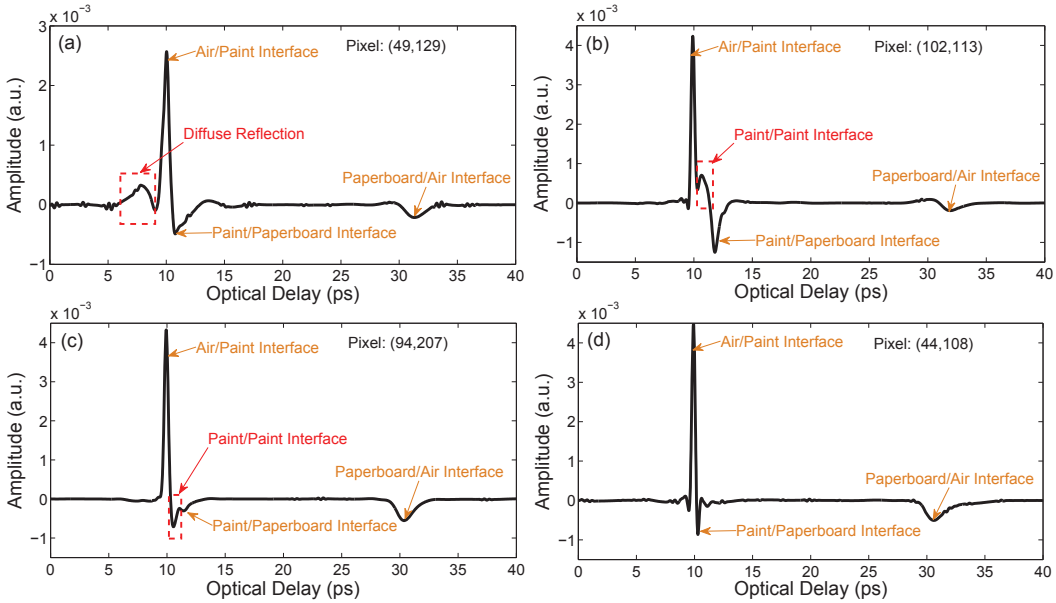

Figure 5.6: Four different types of the deconvolved signals with (a) (d) corresponding to Type I Type IV.

THz beam has limited size, if the surface within this spot is rough and contains height variation, some portion of the THz beams will reflect earlier than the other portion of the beam, which leads to peaks in the reflected THz signal before the dominant peak. A THz C-scan based on the amplitude of the peak before the main peak for Type I signals is plotted in Fig. 5.7(a). This C-scan mainly displays the outlines of the drawing objects in the foreground, the paint for which may contain angles and edges. A THz C-scan based on the amplitude of the main peak corresponding to the air/paint interface is also plotted in Fig. 5.7(b). By comparing these two C-scans, we see that they are complementary– positive and negative images. Areas with high values in Fig. 5.7(a) exhibit relatively low values in Fig. 5.7(b), which also supports our assertion concerning the role of diffuse reflection.

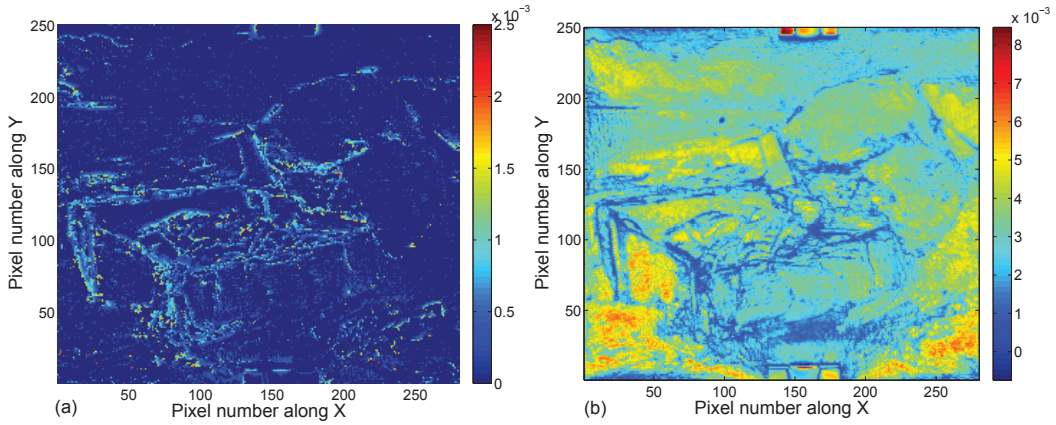

Figure 5.7: THz C-scans based on the Type I signal and the main peak indicating the surface feature of the painting.

For Type II and Type III, shown in Fig. 5.6(b) and (c), one featured peak is detected between the air/paint and paint/paperboard interfaces. This peak indicates the existence of an additional underlying paint layer; therefore, there are in total two paint layers on the paperboard at this pixel. The observation of this peak is important for a successful stratigraphic reconstruction, since it is hidden in the overlapping echoes in the THz B-scans based on the raw data. For peaks with positive sign, shown in Fig. 5.6(b), we conclude that the refractive index of the first paint layer

is smaller than that of the second paint layer. For peaks with negative sign, shown in Fig. 5.6(c), the refractive index of the first paint layer is larger than that of the second paint layer. THz C-scans are plotted based on the amplitude of this featured peak, shown in Fig. 5.8. Figure. 5.8(a) exhibits the regions with underlying layers, of which the refractive index is larger than that of the surface pigments; on the other hand, Fig. 5.8(b) displays the regions with underlying layers, of which the refractive index is smaller than that of the surface pigments.

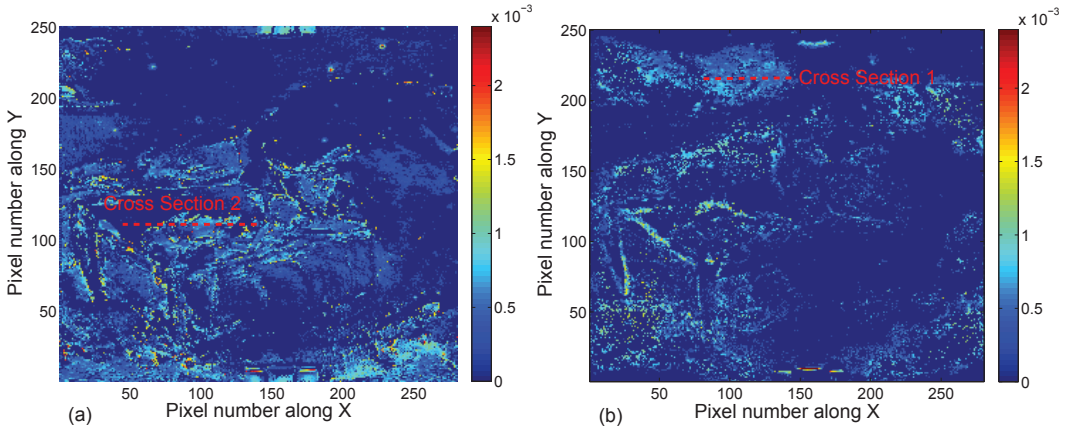

Figure 5.8: THz C-scans based on the Type II and III signals indicating the existence of the underlying layer.

THz B-scans can also be reconstructed based on the deconvolved signals to reveal the stratigraphy of the painting. Based on the peak-detection (both positive and negative peaks), binary THz B-scans (we consider the region with a valid peak as '1' and the other areas as '0') can be obtained. In addition, in order to take into account the fact that the top surface is not flat, but the bottom surface of the paperboard is, the deconvolved signals for binary THz B-scans are further aligned based on the position of echoes reflected from the paperboard/air interface. Binary THz B-scans for the two typical cross sections highlighted in Fig. 5.8 are shown in Fig. 5.9 in comparison with the THz B-scans based on the raw THz data. From the comparison, the paint-layer structure is clearly revealed in the binary THz B-scans from the original overlapping echoes region. Binary THz B-scans for the entire painting can also be

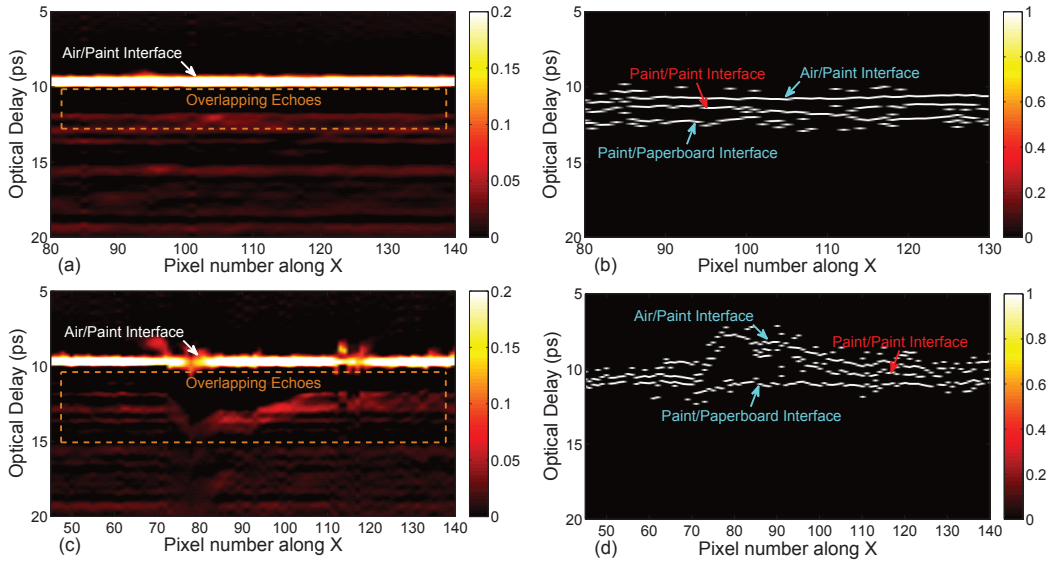

Figure 5.9: Comparison between THz B-scans based on the raw data and binary THz B-scans based on the deconvolved data.

obtained with the deconvolved signals.

For Type IV, shown in Fig. 5.6(d), no extra featured peak can be identified. Therefore, we conclude that there is only one paint layer on the paperboard or the thickness of the underlying layer is too thin to be detected in the THz regime.

5.1.3 Correlation between terahertz and X-ray images

The deconvolved data can also provide quantitative information on the painting, such as the layer thicknesses. The optical thickness of the paint layers can be acquired by calculating the optical delay between the air/paint and paint/paperboard interfaces. The distribution of the paint-layer thickness can reveal in which areas the artist applied more layers of paint. (In our case, the thick paint application with a palette knife resulted in considerable impasto that enables us to check the reasonableness of our THz results visually or tactilely.) If the refractive indice of the pigments of different colors, and of the oil binder, are known, the physical thickness of the paint layers can be calculated. In practice, however, it is difficult to obtain the refractive index of the pigments in an actual art painting nondestructively. In this study, we

assume the refractive index to be constant in different paint layers, which enables us to roughly estimate the physical thickness distribution of the applied paint layers on the basis of the optical thickness in the THz regime.The normalized THz image of the thickness distribution based on the optical thickness of the applied paint layers is shown in Fig. 5.10. A visible raking light image of *After Fishing* is shown in Fig. 5.11 to support our assumption. The raking light image provides information on the surface topography, which also highlights the physical thickness distribution of the applied paint layers on the paperboard. Areas with thicker applied paint layers, as determined in Fig. 5.11, also show high contrast in Fig. 5.10. Relatively small differences in the refractive indices of various paint layers at their mutual interfaces produce the Fresnel coefficients resulting in the echoes we observe. Still, as we argue, we are able to obtain a reasonable estimate of layer thicknesses and overall thickness of the paint application.

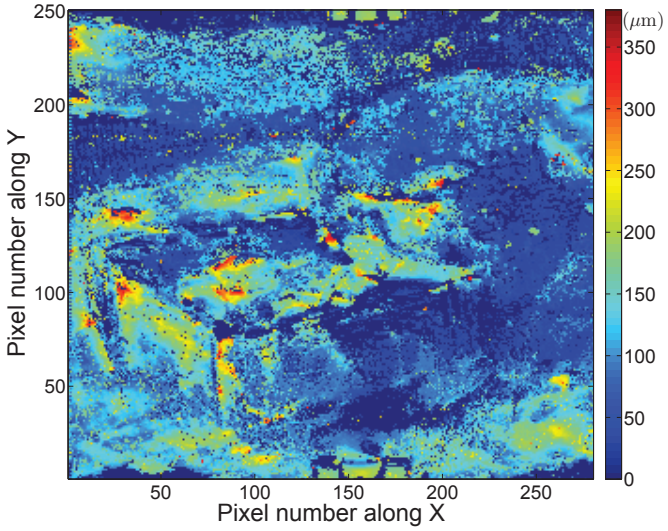

Figure 5.10: THz image of the thickness distribution of the applied paint layers calculated with an estimated refractive index of the pigments.

Finally, we point out the high degree of correlation between the THz image of thickness distribution in Fig. 5.10 and the X-ray transmission image in Fig. 5.1(b). Whereas Fig. 5.10 provides a measure of the optical thickness of the painting and

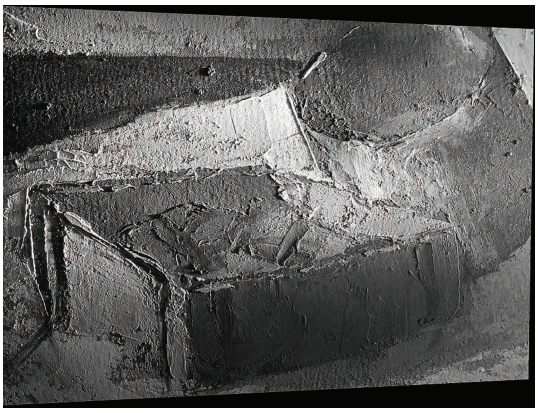

Figure 5.11: Raking light image of *After Fishing*.

an estimate of the amount of paint applied on the paperboard, Fig. 5.1(b) provides a measure of the total X-ray scattering strength in a given pixel, which is also a measure of the amount of material present, but also must account for the atomic number of the constituents, core levels, etc. A fused image of Fig. 5.10 and Fig. 5.1(b) with normalized intensities is created using color to distinguish the similar intensity between the two images, which is shown in Fig. 5.12. By using red for Fig. 5.1(b) and green for Fig. 5.10, areas of similar intensity between the two images are shown yellow in the fused image. In Fig. 5.12, we can observe that the yellow areas are dominant and are mostly located in the regions with relatively thicker layers. Green areas shows the regions where Fig. 5.10 displays a higher response, corresponding to the regions with relatively thinner layers. Red areas, where the X-ray image shows higher response due to its shorter wavelength, highlight the regions containing angles and edges on the surface of painting, which are composed of more paint. On the contrary, regions in red are considered as rough in the THz regime, and due to the diffuse reflection, the received THz signals there belong to the Type I signals, which cannot provide accurate thickness information. Although the X-ray image reveals the features which are lost in the THz image of thickness distribution, it is also noticed that red areas in Fig. 5.12 present high similarity to the previous THz image in Fig. 5.7(a). Therefore, we can conclude that THz imaging can be utilized to obtain

information that is similar to that contained in conventional X-ray imaging.

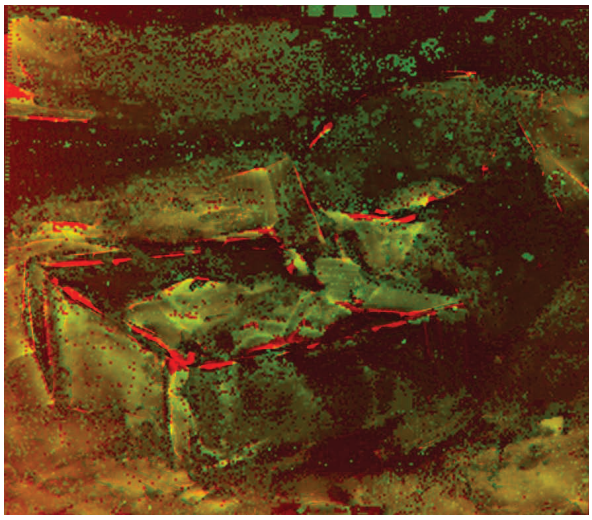

Figure 5.12: The fused image of the X-ray image in red and THz thickness distribution image in green to distinguish the areas of similar intensity in yellow.

In this section, THz frequency-wavelet deconvolution is implemented specifically for the stratigraphic and subsurface investigation of art paintings. A mid-20th Italian oil painting on paperboard, *After Fishing*, by Ausonio Tanda is systematically examined with the method. Utilizing THz reflective imaging, the surface features and a distribution of spots in the paperboard are clearly revealed based on THz raw data. THz frequency-wavelet deconvolution is applied to the THz raw data, and the stratigraphy of the paint layers is successfully reconstructed across the painting based on the deconvolved data. THz C-scans and B-scans are analyzed based on different types of deconvolved signals to investigate the subsurface features of the painting, including the identification of regions with more than one paint layer, the refractive-index difference between paint layers, and the distribution of the paint-layer thickness. Based on our study, we conclude that THz frequency-wavelet deconvolution can be an effective tool for the stratigraphic and subsurface investigation of art paintings, and may also be applied for the characterization of other stratified systems.

In addition, one striking point comes out of this study is the high similarity between the THz and X-ray images. THz imaging of the thickness distribution of

the paint exhibits a high degree of correlation with the X-ray transmission image. Moreover, THz imaging also reveals the spots in the paperboard which cannot be identified in the X-ray image. Compared with X-ray imaging, THz imaging can be carried out in reflection, so that there is no need access to both sides of a painting; THz imaging can provide information in depth and THz data contains spectral information which can potentially be used to identify different pigments. Therefore, our results open up the way for the use of non-ionizing THz imaging as a potential substitute for ionizing X-ray analysis in nondestructive evaluation of art paintings.

5.2 Terahertz characterization of the stratigraphic details of a 17th century Italian oil painting on canvas

One lacuna in the past success of THz stratigraphic characterization of paintings, however, is the field of pre-19th century easel paintings, where the paint layer thicknesses are usually smaller than 50 μm. This characteristic paint-layer thickness is optically thin in the THz regime, since it is much less than the time over which the THz pulse propagates within its duration, corresponding to the depth resolution of a typical THz-TDS system. Nonetheless, there may be spectral information present at the relevant short wavelengths that is obscured in the raw signal. In the context of THz reflectometry, when dealing with optically thin paint layers, the THz echoes resulting from the various interfaces between layers will partially or even totally overlap in time and thus these echoes will merge rather than be distinct. In addition, the depth resolution achieved by FWDD is not high enough to characterize the stratigraphy of typical easel paintings before the 19th century. Consequently, to our knowledge, the detailed stratigraphy of pre-19th century easel paintings has not been clearly revealed by THz reflectometry, as the paint layers in easel paintings are usually very thin in the THz regime, especially for the 16th and 17th century easel paintings.

In this study, in order to tease out the detailed stratigraphic information that is actually contained in the reflected THz signal, the sparse representation is introduced in the deconvolution process. Generally, the reflected THz signals from multilayered structures are a class of very special signals comprised of a limited number of echoes; therefore, the corresponding impulse-response functions have a sparse representation, which means only a limited number of data points have non-zero values. This feature enables us to exploit the sparse constraint and retrieve the impulse-response function by sparsity-based time-domain deconvolution. Here we present THz reflectometry with subwavelength depth resolution for stratigraphic characterization based on a sparsity-based time-domain deconvolution algorithm as developed by our group, which enables us to show the detailed stratigraphy of a 17th century easel painting based on THz reflectometry for the first time to our knowledge. The paint layers on the canvas support of this painting are very thin compared to the dominant wavelength in the available THz spectrum; thus, the THz echoes reflected from the paint layers on the supporting canvas of this painting are strongly overlapped in the first cycle of the reflected THz signal. With the sparsity-based impulse-response function achieved by deconvolution, we gain 3D quantitative insight into the detailed stratigraphy above the canvas throughout the painting, including the varnish, pictorial layer, underpainting, imprimatura, and the ground layer. In addition, we identify delaminations in the pictorial layer associated with age-induced craquelure, and locate a hitherto unidentified extensive restoration of the painting. We emphasize, this is the first time to our knowledge THz reflectometry has resolved multiple layers in an easel painting with such thin layers. Although we focus on easel paintings, the proposed modality can be applied to a wide range of culture heritage objects and provides invaluable information for art-historical studies, as well as for conservation, restoration, and authentication.

The painting in this study was chosen as a typical painting for the period that

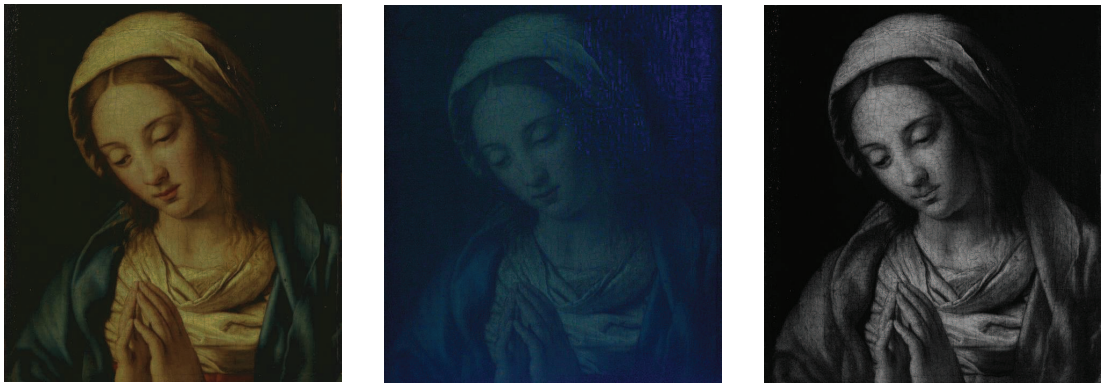

(a) (b) (c)

Figure 5.13: Images of *Vierge en priere*. (a) Visible photograph of the *Viège en priere*; Image of *Viège en priere* obtained by UV Fluorescence; (c) Image of *Viège en priere* obtained by IR Reflectography.

is specifically of the type that has resisted considerable attempts to characterize its stratigraphy, i.e., the relevant layer thicknesses are on the order of tens of microns. It is a 17th century oil painting on canvas, entitled the *Vièrge en priere* (artist unknown) of Italian provenance from the Musée de la Cour d'Or, Metz, France, shown in Fig. 5.13(a). The dimensions of this painting are 24 cm by 32 cm. The canvas is mounted on a wood stretcher. Visually, the paint application itself is smooth and uniform, though subsequently formed craquelure or other inclusions in the canvas give rise to nonuniform features in the surface texture. Multispectral imaging was performed with the Profilocolore HMI (Hypercolorimetric Multispectral Imaging) system, based on a modified Nikon D800FR camera to obtain the spectral reflectance of the surface in the range of 300-1000 nm, with a spatial resolution of 36 Mpixel. The intention is that different types of physical structures and pigments may be revealed by various wavelengths. Images obtained by ultraviolet (UV) Fluorescence and infrared (IR) Reflectography are shown in Fig. 5.13 (b) and (c), respectively. UV Fluorescence can reveal the presence of natural resin varnishes, which often fluoresce under UV light. It is also able to identify any retouchings on top of an aged varnish, since oil paint and newer varnish do not fluoresce under UV. Retouchings therefore appear

as dark patches on the varnish surface. In Fig. 5.13(b), a piece of dark patch near the *Vièrge*'s head can be clearly identified, which may corresponding to a retouching area. Infrared light can pass through the varnish and reveal the features of the surface and subsurface of the pictorial layers. In Fig. 5.13(c), age-induced craquelure in the pictorial layer can be observed.

THz reflective imaging based on a typical THz-TDS system (Teraview TPS Spectra 3000) was performed at almost normal incidence from the top (i.e., painted) surface of the painting. Before scanning the painting, a reflected THz reference signal was recorded by setting a metal plate at the sample position. The THz emitter and detector were raster-scanned by a set of motorized stages moving in the X and Y directions with a 1-mm step size over a 22 cm by 25 cm region of the painting. The painting was mounted paint facing downward supported by the edges of the stretcher in a horizontal configuration. After performing the scan, the positions of the last echo in the reflected signal at each point imaged, corresponding to the bottom surface (interface between the canvas and the air) of the painting, were aligned to the same position temporarily to correct for gravity-induced sag and convenience for further signal processing. After this alignment, a 3D volume raw data set was acquired.

5.2.1 Terahertz raw images of *Vièrge en priere*

First, we present the THz images based on the raw THz signals directly obtained from the scan. THz C-scans (two-dimensional presentation of data displayed as a top planar view of the painting) are shown in Fig. 5.14. The THz C-scan in the time domain is plotted based on imaging contrast mechanism as the peak-to-valley amplitude of the reflected THz signal (mainly the peak-to-valley amplitude of the first cycle), shown in Fig. 5.14(a). The THz C-scan in the frequency domain can also be obtained by taking the Fourier transform of the raw waveform at each pixel, and integrating the magnitude of the frequency components between 0.5 and 1.0 THz, as

shown in Fig. 5.14(b). THz C-scans based on these two contrasts mainly present the THz response of the paint pigments (as we clearly see that the dominant features are those of the visual aspects of the painting), and also reveal the surface roughness, as well as evidence of subsurface features. In Fig. 5.14(a), the Fresnel coefficient between the top-most paint layer and air depends on the refractive indices of the pigment, and so the image of the *Vièrge* is clear. Many of the more irregular features, which will be commented on in depth below, are associated with the surface morphology of the painting. In the presence of a surface irregularity, enhanced scattering of THz radiation occurs, and consequently there is a weaker specular signal. In a similar fashion, Fig. 5.14(a) reveals similar (but not identical) features. In fact, the THz C-scan in the frequency domain is somewhat more effective in revealing surface features, as higher frequency components within the integrated spectral bandwidth, correspond to shorter wavelengths, bringing out small and subtle features.

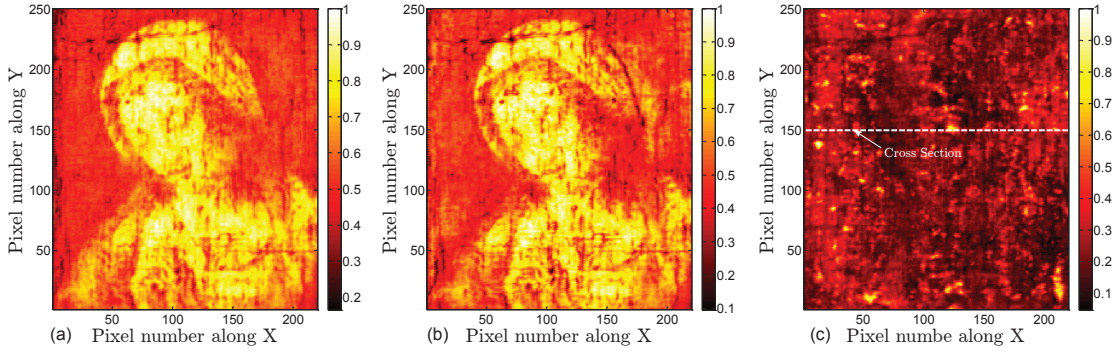

Figure 5.14: THz C-scans based on the raw THz data based on the following contrast mechanisms in the reflected signal: (a) peak-to-valley amplitude; (b) integrated spectrum between 0.5 and 1.0 THz; (c) peak-to-valley amplitude between 13 to 18 ps. The horizontal line at $Y = 150$, marked cross section, is in reference to the B-scan in Fig. 5.15. Contrast is normalized to one.

While a THz C-scan is an X, Y image of the painting, a THz B-scan (two-dimensional presentation displayed as a cross-sectional view of the painting) provides depth information along a line in the X, Y plane. Note that optical delay in the received reflected signal serves as a surrogate for depth. Translating from optical de-

lay to depth also requires a knowledge of the refractive indices of the various layers. The THz B-scan based on the raw data with the cross-section $Y = 150$ is plotted in Fig. 5.15 to show the structure of the painting. Note that in the present case, the contrast mechanism is simply the magnitude of the reflected signal at a given optical delay. The raw THz reflected signals at pixels $(89, 150)$ and $(124, 150)$ are also plotted for reference. These two signals show similar features associated with reflections off corresponding features, although there are slight differences due to local variations across the painting. The roughly horizontal features in the B-scan indicate reflections off interfaces between layers in the painting. The first large feature in optical delay (between 8 and 10 ps optical delay) is due to reflection off the painting surface, below which we see a clear feature ($\sim$13 ps) due to the reflection off the ground-layer/canvas interface. The canvas layer can be clearly identified as corresponding to time delays from 13 to 20 ps. The pronounced horizontal features at $\sim$15.5 and 17 ps are due to the fact that the painting contains a double layer of canvas, as is verified by visual inspection of the edge of the painting. A few pronounced inhomegeneities inside the canvas, which produce additional echoes, are evident in the B-scan and in the C-scan based on the peak-to-valley value in the time slice, in Fig. 5.14(c) above.

Moving above the canvas into the paint layers (optical delay $<$14 ps), however, the THz B-scans based on the raw data do not provide any clear stratigraphic detail, since the stratigraphy of the painting above the canvas is hidden in the first cycle of the reflected THz signal (which is blocked in yellow in Fig. 5.15), and the depth resolution based on the raw THz signals is not high enough to resolve the various paint layers. The available THz spectrum in our system extends to $sim3$ THz; this corresponds to $\sim$100 μm. Accounting for a representative refractive index of 1.6, this limits us to a depth resolution, conventionally defined, of 100 μm$/1.6 \approx 60$ μm. In other words, the absence of useful information from the raw THz is not merely due to the overlapping echoes; the minimum optical thickness that can be resolved is limited

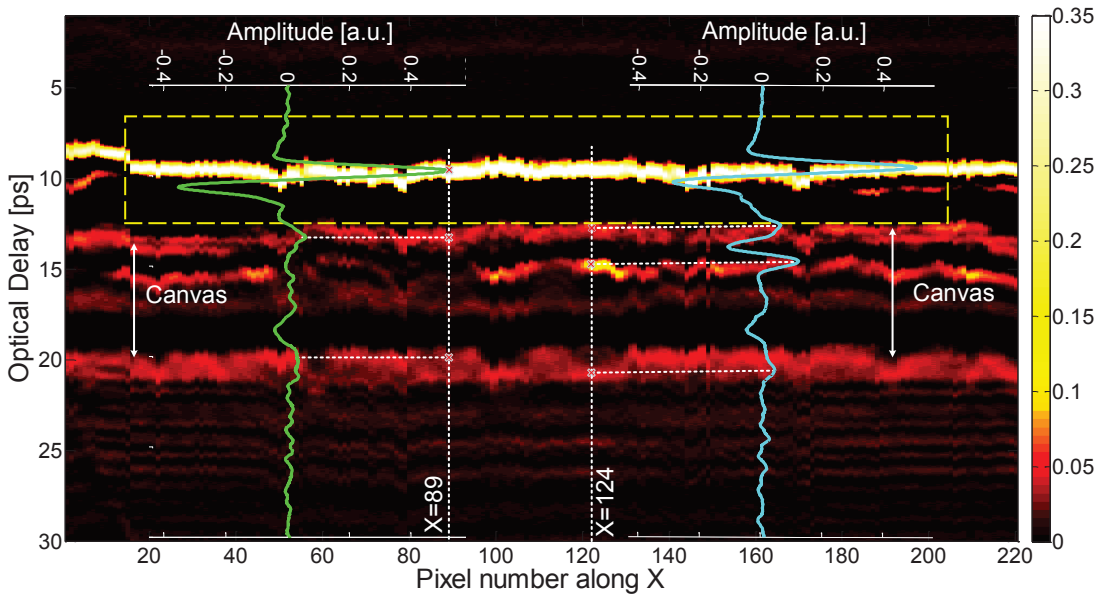

Figure 5.15: The THz B-scan based on the raw signal with the cross-section $Y = 150$. Two typical THz reflected signals are plotted corresponding to the THz B-scan, with the waveform at pixel (89, 150) in green and the waveform at pixel (124, 150) in blue.

to $\sim$100 μm. Nonetheless, as we shall see, due to the nature of the painting's layer structure, we can reconstruct the stratigraphy on a scale significantly below $\sim$100 μm. This is also the reason the time-domain THz C-scan in Fig. 5.14(a) contains both the surface and subsurface features.

As mentioned above, the detailed stratigraphy associated with the painting itself is not evident in the raw data. Nonetheless, the sought for information is indeed contained in the data; it is a matter how to extract it in order to reconstruct the stratigraphy. Sparsity-based time-domain deconvolution based on the shrinkage algorithm is utilized to process the 3D volume raw data. After deconvolution, a sparsity-based impulse-response function is achieved, which entirely depends on the stratigraphy and provides a new imaging parameter with enhanced depth resolution. In the left-hand frames are shown three examples of raw THz signals received at various pixels (black curves) in Fig. 5.16(a1), (a2), and (a3). The corresponding sparsity-based impulse response functions are shown in the right-hand frames, Fig. 5.16(b1), (b2), and (b3).

FWDD (detailed procedure in [83]) is also employed to process the raw data for comparison. It is important to note that, in the deconvolution process, we consider the THz reference signal as the input and the reflected THz signal as the output; therefore, the actual impulse response function associated with reflection coefficients should be obtained by multiplying the deconvolved signal by a factor of –1 for phase correction.

5.2.2 Sparsity-based deconvolved signals

The sparsity-based deconvolution result of the reflected THz signal at pixel $(89, 150)$ is shown in Fig. 5.16(b1). Six peaks are clearly identified in the sparsity-based impulse-response function, which correspond to five separated layers above the canvas. Compared with the result achieved by FWDD, which presents quite broad peaks and fails to reveal the underlying stratigraphy, the sparsity-based deconvolution result shows sharp features associated with interfaces between optically thin layers. Based on a knowledge of the typical structure of easel paintings [91] of this period and visual inspection (see below), these five layers are expected to correspond to the varnish, pictorial layer, underpainting layer, imprimatura, and ground layer. The peaks are positive or negative, depending on whether the refractive index of the following layer is larger or less than that of the preceding layer. Finally, to check that the sparsity-based deconvolved signals indeed correspond to our raw signals, we re-convolve the deconvoluted signals with the THz reference signal obtained by reflecting off a metal plate, and recover reconstructed signals [brown curves, Fig. 5.16(a1), (a2), and (a3)] with high fidelity compared with the received raw signals. This verifies our sparsity-based deconvolution procedure.

The sparsity-based impulse-response function, which consists of a baseline at zero and then a sequence of sharp peaks, enables us to reconstruct the detailed stratigraphy of the painting. Based on the peak-detection (both positive and negative peaks),

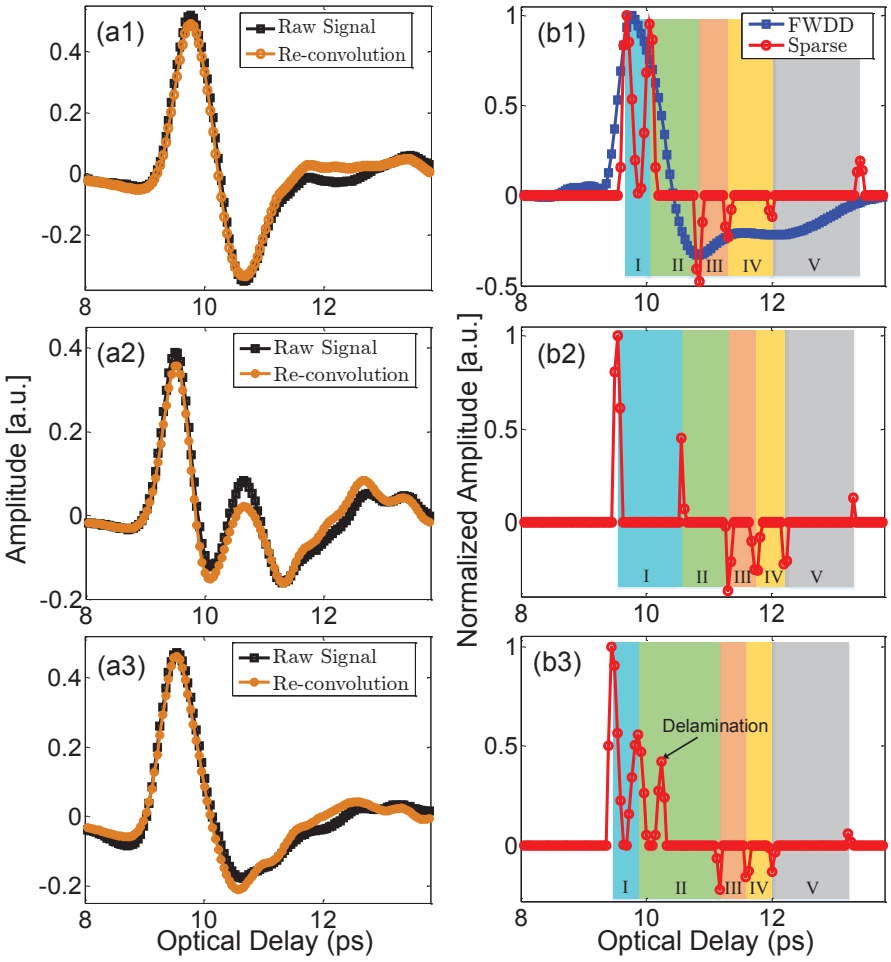

Figure 5.16: Typical THz reflected signals and the sparsity-based deconvolved signals. Figures 5.16(a1), (a2), and (a3) show examples of raw reflected signals (black) and signals reconstructed from the sparse-deconvolution and reference signals. Figures 5.16(b1), (b2), and (b3) show the corresponding sparsity-based deconvolution signals (red); Fig. 5.16(b1) also shows the deconvolved signal achieved by FWDD for comparison.

binary THz B-scans, in which a valid peak is assigned value '1' and the other positions '0' regardless of the sign or height of the peak, can be obtained. The binary THz B-scan with the cross-section $Y = 150$ is shown in Fig. 5.17(b). Compared with the THz B-scan based on the raw signals in Fig. 5.17(a), the binary THz B-scan clearly contains a wealth of information absent in the raw B-scan and reveals the stratigraphy above the supporting canvas. Indeed, this provides the stratigraphic details of the painting and is our main result.

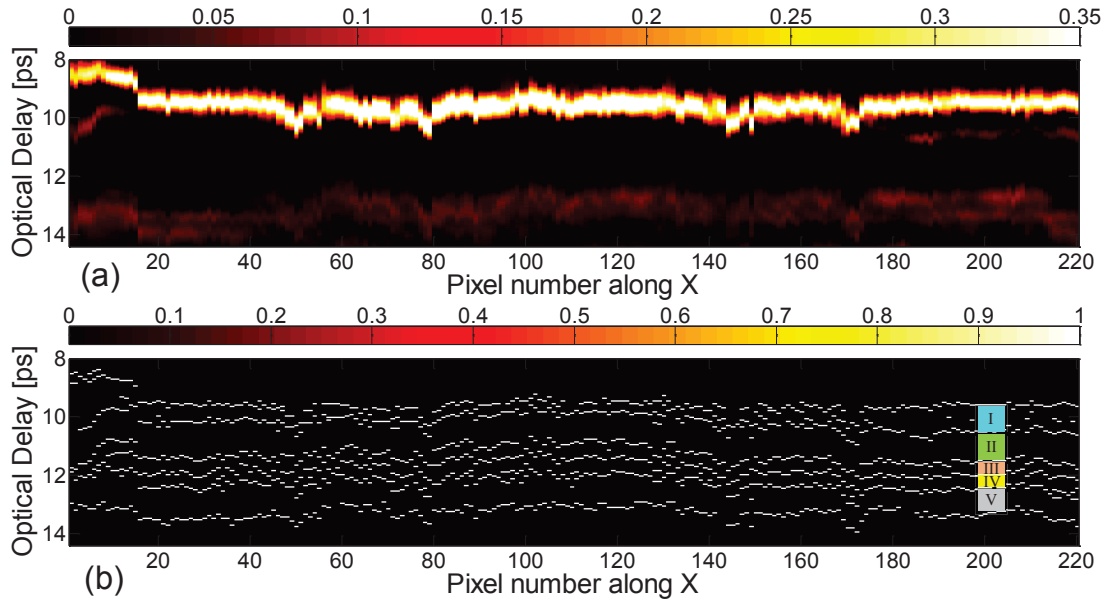

Figure 5.17: Comparison for optical delay corresponding to the layers above the canvas between (a) the THz B-scan based on the raw data (Fig. 5.15 on an expanded vertical scale) and (b) the binary THz B-scan based on the deconvolved data with the cross-section $Y = 150$ in which a valid peak is assigned value '1' and the other positions '0' regardless of the sign or height of the peak.

We synthesize our results to provide a tentative account of the stratigraphy of *Vièrge en priere.* The sparsity-based deconvolved signal, as seen above, contains a wealth of information concerning the various layers present in the painting as seen in the B-scan of Fig. 5.17. In order to reconstruct the layer-structure *across* the painting, it is useful to present the deconvolved data as C-scans that emphasizes individual layers. We can do this by focusing on the amplitude of a specific reflected

peak or the optical delay between specific successive peaks in the signals obtained across the canvas.

5.2.3 3D global mapping of detailed stratigraphy

THz C-scans based on the amplitude of the first reflected peak and C-scans based on the optical delay between the first and the second peaks are shown in Fig. 5.18, which reveal the features of the topmost layer in the painting, *viz*, the varnish. The THz C-scan in Fig. 5.18(a) shows only faint features associated with the painting's composition. Instead, the C-scan is dominated by the surface morphology of the varnish surface, *i.e.*, the surface roughness and variations associated with the craquelure due to aging. The lighter, more yellow areas to the left and right of the *Vièrge*'s head indicate a smoother surface morphology in these regions. The THz C-scan in Fig. 5.18(b), based on optical delay between the first two reflected peaks, provides the quantitative information about the varnish *thickness* across the painting. Surface-morphology-related features are somewhat suppressed as they do not have a major effect on the varnish thickness across the painting. Based on this C-scan, we observe that the varnish around the *Vièrge*'s profile is thicker to the left and right of her head–the same areas indicating a higher-amplitude first reflected peak. Another striking point is that a small region near the right of the *Vièrge*'s head, as well as the left edge of the painting, shows much thicker varnish. Note that these features seen in the two C-scans discussed above are also evident in the raw and sparsity-based deconvolved signals. At representative pixel $(185, 158)$, the optical delay between the first and second peak is larger, shown in Fig. 5.16(b2).

The THz C-scans based on the amplitudes of the second and third peaks, corresponding to the varnish/pictorial and pictorial/underpainting interfaces, are plotted in Fig. 5.19(a) and (b). On the one hand, Fig. 5.19(a) clearly shows the painting's composition, and is due to the pigment-dependent refractive index of the various

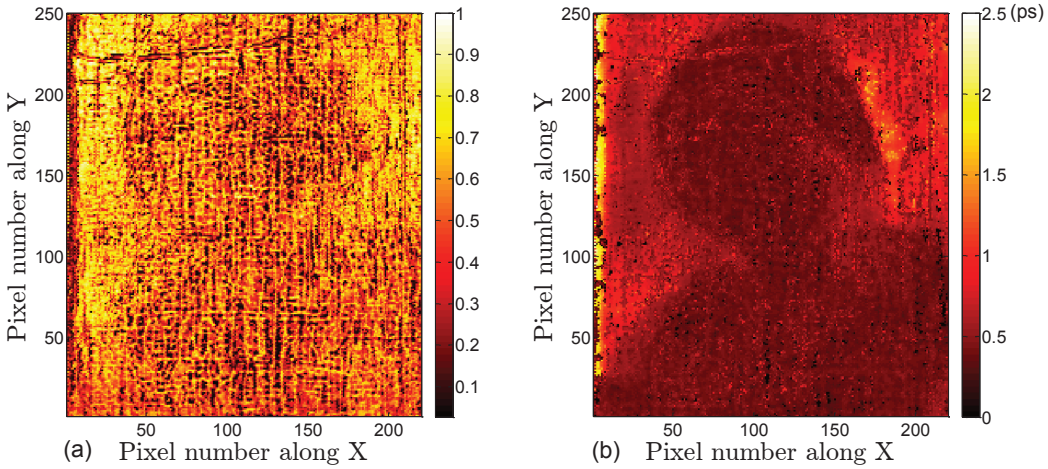

Figure 5.18: Varnish features revealed by THz sparsity-based deconvolved signals. (a) THz C-scan based on the amplitude of the first peak of the deconvolved signal. The contrast is normalized to one; (b) THz C-scan based on the optical delay between the first and second peaks of the deconvolved signal.

colors evident in the final composition. On the other hand, in Fig. 5.19(b) the composition, while visible is less pronounced than in Fig. 5.19(a). This is due to the likelihood that the first-applied pictorial layer may have been fairly uniform in color as was common practice; the most prominent features of the composition, such as drapery, facial features, and hands, were painted subsequently. The various individual paint applications in the pictorial layer thus involve fairly gradual changes in refractive index in layers too thin to resolve in our measurements. Also note that a fine network of horizontal and vertical lines is evident. The optical delay between the second and third peaks in the deconvolved signals provides information about the optical thickness of the pictorial layer; however, the features are not uniform across the painting, shown in Fig. 5.19(d), and the horizontal and vertical lines are more pronounced. These lines are associated with the age-induced craquelure, where an addition peak between the second and the third peaks can be detected in the corresponding sparsity-based deconvolved signal. A typical signal illustrating this at pixel $(112, 229)$ (a typical pixel in the horizontal line) is shown in Fig. 5.16(a3) and (b3). The physical origin of this peak is the existence of an additional layer in these

areas; however, this layer is too thin to be resolved even in the deconvolved signal, which generates only one observable positive peak. We summarize the presence of this additional peak, and thus delaminated regions, in the binary THz C-scan in Fig. 5.19(c). In this image, white regions indicate the presence of the additional peak, black its absence. The white regions are highly correlated with the craquelure; this is not entirely surprising, since stresses associated with craquelure formation and the channels open to the infiltration of moisture and other contaminants may also lead to delamination localized there.

Continuing to consider subsequent peaks in the sparsity-based deconvolved signal, features associated with the underpainting, imprimatura, and ground layers are investigated based on the THz C-scans in Fig. 5.20. Figures 5.20(a1), (a2), and (a3) provide C-scans based on the amplitudes of the fourth, fifth, and sixth peaks, respectively. Lines associated with the craquelure are still evident due to the shadow effects associated with reduced signals reaching subsequent layers depending on THz reflectivity and scattering from layers above. We note that the fourth and fifth peaks cannot be resolved in the deconvolved signals in all the pixels across the painting, corresponding to the black regions in the THz C-scans. Most of the black regions appear in the woman's profile. This might be due to the multiple paint applications in the profile, which makes the underneath layers thinner than the depth resolution achieved. In Figs. 5.20(b1), (b2), and (b3) are shown C-scans computed from the optical delay between the third and fourth, the fourth and fifth, and the fifth and sixth peaks, respectively, if resolved. We note that, for Fig. 5.20(c), the optical delay is calculated based on the peak corresponding to the ground/canvas interface and the preceding peak which can be resolved. Based on the results, we conclude that the Master of the *Vièrge en prier* applied layers of fairly uniform thickness.

Sparsity-based THz reflectometry provides detailed three-dimensional information, enabling us to reconstruct the detailed stratigraphy of the *Vièrge en priere*.

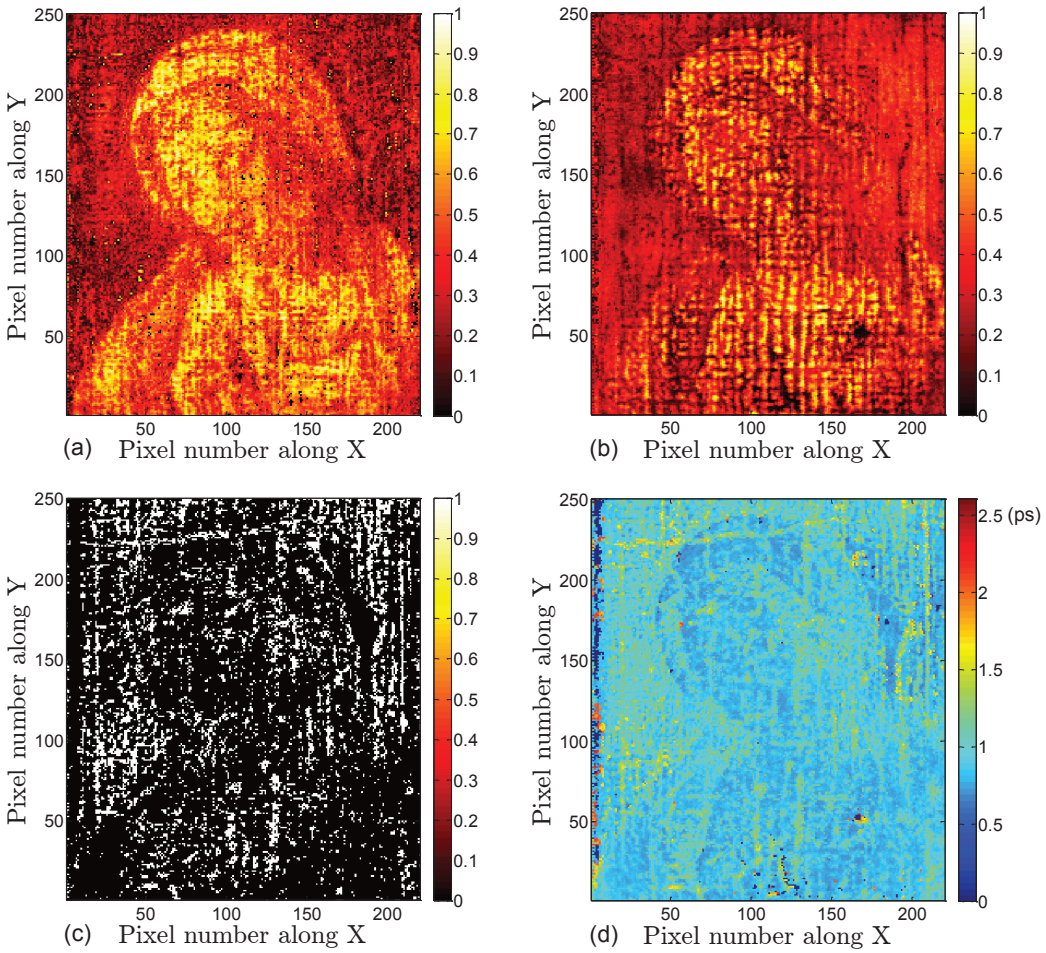

Figure 5.19: Features of the pictorial layer revealed by THz sparsity-based deconvolved signals. (a) THz C-scan based on the amplitude of second peak of the deconvolved signals; (b) THz C-scan based on the amplitude of the peak corresponding to the interface between the pictorial and underpainting layers; (c) binary THz C-scan indicating the positions with the existence of delaminations; (d) THz C-scan based on the optical delay between the peaks corresponding to the thickness of the pictorial layer.

Quantitative information in depth, such as the physical thicknesses of each resolved layer, can be estimated based on the knowledge of corresponding refractive indices. Starting with the canvas, a ground layer (gesso) is applied to seal the canvas and to create a smooth surface on which to paint. The imprimatura, literally the 'first paint layer', follows the ground that would seal the oil-absorbent gesso layer. Without the imprimatura, paint directly applied would soak into the surface and be difficult to control. The underpainting layer provides a proper foundation of the scene/subject matter, which was typically painted in a dark and muted monochrome tone, usually consisting of umber, as brown underpainting has often be used in oil painting right from the 15th to 17th centuries. Such an approach was widespread to the point that the entire tonality and compositions of paintings frequently accounted for this dark underpainting. THz B- and C-scans clearly reveal the features of the ground, imprimatura, and the underpainting layers, which are fairly uniform across the painting. Assuming the refractive index of gesso is about 1.52 [36], the average physical thickness of the ground layer is about 132.7 μm. For other oil-based paint layers, although the difference of refractive index between each layer is sufficient to produce the THz reflections, we assume a mean refractive index of 1.85 [36] in order to estimate the physical thickness of each paint layer. Based on this assumed refractive index, we estimate the average thickness of imprimatura is about 34 μm and the average thickness of the underpainting layer is about 38 μm. The presence of these three preparatory layers is confirmed by optical microscopy near the painting's edge, shown in Fig. 5.21, where these layers are exposed.

The pictorial layers are applied subsequent to the underpainting. They contain the visually evident composition of the finished painting, and consist of additional applications of background color, the figure of the *Vièrge*, facial features, hands, the gossamer veil, and other find details. In the THz C-scans, textural features due to the craquelure first become pronounced in the pictorial layer. This is also where we

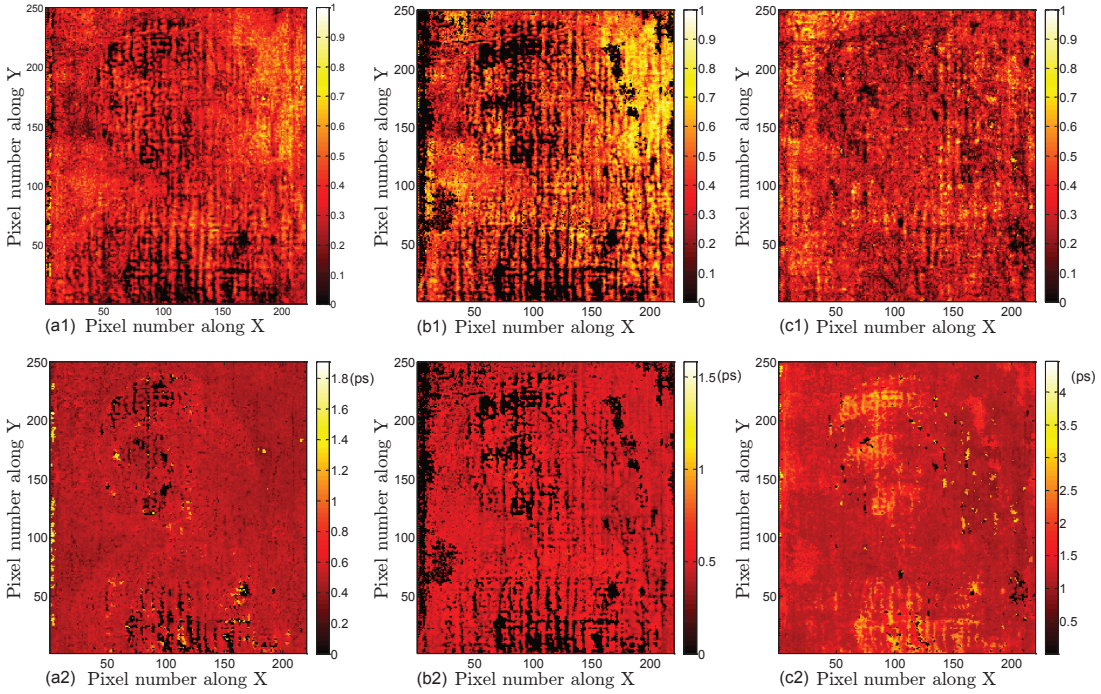

Figure 5.20: Features of the underpainting, imprimatura, and ground layers revealed by THz C-scans based on sparsity-based deconvolved signals. THz C-scans based on the amplitude of (a1) the fourth, (b1) fifth, and (c1) sixth peak. Contrast is normalized to one. THz C-scans based on the optical delay between (a2) the third and fourth peaks, (b2) fourth and fifth peaks, and (c2) fifth and sixth peaks.

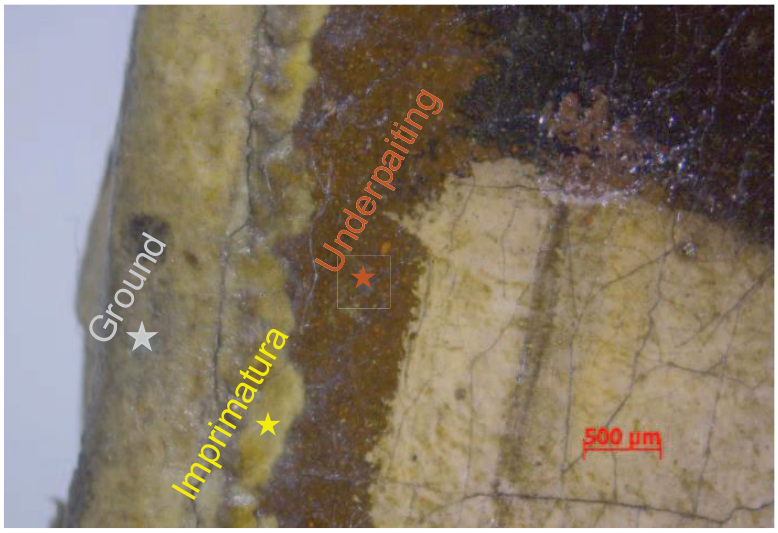

Figure 5.21: The optical microscopic image of a small region at the edge of *Vièrge en priere*. The applications of ground, imprimatura, and the underpainting can be clearly identified.

observe the presence of delamination, closely associated with the craquelure. The surface morphology due to the craquelure can also be seen in white-light raking images shown in Fig. 5.22. In Fig. 5.22(a), the raking light source was placed to the left of the painting, emphasizing inhomogeneities oriented in the vertical direction; in Fig. 5.22(b), the raking light source was placed toward the top side of the painting, emphasizing inhomogeneities oriented in the horizontal direction. Again, strong correlation of the features seen in the raking-light images and in the THz C-scans in Fig. 5.19. Based on the assumed refractive index 1.85, the average physical thickness of the pictorial layer is about 64 μm in the regions without craquelure.

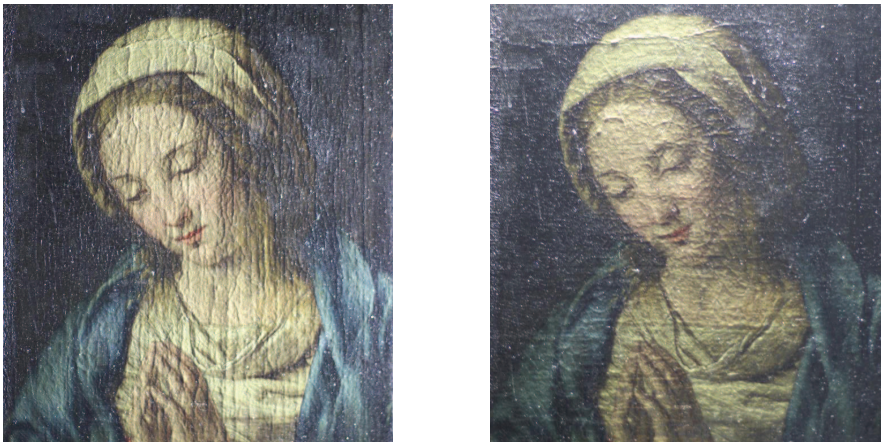

(a) (b)

Figure 5.22: White-light raking images of *Vièrge en priere* with the light source (a) placed on the left side and (b) the top side of the painting.

It was typical in the 17th century finally to apply varnish (a natural resin) to saturate the paint colors and protect the surface. The craquelure continues to be pronounced in the varnish, as is evidenced in the corresponding THz C-scans. The application of the varnish is not uniform across the painting. Assuming the refractive index of the varnish is about 1.6 [67], the physical thickness of the varnish at pixel $(89, 150)$ is about 35 μm. It is important to note that the thicker region near the *Vièrge*'s head is clearly identified, which exhibits the same shape as the dark areas in the UV fluorescence image in Fig. 5.13(c). The physical thickness at pixel $(185, 158)$

is estimated as 96 μm. This thick region is identified as a retouchings of the varnish. Visual inspection shows that these regions exhibit an anomalous texture.

In summary, sparsity-based THz reflectometry proposed in this study clearly revealed the detailed stratigraphy of a 17th century easel painting with layer-thicknesses smaller than 50 μm, including the varnish, pictorial, underpainting, imprimatura, and the ground layers. Retouching of varnish, as well as age-induced craquelure in the pictorial layer are also successfully characterized. The results achieved by sparsity-based THz reflectometry are supported by various techniques. It is important to emphasize that in many cases a single imaging modality provides only very limited information about an art object, and that in practice what can be learned about an artwork by combining several techniques frequently yields more than the sum of what might be learned by applying each technique in a vacuum. Sparsity-based THz reflectometry promises to provide an effective in-situ 3D quantitative imaging modality for a broad range of cultural heritage objects, and an invaluable contribution to art-historical studies, as well as for conservation, restoration, and authentication.

CHAPTER 6
CONCLUSION AND PERSPECTIVE

6.1 Conclusion

The full promise of THz imaging, of which the performance is enhanced by the theories and techniques developed in this thesis, to provide a noninvasive, noncontact, and nonionizing modality for the NDE and material characterization in the field of industry and cultural heritage are well-exhibited.

For the NDE of fiber-reinforced composites, THz imaging shows the capability for providing 3D quantitative characterization of delaminations in glass-fiber reinforced composite laminates. High-resolution, low-artifact THz C- and B-scan images locating and sizing the delaminations are obtained, which enable us to determine the thicknesses of the delamination and the layers constituting the laminate. The influence of atmospheric water-vapor is taken into account when characterizing small delaminations in woven glass-fiber reinforced composites. Wavelet shrinkage de-noising is applied to remove water-vapor features, leading to enhanced THz C- and B-scans to locate the delaminations in three-dimensions with high contrast. In view of the difficulty and expense in purging with dry nitrogen to physically remove the water-vapor features in many cases, the demonstrated results will be of great interest for a range of laboratory- and field-based THz NDE applications. In addition, polarization-resolved THz imaging is firstly applied to a hybrid fiber-reinforced composite laminate. The evolution of intra- and inter-laminar damage throughout the thickness of the laminate subject to low-velocity impact is evaluated. Inter-laminar damage at the interface and the intra-laminar damage close to the same interface can be differentiated by taking advantage of the sensitivity of the carbon-fiber orientation to the THz polarization.

These studies demonstrate that THz imaging can be regarded as an alternative or complementary modality for the NDE of fiber-reinforced composites.

This thesis makes a great contribution to the THz community by developing advanced THz deconvolution techniques to enhance the capability of THz imaging for the stratigraphic characterization of multi-layered structures with optically thin layers in the THz regime. Previously, layers with thicknesses smaller than 100 μm could not be easily resolved and characterized based on the raw THz signals, due to the depth-resolution achieved by a typical THz TDS system, which further limited the applications of THz imaging. Deconvolution, if applied properly, can yield sub-wavelength or sub-pulse-width depth resolution. In the context of THz imaging, three kinds of deconvolution methods are developed in this chapter. Conventional deconvolution, such as THz frequency-wavelet domain deconvolution (FWDD), which is based on inverse filtering is introduced. The depth-resolution achieved by FWDD is about 55 μm in air. A case study for the characterization of various failure modes in polymer-coated with FWDD is also presented. However, depth-resolution achieved by FWDD cannot satisfy the real applications of THz imaging. In order to further enhance the depth-resolution, sparse representation is exploited, and sparse deconvolution based on an iterative shrinkage algorithm has been developed. With an up-sampling approach, sparse deconvolution with super-resolution is also developed to overcome the time resolution limited by the sampling period in the measurement. A simple but effective time-domain model for describing the temporal pulse spreading due the frequency-dependent loss is also designed and introduced into the algorithm, which significantly improves the performance of sparse deconvolution in processing time-varying pulses during the propagation of THz waves in materials. The depth-resolution achieved by sparse deconvolution is about 45 μm in air. Finally, a novel method for enhancing the depth-resolution of THz deconvolution based on autoregressive spectral extrapolation is developed. An autoregressive process is modeled based

on the THz frequency components with high SNR, and the missing frequency components in the low SNR regions are extrapolated based on the autoregressive model. In this way, the entire THz frequency spectrum of the impulse response function is recovered. This method is able to provide a 'quasi-ideal' impulse response function, and therefore, significantly enhances the depth-resolution for resolving optically thin layers in the THz regime. The depth-resolution achieved by this method is about 27 μm in air. The deconvolution techniques developed and presented in this thesis greatly enhance the capability for resolving optically thin layers in the THz regime, and provide a powerful tool to the entire THz community for a broad applications.

Finally, based on the advanced deconvolution techniques developed in this thesis, the capability of THz reflectometry for the characterization of stratigraphy in historical paintings is significantly improved. Compared with other existing techniques, THz reflectometry with enhanced depth-resolution can provide 3D global mapping of the stratigraphy quantitatively. The most promising result in this thesis is that the detailed stratigraphy of a 17th century Italian easel painting, *Vièrge en priere*, is successfully revealed via sparsity-based THz reflectometry. The detailed layer structure, including the canvas, the ground, imprimatura, underpainting, pictorial, and varnish layers are clearly identified. In addition, a hitherto unidentified restoration of the varnish has been found. It is important to note that, it is the first time to our knowledge THz reflectometry has resolved multiple layers in an easel paintings. Based on this work, THz reflectometry shows great potentials in providing in-situ 3D quantitative information for a broad range of art-historical studies, as well as for conservation, restoration, and authentication.

6.2 Perspective

The potential applications of THz imaging in the fields of industry and cultural heritage conservation are being explored continuously.

For the NDE of fiber-reinforced composites, THz imaging of carbon fiber-reinforced composites should be emphasized, since carbon fiber-reinforced composites are most widely used in the aerospace and automotive industries to take the place of metal. Although the conductivity of carbon fibers limits the penetration depth of THz waves, the enhanced THz imaging by deconvolution is expected to perform sub-surface investigations of carbon fiber-reinforced composites. The damage mechanisms induced by tension or bending in woven fiber-reinforced composites will be well-studied via THz imaging. The main damage mechanisms introduced by tension are complex and can be classified into micro-structural damage within the fiber strands and the macroscopic damages within the composites. Considering the wavelength of THz waves, the macroscopic damage mechanisms including transverse cracks in weft, cracks in pure-matrix regions, delamination between warp and weft and between adjacent layers, warp tensile failure and finally fracture, are expected to be revealed by THz imaging. By mapping the material parameters under THz different frequencies, THz images in transmission or reflection are expected to show the cumulative damage patterns across the sample plane. Damage indicators for the existence of various damages and defects due to tension or bending are also expected to develop, which is benefical for identifying and detecting damages at the initial stage of the fatigue life of woven-fabric composites.

For the THz imaging in cultural heritage conservation science, there are still several open challenges to be faced. The knowledge of the THz fingerprints of materials used in artworks is rare. Contributions should be made to the development of a global reliable and standardized database in order to improve the quantitative analysis and material identification. THz studies of archaeological and historical objects will be carrying on. Correlation between THz images and images from other NDE techniques will be made to reveal the various features of artworks.

The deconvolution methods developed in this thesis have already reached the

limitation of the depth-resolution considering the THz wavelength. In order to further increase the depth resolution, producing THz pulses with shorter time-duration or establishing THz interferometry imaging techniques might be necessary. Current deconvolution procedure is based on the THz reference signal and the reflected THz signals. Blind deconvolution in the THz context is still needed in order to get rid of the influence of the reference signal and deconvolve the time-varying echoes during the propagation of THz waves. With deconvolution, the structural information at depth can be extracted; however, it is not possible to extract spectral information at a depth of sufficient fidelity. Therefore, more efforts should be made to resolve the spectral signature of the material at depth. Finally, there is significant need for further development of more powerful signal processing routines to allow for real-time analysis of terahertz time-domain signals.

6.3 Publications

Peer-reviewed publications:

1. **J. Dong**, A. Locquet, M. Melis, A. Adrian, C. Meunier, K. Kazek, P. Brunella, and D. S. Citrin, Global mapping of stratigraphy of an old master using sparsity-based terahertz reflectometry, submitted (2017).

2. **J. Dong**, A. Locquet, and D. S. Citrin, Depth-resolution Enhancement of Terahertz Deconvolution by Autoregressive Spectral Extrapolation, *Optics Letters* 42(9), 1828 (2017).

3. **J. Dong**, X. Wu, A. Locquet, and D. S. Citrin, Terahertz Super-resolution Stratigraphic Characterization of Multi-layered Structures Using Sparse Deconvolution, *IEEE Transactions on Terahertz Science and Technology* 7(3), 260-267 (2017).

4. **J. Dong**, A. Locquet, and D. S. Citrin, Terahertz Quantitative Nondestructive

Evaluation of Failure Modes in Polymer-Coated Steel, *IEEE Journal of Selected Topics in Quantum Electronics* 23(4), 8044207 (2017).

5. **J. Dong**, J. Bianca Jackson, M. Melis, D. Giovannacci, G. C. Walker, A. Locquet, J. W. Bowen, and D. S. Citrin, Terahertz Frequency-Wavelet Domain Deconvolution for Stratigraphic and Subsurface Investigation of Art Painting, *Optics Express* 24(23), 26972 (2016).

6. **J. Dong**, A. Locquet, N. F. Declercq, and D. S. Citrin, Polarization-resolved Terahertz Imaging of Intra- and Inter-laminar Damages in Hybrid Fiber-reinforced Composite Laminate Subject to Low-velocity Impact, *Composites Part B: Engineering* 92, 167-174 (2016).

7. **J. Dong**, A. Locquet, and D. S. Citirn, Enhanced Terahertz Imaging of Small Forced Delamination in Woven Glass Fiber-reinforced Composites with Wavelet De-noising, *Journal of Infrared, Millimeter, and Terahertz Waves* 37(3), 289-301 (2016).

8. **J. Dong**, B. Kim, A. Locquet, P. McKeon, N. F. Declercq, and D. S. Citrin, Nondestructive Evaluation of Forced Delamination in Glass Fiber-reinforced Composites by Terahertz and Ultrasonic Waves, *Composites Part B: Engineering* 79, 667-675 (2015).

Conference Presentations

1. **J. Dong**, A. Locquet, and D. S. Citrin, Terahertz Nondestructive Characterization of Multi-layered Structures Using Sparse Deconvolution Accounting for Pulse Spreading, *7th International Conference on Optical Terahertz Science and Technology*, London, UK, 2017.

2. **J. Dong**, A. Locquet, and D. S. Citrin, Terahertz Reflective Imaging of Damage

Mechanisms in the Coating on Metal Substrate, *41st International Conference on Infrared, Millimeter and Terahertz Waves*, Copenhagen, Denmark, 2016.

3. **J. Dong**, A. Locquet, N. F. Declercq, and D. S. Citrin, Polarization-resolved Terahertz Imaging of Impact Damage in a Hybrid Fiber-reinforced Composite Laminate, *43rd Review of Progress in Quantitative Nondestructive Evaluation*, Atlanta, GA, USA, 2016.

4. **J. Dong**, A. Locquet, and D. S. Citrin, 3D Quantitative Damage Characterization in the Coating of a Metal Substrate with Terahertz Waves, *43rd Review of Progress in Quantitative Nondestructive Evaluation*, Atlanta, GA, USA, 2016.

5. **J. Dong**, A. Locquet, and D. S. Citrin, Polarization-resolved Terahertz Imaging of Hybrid Fiber-reinforced Composite Laminate Subject to Low-velocity Impact, *CLEO: Conference on Lasers and Electro-Optics*, San Jose, California, USA, 2016.

6. **J. Dong**, A. Locquet, N. F. Declercq, and D. S. Citrin, Terahertz Imaging of Damage Evolution in Hybrid Fiber-Reinforced Composite Laminate Subject to Low-Velocity Impact, *7th International Workshop on Terahertz Technology and Applications*, Fraunhofer IPM, Kaiserslautern, Germany, 2016.

7. **J. Dong**, J. Liu, B. Kim, A. Locquet, N. F. Declercq, and D. S. Citrin, Forced Delamination Characterization of Glass Fiber Composites using Terahertz and Ultrasonic Imaging, *International Congress on Ultrasonics*, Metz, France, 2015.

8. **J. Dong**, D. S. Citrin, N. F. Declercq, and A. Locquet, Impact Damage Characterization in Hybrid Fiber Composites Using Terahertz Imaging in the Time and Frequency Domains, *40th International Conference on Infrared, Millimeter and Terahertz Waves*, Hong Kong, China, 2015.

9. **J. Dong**, A. Locquet, N. F. Declercq, and D. S. Citrin, Delamination characterization of fiber-reinforced composites using terahertz imaging, *German THz conference*, Dresden, Germany, 2015.

REFERENCES

[1] F. Rutz, M. Koch, S. Khare, M. Moneke, H. Richter, and U. Ewert, "Terahertz quality control of polymeric products," *International Journal of Infrared and Millimeter Waves*, vol. 27, no. 4, pp. 547–556, 2006.

[2] I. Pupeza, R. Wilk, and M. Koch, "Highly accurate optical material parameter determination with THz time-domain spectroscopy," *Optics Express*, vol. 15, no. 7, pp. 4335–4350, 2007.

[3] G. P. Kniffin and L. M. Zurk, "Model-based material parameter estimation for terahertz reflection spectroscopy," *IEEE Transactions on Terahertz Science and Technology*, vol. 2, no. 2, pp. 231–241, 2012.

[4] S. Maik, W. Steffen, J. Christian, and K. Martin, "Modelling heterogeneous dielectric mixtures in the terahertz regime: a quasi-static effective medium theory," *Journal of Physics D: Applied Physics*, vol. 42, no. 6, p. 65 415, 2009.

[5] K. Naito, Y. Kagawa, S. Utsuno, T. Naganuma, and K. Kurihara, "Dielectric properties of eight-harness-stain fabric glass fiber reinforced polyimide matrix composite in the THz frequency range," *NDT & E International*, vol. 42, no. 5, pp. 441–445, 2009.

[6] C Jördens, M Scheller, S Wietzke, D Romeike, C Jansen, T Zentgraf, K Wiesauer, V Reisecker, and M Koch, "Terahertz spectroscopy to study the orientation of glass fibres in reinforced plastics," *Composites Science and Technology*, vol. 70, no. 3, pp. 472–477, 2010.

[7] F. Ospald, W. Zouaghi, R. Beigang, C. Matheis, J. Jonuscheit, B. Recur, J.-P. Guillet, P. Mounaix, W. Vleugels, P. V. Bosom, L. V. González, I. López, R. M. Edo, Y. Sternberg, and M. Vandewal, "Aeronautics composite material inspection with a terahertz time-domain spectroscopy system," *Optical Engineering*, vol. 53, no. 3, p. 31 208, 2013.

[8] K.-H. Im, D. K. Hsu, C.-P. Chiou, D. J. Barnard, I.-Y. Yang, and J.-W. Park, "Influence of terahertz waves on the penetration in thick FRP composite materials," *AIP Conference Proceedings*, vol. 1581, no. 1, pp. 1568–1575, 2014.

[9] V. I. Bezborodov, V. K. Kiseliov, O. S. Kosiak, Y. M. Kuleshov, P. K. Nesterov, and M. S. Yanovsky, "Quasi-optical sub-terahertz internal reflection reflectometer for non-destructive testing of carbon fiber reinforced plastics," *Telecommunications and Radio Engineering*, vol. 73, no. 1, pp. 83–93, 2014.

[10] N Palka, R Panowicz, F Ospald, and R Beigang, "3D non-destructive imaging of punctures in polyethylene composite armor by THz time domain spectroscopy," *Journal of Infrared, Millimeter, and Terahertz Waves*, vol. 36, no. 8, pp. 770–788, 2015.

[11] C. Stoik, M. Bohn, and J. Blackshire, "Nondestructive evaluation of aircraft composites using reflective terahertz time domain spectroscopy," *NDT & E International*, vol. 43, no. 2, pp. 106–115, 2010.

[12] N. Karpowicz, D. Dawes, M. J. Perry, and X. C. Zhang, "Fire damage on carbon fiber materials characterized by THz waves," *International Journal of High Speed Electronics & Systems*, vol. 17, no. 2, pp. 213–224, 2007.

[13] C. D. Stoik, M. J. Bohn, and J. L. Blackshire, "Nondestructive evaluation of aircraft composites using transmissive terahertz time domain spectroscopy," *Optics Express*, vol. 16, no. 21, pp. 17 039–17 051, 2008.

[14] C Jördens, S Wietzke, M Scheller, and M Koch, "Investigation of the water absorption in polyamide and wood plastic composite by terahertz time-domain spectroscopy," *Polymer Testing*, vol. 29, no. 2, pp. 209–215, 2010.

[15] T. Yasuda, T. Iwata, T. Araki, and T. Yasui, "Improvement of minimum paint film thickness for THz paint meters by multiple-regression analysis," *Applied Optics*, vol. 46, no. 30, pp. 7518–7526, 2007.

[16] K Su, Y. C. Shen, and J. A. Zeitler, "Terahertz sensor for non-contact thickness and quality measurement of automobile paints of varying complexity," *IEEE Transactions on Terahertz Science and Technology*, vol. 4, no. 4, pp. 432–439, 2014.

[17] S. Krimi, J. Klier, J. Jonuscheit, G. Von Freymann, R. Urbansky, and R. Beigang, "Highly accurate thickness measurement of multi-layered automotive paints using terahertz technology," *Applied Physics Letters*, vol. 109, no. 2, 2016.

[18] T. Yasui, T. Yasuda, K.-i. Sawanaka, and T. Araki, "Terahertz paintmeter for noncontact monitoring of thickness and drying progress in paint film," *Applied Optics*, vol. 44, no. 32, pp. 6849–6856, 2005.

[19] T. Fukuchi, N. Fuse, M. Mizuno, and K. Fukunaga, "Surface roughness measurement using terahertz waves," *The 3rd International Conference on Industrial Application Engineering 2015 (ICIAE2015)*, 2015.

[20] A. Jagannathan, A. J. Gatesman, and R. H. Giles, "Characterization of roughness parameters of metallic surfaces using terahertz reflection spectra," *Optics Letters*, vol. 34, no. 13, pp. 1927–1929, 2009.

[21] N. Fuse, T. Fukuchi, T. Takahashi, M. Mizuno, and K. Fukunaga, "Evaluation of applicability of noncontact analysis methods to detect rust regions in coated steel plates," *IEEE Transactions on Terahertz Science and Technology*, vol. 2, no. 2, pp. 242–249, 2012.

[22] N. Hasegawa, T. Nagashima, and K. Hirano, "Thickness measurement of iron-oxide layers on steel plates using terahertz reflectometry," *Infrared, Millimeter and Terahertz Waves (IRMMW-THz), 2011 36th International Conference on*, pp. 1–2, 2011.

[23] A. Moriguchi, T. Tanaka, T. Sakagami, and M. Hangyo, "Nondestructive evaluation of steel plate coated with corrosion protection paint utilizing transmission property of thz wave," *Proc. 13th International Symposium on Nondestructive Characterization of Materials (NDCM-XIII)*, vol. 15538, 2013.

[24] K. Fukunaga and M. Picollo, *Characterisation of works of art*. Springer, 2012, pp. 521–538, ISBN: 3642295630.

[25] M. Panzner, U. Klotzbach, E. Beyer, F. Rutz, C. Jördens, and M. Koch, "Non-destructive investigation of paintings with thz-radiation," *Proceedings of the European Conference on Nondestructive Testing*, p. 181, 2006.

[26] K. Fukunaga and M. Picollo, "Terahertz spectroscopy applied to the analysis of artists' materials," *Applied Physics A*, vol. 100, no. 3, pp. 591–597, 2010.

[27] J. B. Jackson, M Mourou, J. F. Whitaker, I. N. Duling Iii, S. L. Williamson, M Menu, and G. A. Mourou, "Terahertz imaging for non-destructive evaluation of mural paintings," *Optics Communications*, vol. 281, no. 4, pp. 527–532, 2008.

[28] A. J. L. Adam, P. C. M. Planken, S. Meloni, and J. Dik, "Terahertz imaging of hidden paintlayers on canvas," *Optics Express*, vol. 17, no. 5, pp. 3407–3416, 2009.

[29] M. Picollo, K. Fukunaga, and J. Labaune, "Obtaining noninvasive stratigraphic details of panel paintings using terahertz time domain spectroscopy imaging system," *Journal of Cultural Heritage*, vol. 16, no. 1, pp. 73–80, 2015.

[30] C. L. Koch Dandolo, A. Cosentino, and P. U. Jepsen, "Inspection of panel paintings beneath gilded finishes using terahertz time-domain imaging," *Studies in Conservation*, vol. 60, no. sup1, S159–S166, 2015.

[31] C. Koch Dandolo, T. Filtenborg, J. Skou-Hansen, and P. Jepsen, "Analysis of a seventeenth-century panel painting by reflection terahertz time-domain imaging (THz-TDI): contribution of ultrafast optics to museum collections inspection," *Applied Physics A*, vol. 121, no. 3, pp. 981–986, 2015.

[32] C. L. Koch Dandolo, M. Picollo, C. Cucci, and P. U. Jepsen, "Fra Angelico's painting technique revealed by terahertz time-domain imaging (THz-TDI)," *Applied Physics A*, vol. 122, no. 10, p. 898, 2016.

[33] C Seco-Martorell, V López-Domínguez, G Arauz-Garofalo, A Redo-Sanchez, J Palacios, and J Tejada, "Goya's artwork imaging with Terahertz waves," *Optics Express*, vol. 21, no. 15, pp. 17 800–17 805, 2013.

[34] C. L. Koch-Dandolo, T. Filtenborg, K. Fukunaga, J. Skou-Hansen, and P. U. Jepsen, "Reflection terahertz time-domain imaging for analysis of an 18th century neoclassical easel painting," *Applied Optics*, vol. 54, no. 16, pp. 5123–5129, 2015.

[35] K. Fukunaga, T. Ikari, and K. Iwai, "THz pulsed time-domain imaging of an oil canvas painting: a case study of a painting by Pablo Picasso," *Applied Physics A*, vol. 122, no. 2, pp. 1–5, 2016.

[36] A. M. Gomez-Sepulveda, A. I. Hernandez-Serrano, R Radpour, C. L. Koch-Dandolo, S. C. Rojas-Landeros, L. F. Ascencio-Rojas, A. Zarate, G. Hernandez, R. C. Gonzalez-Tirado, M Insaurralde-Caballero, and E Castro-Camus, "History of Mexican Easel Paintings from an Altarpiece Revealed by Non-invasive Terahertz Time-Domain Imaging," *Journal of Infrared, Millimeter, and Terahertz Waves*, vol. 38, no. 4, pp. 403–412, 2017.

[37] K Fukunaga, I Hosako, Y Kohdzuma, T Koezuka, M.-J. Kim, T Ikari, and X Du, "Terahertz analysis of an east asian historical mural painting," *Journal of the European Optical Society-Rapid publications*, vol. 5, 2010.

[38] G. C. Walker, J. W. Bowen, W. Matthews, S. Roychowdhury, J. Labaune, G. Mourou, M. Menu, I. Hodder, and J. B. Jackson, "Sub-surface terahertz imaging through uneven surfaces: visualizing Neolithic wall paintings in Çatalhöyük," *Optics Express*, vol. 21, no. 7, pp. 8126–8134, 2013.

[39] C. L. K. Dandolo and P. U. Jepsen, "Wall painting investigation by means of non-invasive terahertz time-domain imaging (THz-TDI): Inspection of subsurface structures buried in historical plasters," *Journal of Infrared, Millimeter, and Terahertz Waves*, vol. 37, no. 2, pp. 198–208, 2015.

[40] K Krügener, M Schwerdtfeger, S. F. Busch, A Soltani, E Castro-Camus, M Koch, and W Viöl, "Terahertz meets sculptural and architectural art: Evaluation and conservation of stone objects with T-ray technology," *Scientific Reports*, vol. 5, p. 14 842, 2015.

[41] M Koch, S Hunsche, P Schumacher, M. C. Nuss, J Feldmann, and J Fromm, "THz-imaging: a new method for density mapping of wood," *Wood Science and Technology*, vol. 32, no. 6, pp. 421–427, 1998.

[42] J. B. Jackson, M Mourou, J Labaune, J. F. Whitaker, I. I. I. I. N. Duling, S. L. Williamson, C Lavier, M Menu, and G. A. Mourou, "Terahertz pulse imaging for tree-ring analysis: a preliminary study for dendrochronology applications," *Measurement Science and Technology*, vol. 20, no. 7, p. 75 502, 2009.

[43] J. Labaune, J. B. Jackson, K. Fukunaga, J. White, L. D'Alessandro, A. Whyte, M. Menu, and G. Mourou, "Investigation of Terra Cotta artefacts with terahertz," *Applied Physics A*, vol. 105, no. 1, pp. 5–9, 2011.

[44] J Labaune, J. B. Jackson, S Pagès-Camagna, I. N. Duling, M Menu, and G. A. Mourou, "Papyrus imaging with terahertz time domain spectroscopy," *Applied Physics A: Materials Science & Processing*, vol. 100, no. 3, pp. 607–612, 2010.

[45] L. Öhrström, B. M. Fischer, A. Bitzer, J. Wallauer, M. Walther, and F. Rühli, "Terahertz imaging modalities of ancient Egyptian mummified objects and of a naturally mummified rat," *The Anatomical Record*, vol. 298, no. 6, pp. 1135–1143, 2015.

[46] J. B. Jackson, J. Labaune, R. Bailleul-Lesuer, L. D'Alessandro, A. Whyte, J. W. Bowen, M. Menu, and G. Mourou, "Terahertz pulse imaging in archaeology," *Frontiers of Optoelectronics*, vol. 8, no. 1, pp. 81–92, 2014.

[47] M Schwerdtfeger, E Castro-Camus, K Krügener, W Viöl, and M Koch, "Beating the wavelength limit: three-dimensional imaging of buried subwavelength fractures in sculpture and construction materials by terahertz time-domain reflection spectroscopy," *Applied Optics*, vol. 52, no. 3, pp. 375–380, 2013.

[48] D. Mittleman, *Sensing with terahertz radiation / Daniel Mittleman, (ed.)* Berlin ; New York : Springer, c2003., 2003, ISBN: 3540431101.

[49] W. Withayachumnankul, B. M. Fischer, and D. Abbott, "Numerical removal of water vapour effects from terahertz time-domain spectroscopy measurements," *Proceedings of the Royal Society A: Mathematical, Physical and Engineering Science*, vol. 464, no. 2097, pp. 2435–2456, 2008.

[50] Y. Wang, Z. Zhao, Z. Chen, K. Kang, B. Feng, and Y. Zhang, "Terahertz absorbance spectrum fitting method for quantitative detection of concealed contraband," *Journal of Applied Physics*, vol. 102, no. 11, p. 113 108, 2007.

[51] C. Ryu and S. G. Kong, "Atmospheric degradation correction of terahertz beams using multiscale signal restoration," *Applied Optics*, vol. 49, no. 5, pp. 927–935, 2010.

[52] Y. Chen, Y. Sun, and E. Pickwell-Macpherson, "Improving extraction of impulse response functions using stationary wavelet shrinkage in terahertz reflection imaging," *Fluctuation and Noise Letters*, vol. 9, no. 04, pp. 387–394, 2010.

[53] D. M. Mittleman, R. H. Jacobsen, R Neelamani, R. G. Baraniuk, and M. C. Nuss, "Gas sensing using terahertz time-domain spectroscopy," *Applied Physics B*, vol. 67, no. 3, pp. 379–390, 1998.

[54] Y. Chen, S. Huang, and E. Pickwell-MacPherson, "Frequency-wavelet domain deconvolution for terahertz reflection imaging and spectroscopy," *Optics Express*, vol. 18, no. 2, pp. 1177–1190, 2010.

[55] B. Ferguson and D. Abbott, "De-noising techniques for terahertz responses of biological samples," *Microelectronics Journal*, vol. 32, no. 12, pp. 943–953, 2001.

[56] R. A. Smith, L. D. Jones, S. J. Willsher, and A. B. Marriott, "Diffraction and shadowing errors in -6 dB defect sizing of delaminations in composites," *Insight-Non-Destructive Testing and Condition Monitoring*, vol. 40, no. 1, pp. 44–49, 1998.

[57] N Athanasopoulos and V Kostopoulos, "Prediction and experimental validation of the electrical conductivity of dry carbon fiber unidirectional layers," *Composites Part B: Engineering*, vol. 42, no. 6, pp. 1578–1587, 2011.

[58] I. Kwang-Hee, D. K. Hsu, C. Chien-Ping, D. J. Barnard, J. Jong-An, and Y. In-Young, "Terahertz wave approach and application on FRP composites," *Advances in Materials Science & Engineering*, pp. 1–10, 2013.

[59] S.-H. Yang, K.-B. Kim, H. G. Oh, and J.-S. Kang, "Non-contact detection of impact damage in CFRP composites using millimeter-wave reflection and considering carbon fiber direction," *NDT & E International*, vol. 57, no. 0, pp. 45–51, 2013.

[60] C. Dong and I. J. Davies, "Flexural strength of bidirectional hybrid epoxy composites reinforced by E glass and T700S carbon fibres," *Composites Part B: Engineering*, vol. 72, no. 0, pp. 65–71, 2015.

[61] N. Palka, S. Krimi, F. Ospald, D. Miedzinska, R. Gieleta, M. Malek, and R. Beigang, "Precise determination of thicknesses of multilayer polyethylene composite materials by terahertz time-domain spectroscopy," *Journal of Infrared, Millimeter, and Terahertz Waves*, vol. 36, no. 6, pp. 578–596, 2015.

[62] W. Tan, B. G. Falzon, L. N. S. Chiu, and M. Price, "Predicting low velocity impact damage and Compression-After-Impact (CAI) behaviour of composite laminates," *Composites Part A: Applied Science and Manufacturing*, vol. 71, no. 0, pp. 212–226, 2015.

[63] J. Zhang and X. Zhang, "Simulating low-velocity impact induced delamination in composites by a quasi-static load model with surface-based cohesive contact," *Composite Structures*, vol. 125, no. 0, pp. 51–57, 2015.

[64] J. R. Fletcher, G. P. Swift, D. Dai, J. M. Chamberlain, and P. C. Upadhya, "Pulsed terahertz signal reconstruction," *Journal of Applied Physics*, vol. 102, no. 11, p. 113 105, 2007.

[65] R. K. H. Galvão, S. Hadjiloucas, A. Zafiropoulos, G. C. Walker, J. W. Bowen, and R. Dudley, "Optimization of apodization functions in terahertz transient spectrometry," *Optics Letters*, vol. 32, no. 20, pp. 3008–3010, 2007.

[66] J. Dong, A. Locquet, and D. S. Citrin, "Enhanced Terahertz Imaging of Small Forced Delamination in Woven Glass Fibre-reinforced Composites with Wavelet De-noising," *Journal of Infrared, Millimeter, and Terahertz Waves*, vol. 37, no. 3, pp. 289–301, 2015.

[67] J. Yun-Sik, K. Geun-Ju, and J. Seok-Gy, "Terahertz Dielectric Properties of Polymers," *Journal of Korean Physical Society*, vol. 49, no. 2, S. 513, 2006.

[68] J. Dong, A. Locquet, N. F. Declercq, and D. S. Citrin, "Polarization-resolved terahertz imaging of intra- and inter-laminar damages in hybrid fiber-reinforced composite laminate subject to low-velocity impact," *Composites Part B: Engineering*, vol. 92, pp. 167–174, 2016.

[69] N Fuse, T Fukuchi, T Takahashi, M Mizuno, and K Fukunaga, "Evaluation of applicability of noncontact analysis methods to detect rust regions in coated steel plates," *IEEE Transactions on Terahertz Science and Technology*, vol. 2, no. 2, pp. 242–249, 2012.

[70] E. P. J. Parrott, S. M. Y. Sy, T. Blu, V. P. Wallace, and E. Pickwell-MacPherson, "Terahertz pulsed imaging in vivo: measurements and processing methods," *Journal of Biomedical Optics*, vol. 16, no. 10, pp. 106 010–106 018, 2011.

[71] I. Daubechies, M. Defrise, and C. De Mol, "An iterative thresholding algorithm for linear inverse problems with a sparsity constraint," *Communications on Pure and Applied Mathematics*, vol. 57, no. 11, pp. 1413–1457, 2004. eprint: 0307152 (math).

[72] E. Carcreff, S. Bourguignon, J. Idier, and L. Simon, "High-resolution deconvolution applied to non destructive testing," *Proceedings of the Acoustics 2012 Nantes Conference*, pp. 2975–2980, 2012.

[73] A. Redo-Sanchez, B. Heshmat, A. Aghasi, S. Naqvi, M. Zhang, J. Romberg, and R. Raskar, "Terahertz time-gated spectral imaging for content extraction through layered structures," *Nature Communications*, vol. 7, p. 12 665, 2016.

[74] S. Zhou, D. G. Valchev, A. Dinovitser, J. M. Chappell, A. Iqbal, B. W.-H. Ng, T. W. Kee, and D. Abbott, "Terahertz Signal Classification Based on Geometric Algebra," *IEEE Transactions on Terahertz Science and Technology*, vol. 6, no. 6, pp. 793–802, 2016.

[75] T. Olofsson and T. Stepinski, "Minimum entropy deconvolution of pulse-echo signals acquired from attenuative layered media," *Journal of the Acoustical Society of America*, vol. 109, no. 6, pp. 2831–2839, 2001.

[76] E. J. Candès and C. Fernandez-Granda, "Super-resolution from noisy data," *Journal of Fourier Analysis and Applications*, vol. 19, no. 6, pp. 1229–1254, 2013.

[77] Y. Chen, Y. Sun, and E. Pickwell-MacPherson, "Total variation deconvolution for terahertz pulsed imaging," *Inverse Problems in Science & Engineering*, vol. 19, no. 2, pp. 223–232, 2011.

[78] T. J. Ulrych and R. W. Clayton, "Time series modelling and maximum entropy," *Physics of the Earth and Planetary Interiors*, vol. 12, no. 2-3, pp. 188–200, 1976.

[79] T. J. Ulrych and T. N. Bishop, "Maximum entropy spectral analysis and autoregressive decomposition," *Reviews of Geophysics*, vol. 13, no. 1, pp. 183–200, 1975.

[80] H. Akaike, "A new look at the statistical model identification," *IEEE transactions on automatic control*, vol. 19, no. 6, pp. 716–723, 1974.

[81] B Shakibi, F Honarvar, M. D. C. Moles, J Caldwell, and A. N. Sinclair, "Resolution enhancement of ultrasonic defect signals for crack sizing," *NDT & E International*, vol. 52, pp. 37–50, 2012.

[82] M. Ortigueira and J. Tribolet, "Global versus local minimization in least-squares ar spectral estimation," *Signal Processing*, vol. 7, no. 3, pp. 267–281, 1984.

[83] J. Dong, A. Locquet, and D. S. Citrin, "Terahertz Quantitative Nondestructive Evaluation of Failure Modes in Polymer-Coated Steel," *IEEE Journal of Selected Topics in Quantum Electronics*, vol. 23, no. 4, pp. 1–7, 2017.

[84] P. Reischig, L. Helfen, A. Wallert, T. Baumbach, and J. Dik, "High-resolution non-invasive 3D imaging of paint microstructure by synchrotron-based X-ray laminography," *Applied Physics A*, vol. 111, no. 4, pp. 983–995, 2013.

[85] I. Reiche, K. Müller, M. Eveno, E. Itié, and M. Menu, "Depth profiling reveals multiple paint layers of Louvre Renaissance paintings using non-invasive compact confocal micro-X-ray fluorescence," *Journal of Analytical Atomic Spectrometry*, vol. 27, no. 10, p. 1715, 2012.

[86] T. E. Villafana, W. P. Brown, J. K. Delaney, M. Palmer, W. S. Warren, and M. C. Fischer, "Femtosecond pump-probe microscopy generates virtual cross-sections in historic artwork," *Proceedings of the National Academy of Sciences*, vol. 111, no. 5, pp. 1708–1713, 2014.

[87] F. Presciutti, J. Perlo, F. Casanova, S. Glöggler, C. Miliani, B. Blümich, B. G. Brunetti, and A. Sgamellotti, "Noninvasive nuclear magnetic resonance profiling of painting layers," *Applied Physics Letters*, vol. 93, no. 3, p. 033 505, 2008.

[88] C. S. Cheung, M Spring, and H Liang, "Ultra-high resolution Fourier domain optical coherence tomography for old master paintings," *Optics Express*, vol. 23, no. 8, p. 10 145, 2015.

[89] M. Alfeld and J. A. C. Broekaert, "Mobile depth profiling and sub-surface imaging techniques for historical paintings—A review," *Spectrochimica Acta Part B: Atomic Spectroscopy*, vol. 88, pp. 211–230, 2013.

[90] M. Bessou, H. Duday, J.-P. Caumes, S. Salort, B. Chassagne, A. Dautant, A. Ziéglé, and E. Abraham, "Advantage of terahertz radiation versus X-ray to detect hidden organic materials in sealed vessels," *Optics Communications*, vol. 285, no. 21–22, pp. 4175–4179, 2012.

[91] A. Nevin, P. Pouli, S. Georgiou, and C. Fotakis, "Laser conservation of art," *Nature Materials*, vol. 6, no. 5, pp. 320–322, 2007.